MICROFABRICATION OF MEMS AND AFM PLATFORMS FOR LUBRICATION STUDY

TANG XIAOSONG

(B Eng) , Xian Jiaotong University

(M.Eng.), Cornell University

A THESIS SUBMITTED

FOR THE DEGREE OF DOCTOR OF PHILOSOPHY

DEPARTMENT OF MECHANICAL ENGINEERING

NATIONAL UNIVERSITY OF SINGAPORE

2013

To my parents, my lovely wife and kids for their love, support and encouragement

DECLARATION

This thesis is an account of my original work undertaken at the National University of Singapore in the Department of Mechanical Engineering and Institute of Materials Research and Engineering under the A-star funded Scientific Staff Development Scheme (SSDS).

The contributors from other researchers toward my work are as following.

i) In Chapter 3, Dr. Loke Yee Chong assisted in the sled microfabrication.

ii) In Chapter 5, Dr. Sean O'Shea built the vacuum AFM.

iii) In Chapter 6, Dr. Lu Pin performed the FEM simulations.

A number of publications have been accepted or submitted that report the work of this thesis. These are listed on page IV of the thesis. This thesis has also not been submitted for any degree in any university previously. I have duly acknowledged all the sources of information which have been used in the thesis.

_____

Tang Xiaosong

22 Jan 2013

ACKNOWLEDGEMENTS

It would not have been possible to write this doctoral thesis without the help and support of the kind people around me, to only some of whom it is possible to give particular mention here.

This thesis would not have been possible without the help, support and patience of my principle supervisors, Prof. Zhou Guangya and Prof. Sujeet Sinha, not to mention their advice and unsurpassed knowledge and friendship.

The good advice, support and friendship of my second supervisor, Dr. Sean O'Shea at Institute of materials Research and Engineering (IMRE) have been invaluable on both an academic and a personal level, for which I am extremely grateful. My sincere gratitude is reserved for Sean for his invaluable insights, hands-on experiment skill and brilliant suggestions. I really appreciate his willingness to meet me at short notice every time and go through several drafts of my thesis. He is an inspiration.

I would like to acknowledge the financial, academic and technical support of the IMRE, and for academic support I must name my research group members first, Lu Pin, Loke Yee Chong, Cui Song, and Sunil. It is such a wonderful team. Thanks for your valuable inputs in the project discussion, simulation and working in fabrication together. Your involvements and suggestions greatly shorten the awkward when I face the problems. I also must mention my previous peers Nitya, Leonard and Lena. Your help notes are very precious.

 I would like thanks Dr. Cedric who lend me the Lock in amplifier and help me to correct

and it give me the hope that anything can be possible. Also, Doreen guided me on viewing the sharp tips in SEM without a metal layer coating and the results are important for explaining the experimental results. Debbie worked on the FIB to process my delicate samples and it is the results long time dreamed. When I have problem to push my small device, I remember Hui Kim lend me her special probe to minimize the charge, and it indeed work. My samples are a bit different from the normal samples in characterizations. Many thanks for your patience and time to explore the handling and specific characterization issue. I would like to specially thank IMRE cleanroom manager, Siew Tat Mun and facility manager Ngiam Ming Cai, for their friendship, not only for all their useful suggestions but also for being there to listen when I needed an ear.

I would also like to take this opportunity to thank Ivan Vakarelski. We have enjoyed a nice time together to fabricate and to characterize the nice patterns of the microwares. I would also like to thank Professor Derek Chan and Professor Raymond Dagastine at Melbourne University for their sincere helpful on the hydrodynamic force and droplet-droplet experiments. The trip to Melbourne is really eye-opening and I gained a lot of AFM related technology.

I would like to thank my colleagues assist me in the test as well, particularly Dr. Yao Kui and his team member Gan Bee Keen, Goh Pei Chin, Christina Tan, LAI Szu Chen, Ji Wei and lim Yee Fun. I am very lucky to be in a good testing environment with many testing apparatus can be readily for my experiments. I also thank Dr. Santi who is very kind to borrow the vacuum pump, magnetic gauge and permanent magnet to me. It save me a lot of trouble to setup a vacuum system integrated with the laser vibrometer. I would like to thank my friends who spend valuable time to help me on proof reading my thesis as well, particular Donna Zhou and Tan Wui Siew.

Amongst my fellow postgraduate students in the Department of Mechanical engineering, I would like to thank Jason Chew and Tian Feng for their kindness, friendship and support, together. We have developed the process and share joy when the first release device was out and survived. I would like to specially thank Dr Sascha at SSLS. He gave me a great help on using the SU8 related processes and he also informed me the valuable process detail in metal plating. Without his help, I might be challenged by a lot of unexpected problem and develop a quick and workable process. I would like to thank for Ren Ya Ping as well, since we have been encouraging each other on the way to pursue the PhD program. I would also like to thank my colleagues and friends met the old College, Madan, Huang Hui, and Li Biao. By no means least, I thank my friends in China, America and elsewhere for their support and encouragement throughout, some of whom have already been named.

Words cannot express the feelings that I have for my parents and my parents-in-laws for their constant unconditional support. I would not be here if it is not for you. Finally, I would like to acknowledge the most important person in my life – my wife Kang Lei. She has been a constant source of strength and inspiration. There were times during the past seven years when everything seemed hopeless and I didn't have any confidence. I can honestly say that it was only her determination and constant encouragement (and sometimes a kick on my backside when I needed one) that ultimately made it possible for me to see this project through to the end.

For any errors or inadequacies that may remain in this work, of course, the responsibility is entirely on my own.

SUMMARY

Microfabrication and the use of micro-electromechanical (MEMS) structures to address friction problems is the theme of this thesis. To this end, MEMS structures called "sleds" are introduced.

Sleds are microfabricated silicon plates with lateral dimensions of 100-300 µm and a plate thickness of only ~300nm or ~3µm. Three sharp tips protrude from the plate and these form a 3-point contact when the sled is placed on a surface. The objective is to make sleds move in-plane across a surface with user-controlled friction based on the idea of actuated superlubricity (A. Socoliuc, *et. al*. Science **313**, 207-210 (2006)). That is, to induce mechanical vibration of the tips in the vertical direction such that sliding occurs in the horizontal.

No motion of the sled was observed using magnetic actuation of sleds with large magnetic particles attached. Ultrasonic actuation was successful and results showing actuation of the sled motion are shown, with the movement controlled by changing the actuation frequency. Sled rotation is often observed and occasionally translation over very large distances (mm). However, we do not believe the motion represents superlubricity because ultrasonic actuation excites many tip-substrate vibration modes, and the phenomena more resembles lowering of friction using ultrasonic agitation. For actuated superlubricity, only resonance modes of the sled should be excited and this could not be achieved because the magnetic actuation, required for exciting just the sled, is too weak to provide sufficient vertical displacement of the sled.

The resonance frequencies of a free standing sled on a surface are the driving frequencies for actuated superlubricity. Extensive FEM analysis was undertaken to model the resonance modes of sleds attached to the process chip, completely free sleds, sleds placed on a surface, and sleds with and without a magnetic particle placed near the centre. The vibration modes are measured experimentally using a laser vibrometer and qualitatively match the FEM modeling. It is generally difficult to measure the modes of a free standing MEMS structure on a surface, and a new method is demonstrated to estimate such modes using data taken on the same structure whilst still suspended on the MEMS process chip i.e. before release. The location of the sled tips on a surface is important. Poor tip positioning can severely distort the mode shape and it was found that for successful actuation at least two tips should be distant from any node location.

In order to measure friction on the sleds, we present a new AFM based approach for measuring the friction of free standing MEMS structures. In the method, an AFM tip is brought into contact with the sled resting on a substrate. The substrate is displaced laterally and, provided the AFM tip does not slide over the plate, the twisting of the AFM cantilever is used to measure the friction of the underlying sled-substrate interface. The method can measure nano-Newton to micro-Newton forces (both friction and load) and provides a means to measure friction of macroscopic structures at low load.

Special MEMS cantilevers are also microfabricated for low friction force measurement and friction study in liquid. Ultrathin cantilevers (~300 nm thick) are fabricated with a 1 μm thick silicon massload at the free end. The use of such ultra-thin cantilevers in a pendulum AFM geometry is proposed to measure very low friction forces e.g. on lubricants, with the AFM operating in contact mode. Special cantilevers are also manufactured and characterized so that a droplet or a bubble can be reliably attached to

the free ends of the levers. The cantilevers are used as a colloid probe type AFM in aqueous solutions, enabling the drainage of water films between two approaching bubbles or droplets to be measured.

LIST OF PUBLICATIONS

To the best knowledge of the author, all the results presented in this dissertation are original, and reference are provided to the works by other researchers.

The following works were published in international journals as a result of work described in thesis:

X.S. Tang, Y.C. Loke, P. Lu, S.K. Sinha, and S.J. O'Shea "Friction measurement on free standing plates using atomic force microscopy", Review of Scientific Instruments ,84(1), 2012

X.S. Tang, Y.C. Loke, P. Lu, S.K. Sinha, G.Y. Zhou, and S.J. O'Shea "Microfabricated plates with 3-point contact for nano-to-microscale friction", Submitted to Nanotechnology

I.U. Vakarelski, R. Manica, **X.S. Tang,** S.J. O'Shea, G.W. Stevens, F. Grieser, R.R. Dagastine and D.Y.C. Chan "Dynamic interactions between microbubbles in water" *PNAS* 107 (25) (2010), 11177–11182.

O. Manor, I.U. Vakarelski, **X.S. Tang,** S.J. O'Shea, G.W. Stevens, F. Grieser, R.R. Dagastine and D.Y.C. Chan, "Hydrodynamic boundary conditions and dynamic forces between bubbles and surfaces", Phys. Rev. Lett. 101 (2008), 024501.

P. Lu, Y.C. Loke, **X.S. Tang**, S. S. Kushvaha and S.J. O'Shea, "A note on the two-spring Tomlinson model", *Tribology Letters*, 43(1), (2011), 73-76.

Oral conference presentations:

X.S. Tang, Y.C. Loke, S.K. Sinha, and S.J. O'Shea, "Microfabricated devices for friction measurements", ICMAT 2009, International Conference on Materials for Advanced Technologies, June 28 – July 3 2009.

X.S. Tang, S. Rast, E. Meyer, S.K. Sinha and S.J. O'Shea, "Fabrication of mass loaded MRFM cantilever with integrated tip and ultra-low spring constant, ICMAT 2009, International Conference on Materials for Advanced Technologies, June 28 – July 3 2009.

X.S. Tang, Y.C. Loke, P. Lu and S.J. O'Shea " Friction bridging the nano-to-micro scale with microfabricated plates", 19th International Vacuum conference, Paris, Sep 9-13, 2013

The following works were also published in international journals, and demonstrate fabrication skills in MEMS: but are not within the scope of the thesis;

X.S. Tang, S.J. O'Shea and Ivan U. Vakarelski "Photoresist Templates for Wafer-Scale Defect-Free Evaporative Lithography" Advanced Materials, 22, (2010) 5150–5153

IU Vakarelski, J.W Kwek, **X.S. Tang**, S.J O'Shea,"Particulate Templates and Ordered Liquid Bridge Networks in Evaporative Lithography", Langmuir, 2009 25 (23), 13311-13314.

Y. C. Loke, W. Hofbauer, P. Lu, K. Ansari, **X. S. Tang**, and S. J. O'Shea "Electroplated CoPt magnets for actuation of stiff cantilevers", Review of Scientific Instruments. **82** (11) 2011

LIST OF SYMBOLS

Acronyms

AC	alternating current
AFM	atomic force microscopy
C_4F_8	octa-fluoro-cyclo-butane
$C_{14}H_{30}$	Tetradecane
CAD	computer aided design
CCD	charge-coupled device
CD	critical dimension
CMOS	complementary metal-oxide semiconductor
COF	coefficient of fricition
CW	continuous wave
DC	direct current
DI Water	distilled water
DRIE	deep reactive-ion-etching
DCS	dichlorosilane
EBL	electron beam lithography
F-Si	silicon coated with fluorine terminated monolayer
FDTS	perfluorocdecyltrichlorosilane
FEM	finite element modeling
FFT	fast fourier transform
FIB	focused ion beam
GDS2	graphic database System 2
H_2O_2	hydrogen peroxide

H_2SO_4	sulphuric acid
HF	hydrofluoric acid
HMDS	hexa-methyl-di-silazane
ICP	inductive coupled plasma
IPA	isopropyl alcohol
KOH	potassium hydroxide
LDV	laser Doppler vibrometer
LFM	lateral force microscopy
LPCVD	low-pressure chemical vapor deposition
MEMS	micro-electromechanical systems
NEMS	nano-electromechanical systems
NSOM	near-field scanning microscopy
PECVD	plasma enhanced chemical vapor deposition
PMMA	poly(methyl methacrylate)
PSD	position sensitive detector
PSV	Polytec Scanning Vibrometer
PTFE	polytetrafluoroethylene
PVD	physical vapor deposition
PZT	piezoelectric
SDS	sodium dodecylsulfate
SOI	silicon on insulator
TM	tranverse magnetic

Symbols

a	side length or radius of a plate
A	contact area
B	the strength of the magnetic field
D	bending stiffness of the plate
E	Young's modulus
F_{ads}	adhesion force
F_L	lateral force
F_n	normal contact force
F_x	force in the x-direction
h(r,t)	separation between two droplets
H	magnetic field
I	current
k_c	cantilever spring constant for the normal direction
k_{eff}	effective lateral spring constant
k_{xT}	torsion stiffness of the AFM cantilever
k_{tip}	stiffness of the tip apex
$k_{contact}$	AFM tip surface contact stiffness
k_x	in plane cantilever stiffness
k_z	cantilever stiffness in the normal direction
M	magnetization
Q	quality factor
t	thickness of structure
V_n	the volume of a magnetic particle
V_{bias}	bias voltage
V_{pp}	peak to peak voltage

w	circular frequency
γ	surface energy
δ	indentation depth
Δx	discretization in x
Δt	discretization in time t
Δy	discretization in y
Δz	discretization in z
λ	wavelength
μ	static coefficient of friction
τ	interfacial shear strength of the contact
υ	Poisson ratio
Φ	phase
ω_0	resonant frequency

TABLE OF CONTENTS

LIST OF FIGURES

LIST OF TABLES

Chapter 1 Introduction

1.1 Motivation

Micro-electromechanical systems (MEMS) is a field studying micron sized objects fabricated using semiconductor processing techniques. The technology is the basis for several major commercial products, such as miniature accelerometers and fluidic devices for biotechnology.[1]

One of the most challenging aspects in the operation of MEMS is how to reduce friction when parts in relative motion come into contact. This fundamental tribology problem severely limits the type of MEMS device which can be constructed. Indeed, one can consider why there are so few types of devices in MEMS when in the macroscopic world such devices are abundant e.g. wheels, gears, motors, etc The answer is that the friction problems have not been solved in MEMS to allow two surfaces to slide past each other in a reliable manner.

Friction is an important aspect of MEMS because micro-components have a very large surface area-to-volume ratio and thus interfacial forces become predominant. The predominance of these surface forces causes adhesion. This leads to the problems of stiction, where the applied force cannot overcome static forces; extensive wear and creation of wear debris during operation; high contact shear stresses at high speeds; etc. Most of these problems lead to eventual failure of the MEMS device, particularly for Silicon which has very poor tribology properties.

An important aspect in solving friction problems is to have small surface forces i.e. to reduce the surface free energy. Overall, chemical modification of surfaces is a favoured solution as this can be easily incorporated into the fabrication process. Air bearings are another approach for rotating MEMS e.g. in hard disk drives, gas turbine structures, etc. In general, one can state that there is considerable effort being undertaken to discover methods of surface modification and boundary lubrication to reduce friction.[2,3] Current technology is able to provide special solutions for devices that operate in dry, controlled conditions, and nearly all researchers in MEMS tribology work on solving friction problems in existing devices, such as tilting mirrors[1] or in designing devices which do not have sliding surfaces e.g. comb drive actuators.

From a MEMS perspective, almost all existing research effort aims to *avoid* sliding surfaces in MEMS rather than to discover alternatives that would allow sliding devices to be manufactured. We turn the central problem around and do not avoid friction, but use it within a MEMS actuation scheme to turn sliding on and off. Such an approach is also the basis of the simple scratch drive.[4]
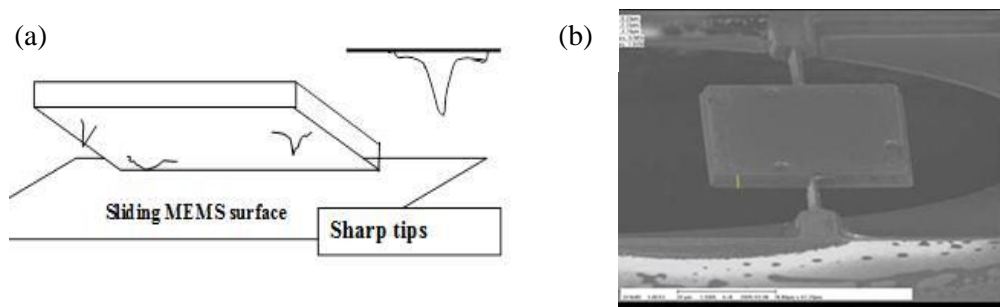
Figure 1.1 a) Schematic of the sled design. b) A fabricated sled. The sleds are made from silicon and have lateral dimensions of 100 to 300 μm, and thickness ~0.3 to 5 μm.

Our basic idea is to microfabricate simple prototypes called "sleds". The sleds consist of a silicon plate with 3 protruding tips as shown in Figure 1.1. The sleds are 100 to 300 μm in size with square, triangle or circular geometry, and the tips are made very sharp,

similar to those fabricated for atomic force microscopy (AFM). The tips form a 3-point contact when placed on a surface, and the working hypothesis is that the friction acting on the tips can be switched from high to low by changing the frequency of an external actuation force. In this Thesis, ultrasonic (piezoelectric) and magnetic actuation are used to vibrate the sled into motion. The use of a change in frequency to stop or start the sled sliding is based on the new concept called superlubricity.[5] Superlubricity is a regime of motion in which friction vanishes or becomes negligible, and our ideas were initiated after a report showing that an oscillating external electrical field could switch the friction acting on an AFM tip from a high to negligible value over a very narrow range of oscillation frequency, with the frequency corresponding to mechanical resonances associated with the AFM cantilever.[6] In this Thesis, we apply this concept of actuated superlubricity to a large, microfabricated MEMS structure, namely the sled. In this way, macroscopic pieces can be moved with low friction based on nano-tribology ideas.

1.2 Requirements for actuated superlubricity

Most requirements for superlubricity conditions appear to be achievable for a MEMS device using available technology, as shown in Table 1.1. The work presented can only explore some of these many aspects. In particular, we note that for the sled to move we must also have low friction surfaces, irrespective of whether we can actuate a superlubricity condition. Surface effects are not studied here. The methodology we adopt is as follows.

a) Thin sleds are microfabricated.

b) We use the vibration modes of the sleds to define the frequencies at which actuated superlubricity is expected to occur.

c) The sleds are placed on a surface and an external vibration is applied.

d) The frequency and amplitude of the actuation is varied and any lateral motion of

the sled across the surface is observed.

Many of the challenges that arise in our work occur because the sled is free standing i.e. un-tethered. For example, for actuation we simply cannot attach an electrode to the sled, as done for the AFM cantilever experiments.[6] Therefore, experiments had to be done to test that the general idea of external actuation of the sled is feasible, and we verified that sleds can be actuated (ultrasonically) to slide at specific driving frequencies.

Table 1.1 The general physical requirements to achieve extremely low friction sliding[5]

Requirement for superlubricity	Possible MEMS solution
Dry sliding i.e. no capillary forces	Hermetically seal
Low wear	Vapor lubrication, polymer surfaces
Smooth surfaces	SiO_2, Diamond like carbon (DLC)
High modulus surfaces to minimise contact	Si_3N_4 tips, DLC coatings
Sharp tips to minimise contact area.	Microfabricated tips, diamond tips
Low loads needed.	Use very thin plates with loads <10 nN.

The difficultly is in establishing that the underlying phenomena giving rise to the sled movement is superlubricity. We must correlate the observed sled movement with the measured resonance frequencies of the individual sled and also measure the friction forces acting as the sled slides over the surface. Combining actuation, friction and resonance data within one measurement is very challenging for free standing structures and only the individual parts have been completed within the thesis.

Firstly, one must know the sled resonances to be able to actuate motion and finite element modelling (FEM) was used to find the eigenmodes for a given sled design. In addition, we must not only excite the sled structure on a resonance, but also place the 3 tips of the sled at positions where the tips will move at resonance i.e. the tips must be placed at the vibration anti-nodes. In principle, one can manipulate the position of the tips, the mode

frequency used and the shape of the sled to achieve different actuation motion e.g. translation or rotation.

The situation is further complicated because the modes may change when the sled is placed on a surface, and we model the tip-surface contact with simple springs in the FEM simulation. This provides a link to experimental data because we have extensively modelled and compared the mode frequency and shape before the sled is placed on a surface (i.e. still suspended on the microfabrication chip by soft cantilever beams) and after being placed on the surface. This approach allows us to predict, with moderate success, the sled vibration modes when placed on a surface from measurements taken before the sled is released. This method is important because measuring the vibration of a free standing structure using a standard MEMS vibrometer is difficult; the vibration energy from the vibrometer oscillator needs to couple between the substrate and the plate, and this is very uncertain.

A final difficulty arising with un-tethered MEMS structures is to measure friction. The friction acting on the sled must be measured to verify that the friction force is low (i.e. superlubricity occurs) when the sled begins to move under actuation. The question arises, how can the friction be measured on a free standing, micron sized plate? Traditional tribometer methods and macroscopic approaches cannot be applied because the forces involved are much lower than standard commercial nanotribometers. We therefore developed a new method based on indenting an AFM tip onto the sled and then measuring the forces acting by the twisting of the cantilever, as in standard friction force microscopy. We believe this approach also has broad application to the measurement of friction on any small, free standing structure.

1.3 Thesis outline

The thesis is organized as follows:

Chapter 2 briefly reviews friction problems in sliding MEMS and possible solutions. The method of actuated superlubricity and low friction force measurements are discussed in detail to link with the present effort.

Chapter 3 discusses the experimental procedures and processes that are related to the sled fabrication, characterization and actuation. A home built AFM was constructed for the new method of measuring friction on free standing structures, and some details of the construction are described. The plate resonances were recorded using a commercial laser vibrometer. However, our experimental requirements are more stringent than typical dynamic MEMS measurements, usually limited to bulk micromachined membranes or cantilevers[7-12]. Very small displacements are encountered (<1 nm) in our experiments and the sleds can have important resonance modes up to ~900 kHz. Considerable effort was therefore made to reduce the vibrometer noise levels. We built special piezoelectric actuation stages, magnetic actuation stages, and a vacuum chamber to integrate with the vibrometer.

The work in **Chapter 4** reports the microfabrication of the sleds and the FEM simulation results. Two types of sleds, ultra-thin plate (300 nm) and thick plate (3 μm thick), were fabricated incorporating 3 sharp tips. The major fabrication challenges and their solution are described. The FEM analysis was undertaken to understand the resonance modes of sleds attached to the process chip, completely free sleds, sleds placed on a surface, and sleds with and without a magnetic particle placed near the centre. The particle is used experimentally for magnetic actuation of the sled.

Chapter 5 introduces the method to measure friction on a free standing sled, based on AFM.[13] An AFM tip is brought into contact with the sled resting on a substrate and the twisting of the AFM cantilever is used to measure the friction of the underlying sled-substrate interface. The method can measure nano-Newton to micro-Newton forces (both friction and applied load).

Chapter 6 summarizes the vibrometer measurements of the sled modes and the actuation of the sleds. Both piezoelectric and magnetic actuation are explored, and the mode results in ambient and vacuum environment are discussed. The experimental modes are compared with the simulation results, and plate mode shapes are determined. The in-plane movement of free standing sleds was observed on different surfaces (mica, fluorine terminated silicon and graphite) under piezoelectric actuation and some qualitative conclusions drawn.

Chapter 7 describe the microfabrication and characterization of special AFM cantilevers for ultra-low friction force measurements. The chapter includes the fabrication of ultrathin cantilevers (~300 nm) with a mass loading at the free end. We propose that the use of such ultra-thin cantilevers in a pendulum AFM geometry[14] can be used to measure very low friction forces e.g. on lubricants, with the AFM operating in contact mode. The chapter also describes the fabrication and characterization of special cantilevers so that a droplet or a bubble can be reliably attached to the free end of the lever. These levers were used at the University of Melbourne as a colloid probe type AFM in aqueous solutions, enabling the drainage of water films between two approaching bubbles or droplets to be measured.[15,16]

Chapter 8 provides a brief summary of the major results and suggests several problems for future work.

Chapter 2 Literature Review

2.1 Introduction

Micro-electromechanical systems (MEMS) is a field associated with integrated sensors, microactuators and Microsystems utilizing fabrication technologies that originated from the integrated circuit (IC) industry. Several MEMS passive transducers such as inertial sensors, chemical sensors and biomedical systems have been brought into market since 1980. The first commercial MEMS product in mass production was the disposable blood pressure transducer (Foxboro/ICT, Honeywell), followed by the multiaxis accelerometer (ADXL50) and digital mirror devices (Texas instruments).[17] With the advancement of nano-fabrication technology, the field of Nano-electromechanical systems (NEMS) has also immerged. However, there exist many technical obstacles related to inherent technology limitations, and a major issue relates to device tribology.

Tribology is the 'science and technology of interacting surfaces in relative motion and associated subjects and practice'. It includes the research and application of friction, wear and lubrication. Strong adhesion and friction are present because the surface areas to volume ratio is large in MEMS devices, and any contact or sliding of surfaces can dominate the device performance. The term micro/nano tribology concerns the friction and wear of two objects in relative sliding whose dimensions range from the micro-scale level down to the atomic scale. Nano-tribology measurements are generally carried out using instruments such as the surface force apparatuses (SFA), atomic force microscope (AFM) or friction force microscope (FFM).[18]

For MEMS devices where sliding surfaces are required for a motor drive, no satisfactory

lubrication scheme has yet been developed despite intensive research efforts. Hence, much of MEMS design tries to avoid sliding surfaces rather than to explore alternatives that would allow sliding devices to be manufactured. An example of actuating a micro-device motion avoiding surface sliding is the Texas Instrument's Digital Micromirror Device (DMD). Using bottom electrodes, the mirrors can be controlled in slight rotation angles Figure 2.1a). Each individual mirror is only about 16 micron across and is required to rotate ±10˚ by using electrostatic attraction.[19]
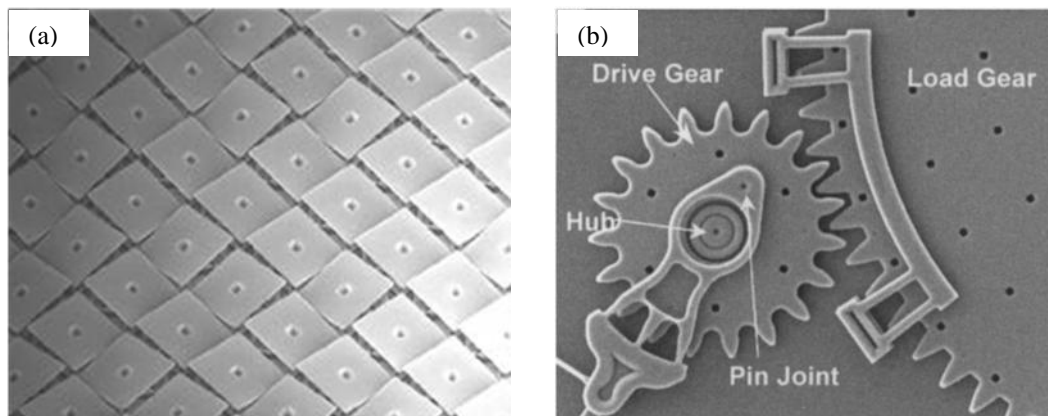
Figure 2.1 a) DVD micromirrors are shown. Stiction is reported as the main failure mechanism. b) MEMS microengines used in load tests.

Initially, significant stiction issues were observed in DMD produced from the contact between the mirror and a mechanical stop on a mirror yoke underneath each mirror. This yoke ensures that the mirror is at a correct angular position and the yoke surface can touch the mirror backside during operation. The impact of stiction, produced by adhesive forces acting at contacts, has been extensively studied.[3] Additional steps must be used, with significant cost, to curb the contact stiction, e.g. hermetic sealing, anti-stiction coating, and adding miniaturized springs to act against stiction. The methods applied are effective in minimizing the stiction issue, but they cannot entirely eliminate the problem. High driving voltages must also be employed to overcome the stiction.

Stiction in micromachines is also a topic of much research (Figure 2.1b). The micro-gears

suffer from high friction and excessive wear, resulting in very short lifetime for most applications.[19,20] The microengines cannot transfer a load particularly well, and most devices quickly fail if a driving load is applied.[21]

2.2 Possible lubrication solutions

The challenges in sliding MEMS, such as micro-gears, remains a large obstacle. Another equally troublesome problem is the excessive wear exacerbated by high friction during operation.[22] Some possible solutions from present MEMS research are discussed below.

2.2.1 Monolayer boundary lubrication

Polymeric lubricants are excellent for low friction and low wear at a single asperity contact.[23] However, polymers developed for MEMS to prevent stiction and related self-assembled monolayers (SAM), are still considered to have too high a friction coefficient for dry sliding MEMS. Also, there is always a concern for the film reliability during continuous sliding. It has been reported that during initial mechanical contact, the surface of SAM coatings can be worn off and lead to unacceptable adhesion, friction, and wear in dry operating environments.[24] A possible solution is to use liquid lubricants that lead to monolayer boundary lubrication. However, liquid lubrication of MEMS structures has not been applied for real devices because of the large hydrodynamic drag at low sliding speeds.

2.2.2 Gas lubricated bearings

A MEMS electrostatic induction micromotor supported on gas lubricated bearings has been successfully demonstrated in aerospace projects by MIT Gas Turbine Laboratory. It is a working MEMS power device which enables electrical to mechanical energy conversion.[25] A torque on the motor is produced by the difference between a potential

waveform on a stator surface and induced waveform underneath the rotor. The key is the gas acting as lubricant between the hydrostatic bearings and the periphery of the rotors. The high speed gas lubrication is realized by injecting pressured gas in the device, as shown in Figure 2.2.
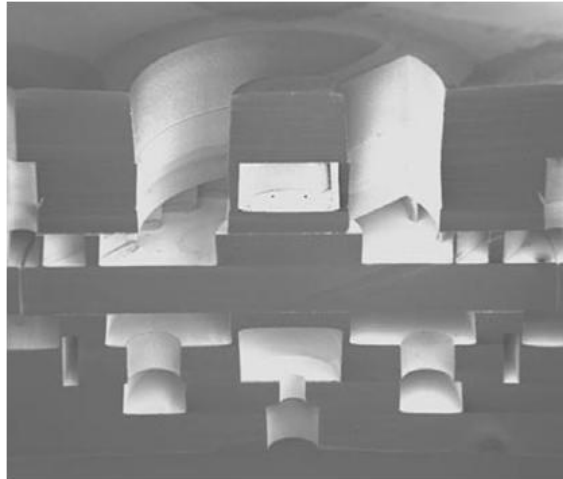
Figure 2.2 A cross-section view of a 5-layer MEMS turbine including bearings[25]

However, the fabrication of such devices is challenging. The fabrication of the MIT turbine includes 25 steps of lithography, 14 steps of silicon etching, and 14 steps of deposition and etching. The fabrication process cannot be done in a general clean room e.g. the MIT team maintained dedicated equipment. The main reason for a dedicated process tool is the requirement for multiple silicon fusion bonding. This step requires stringent surface roughness and contamination control because processes such as lithography and etching can introduce surface contamination and affect the bonding quality.[26]

2.2.3 Magnetic bearings and magnetic levitation

Magnetic levitation (maglev) technology has been used for the positioning of a moving platform in a noncontact manner. Such platforms have been reported as a precision moving stage for photolithography purposes.[27,28] Magnetic levitation is considered

particularly useful in miniaturized valves or motors, since the friction and wear primarily

are related to surface contacts on those devices. However, the magnetic levitation method

is not easy to be applied for MEMS sliding device.[29]

Wegner *et al* demonstrate a type of magnetic levitation using a piece of rare earth

magnet.[30] The magnet is glued onto a silicon thin plate and suspended by thin silicon

springs. The magnetic field is produced from a planar coil on the substrate and deflects

the plate out of the plane of the silicon substrate by the magnetic force. The design and

the resulting magnetic force are shown in Figure 2.3.
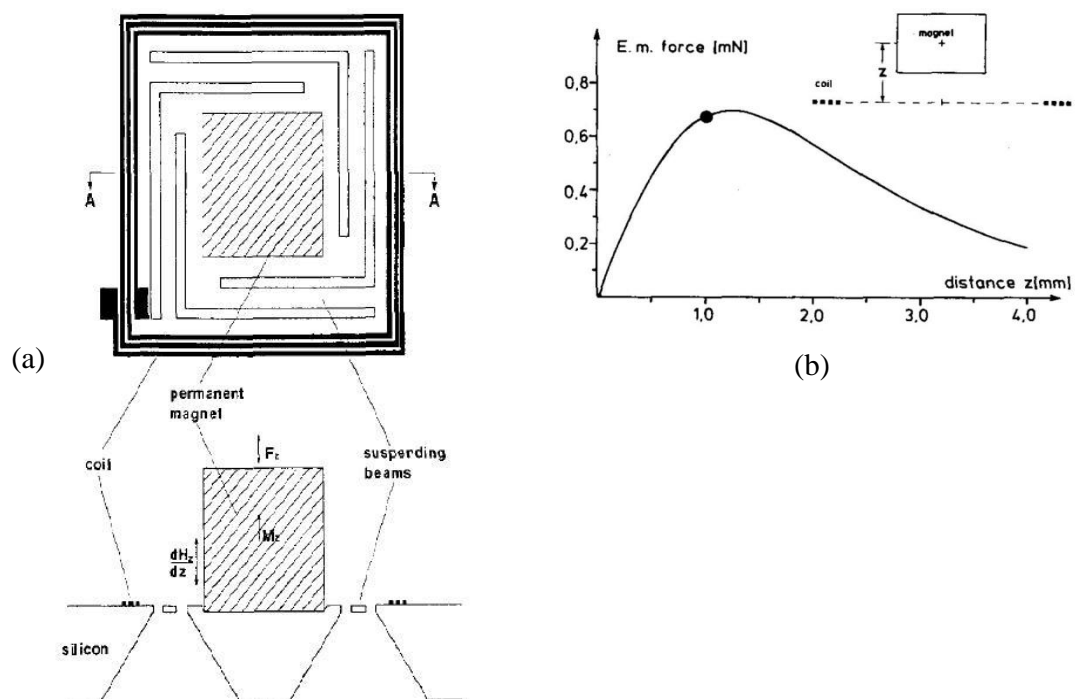
Figure 2.3 a) Schematic view of a vertical electromagnetic actuator with integrated coil and hybrid mounted permanent magnet, and b) electromagnet forces on a magnet near the planer coil.[30]

During operation, the planer coil generates a magnetic force which forces the platform to

move vertically. It is difficult to miniaturize the magnet. The force acting on the The

permanent magnet is given by,

$$F_{m,z} = M_z \int \frac{dB_z}{dz} dV \qquad\qquad (2.1)$$

where M_z is the magnetization, V the volume, and B_z is the vertical component of the magnet field produced by the coil. The magnetic force $F_{m,z}$ is proportional to the volume of the magnet. To produce large force, a NdFeB permanent magnet with dimension of 1.5 $\times$ 1.5 $\times$ 1.0 mm^3 is used and obviously such a dimension is too large to be sensibly integrated in MEMS.

Also, the magnitude of the magnetic field depends on the current density achieved in the coils, and this current in turn is limited by heating. The magnetic force in this example has a maximum value of 0.68mN at a distance 1.25mm from the coil plane (b) and the deflection of the actuator can reach ~100 μm.[30]

2.2.4 Gas phase lubrication

A method of gas phase lubrication is reported by using 1-pentanol vapor.[31] The 1-pentanol can absorb on the silicon surface and sustain a lubricating layer, which prevents wear of the MEMS surfaces and minimizes friction. Further, the lubricant layer can always be replenished from the surrounding vapor phase. This is the key attribute of the technology because even if damage occurs to the surface the lubricant will always reform a protecting layer. The main limitation to use of gas vapor lubrication is the environment control. High vacuum conditions with specific control for the gas mixture ratio are required.[31]
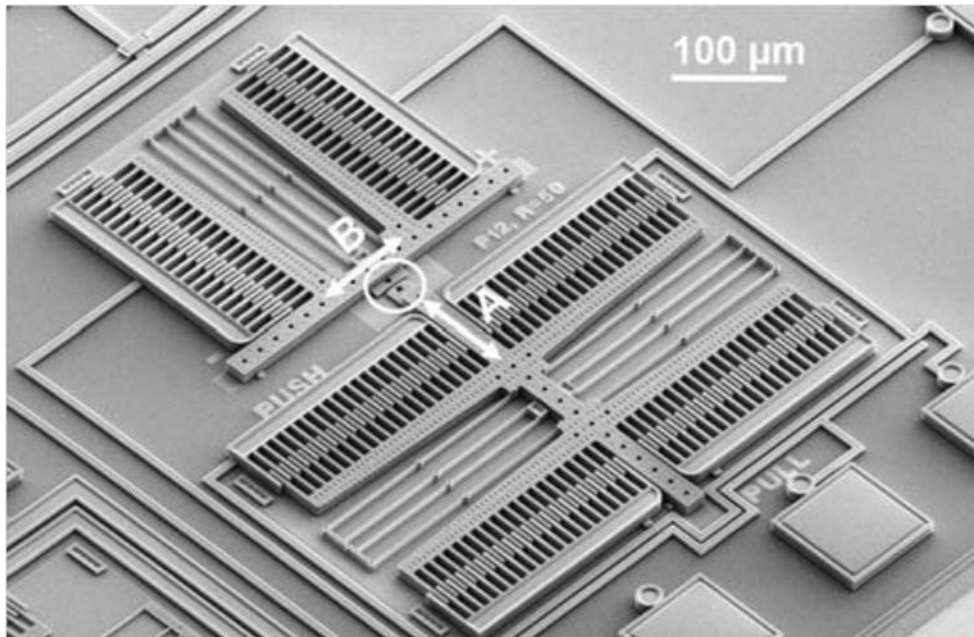
Figure 2.4 SEM image of a special MEMS tribometer used for gas phase lubrication. The sidewall contact area is encircled. Loading/Unloading actuators cause the post (Labeled ''A'') to move and come into and out of contact. Push-Pull actuators cause the shuttle (Labeled ''B'') to move laterally and shear the contact.[31]

A special MEMS tribometer is built to measure the friction coefficient in the study.[31] The microtribometer is a polysilicon device fabricated by the Sandia National Laboratories SUMMiTTM process[32], as shown in Figure 2.4. This type of MEMS tribometer is alternatively developed on SOI technology and a backside etching hole is included underneath the post in which liquid lubricant can be applied directly onto the desired region without affecting other components on the same device. The sliding performance with or without the lubricants on the sliding surface can be studied and good wear resistance is reported on the sidewall with lubricants.[33]

2.3 Superlubricity

Superlubricity is a regime of sliding motion in which friction vanishes or is negligibly small. No energy is released in the friction stick-slip process, but other dissipative mechanisms can still be present in the contact region. The existence of this low friction

phenomena was shown by Hirano and Shinjo in the early nineties.[34,35]

2.3.1 First superlubricity experiment

To introduce superlubricity, it is insightful to describe the first experiment to verify superlubricity showing the sliding of two pieces of clean muscovite mica plates.[36]
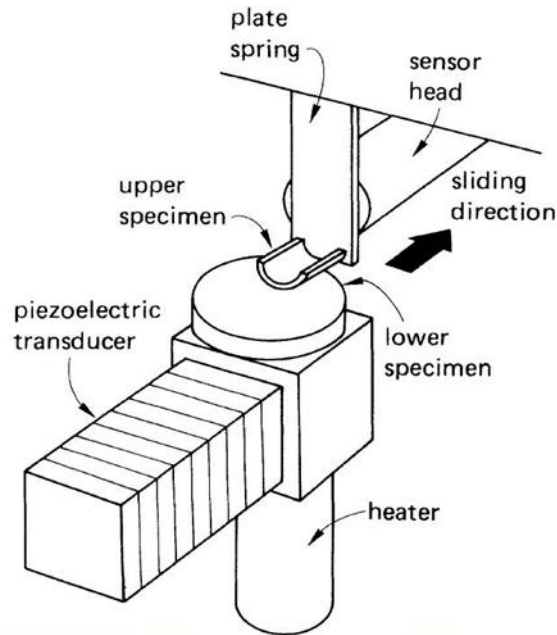
Figure 2.5 Schematic illustration of the friction apparatus reported by Hirano. The sliding direction is shown by the large arrow corresponding to the direction of extension of the piezoelectric transducer. [36]

The experimental setup is shown in Figure 2.5. One mica sheet is attached to a cylindrically curved substrate and the other to a planar disk. To control water vapor and reduce contamination, both samples were heated at 130˚ and the experiment undertaken under an argon-purged dry atmosphere. The two sheets are then brought into contact at a mean contact pressure of 0.9 MPa. Static and dynamic frictional forces were then measured between the two contacting specimens during a traverse of a few micrometers.

Figure 2.6 shows the measured static and dynamic frictional forces as a function of the lattice misfit angle θ between the two contacting mica lattices. The friction shows

anisotropy, in which the force increases as θ approaches 0° or 60°, and decreases as θ nears 30°. The angles match the atomic lattice directions of mica. Figure 2.6a also shows that no frictional anisotropy is observed under ambient conditions.

In Figure 2.6b, static forces are shown as the function of the twist angle θ_ℓ between two contacting specimens with different environment control in term of water vapor pressure and temperature. The anisotropy of the static friction varies over θ_ℓ between 0° to 90° under a dry atmosphere and at high temperature. The anisotropy is gradually weakened by increased vapor pressure and decreased temperature, and disappears under ambient.
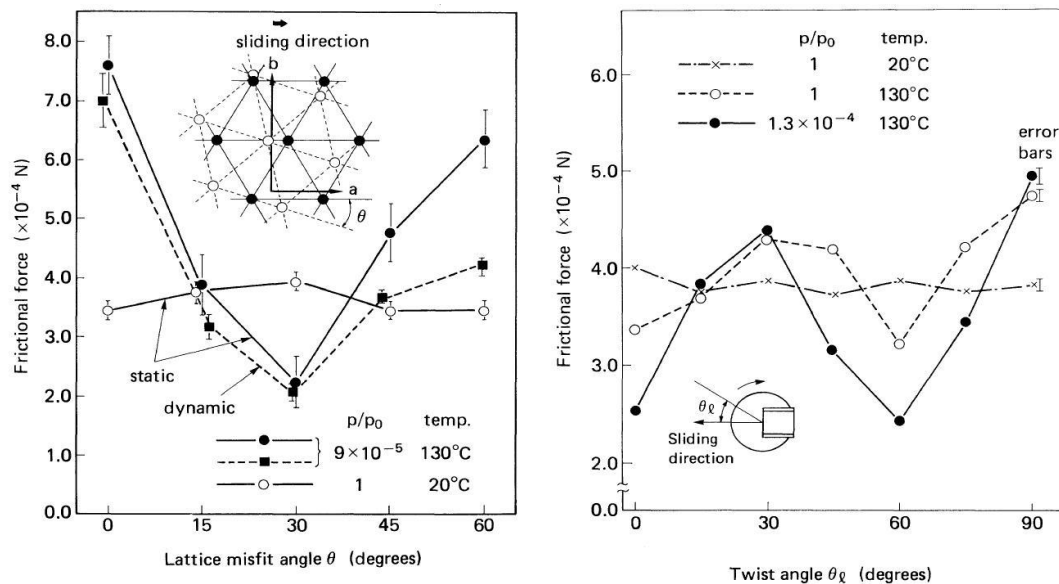
Figure 2.6 a) The measured static and dynamic frictional forces show changes as a function of the lattice misfit angle θ between two contacting mica lattices. b) The measured static frictional force is changed as a function of twist angle θ_ℓ between the two contacting specimens.[36]

2.3.2 Types of Superlubricity

The phenomena observed above by Hirano *et al* has been termed directional superlubricity.[37]

Particular crystal planes slide with much lower friction. Specifically, if two surfaces have commensurate orientation the friction will be high because the lattices can "lock" together, resulting in stick-slip motion. If the surfaces have incommensurate orientation then sliding is easier and friction lower. The effect is especially studied on graphite and graphene where very low friction can be observed depending on lattice orientation.[38]

Other mechanisms leading to superlubricity phenomena have also been defined[37] and can broadly be placed under the categories of :

    i)   The sliding of hard elastic surfaces at low load. A state of ultralow friction can be achieved when a sharp, hard tip slides over a flat surface and the applied load is below a certain threshold. The threshold depends on the tip-surface interaction and the stiffness of the materials in contact. Under these conditions, stick-slip motion disappears and hence the friction decreases. This effect has been observed by AFM[6] and is the basis of the superlubricity idea followed in this thesis.

    ii)   Chemical or chemolubricity. Friction can be greatly reduced by appropriate chemical treatment of the surfaces. Coatings with extremely low coefficient of friction have been developed e.g. specific diamond-like carbon films, molybdenum disulfide coatings.[39]

Unfortunately, superlubricity cannot be easily applied. The surfaces must be very clean and smooth. Persson *et al* have shown theoretically that even a relatively small surface roughness or a low concentration of adsorbents can completely remove the superlubricity effect.[37] The load must also be as low as possible, typically in the nano-Newton range.

2.3.3 Actuated Superlubricity

Recently, transition from stick-slip to frictionless sliding has been demonstrated using an external actuation.[6] This method was demonstrated for a single AFM tip actuated by a sinusoidal electric field, where it was found that if the electric field was tuned at certain natural frequencies of the AFM cantilever, the tip moved with extremely low friction. This phenomenon has been termed dynamic superlubricity.[40] Basically the friction can be turned "on" or "off" by applying a suitable voltage and frequency to the external actuation.
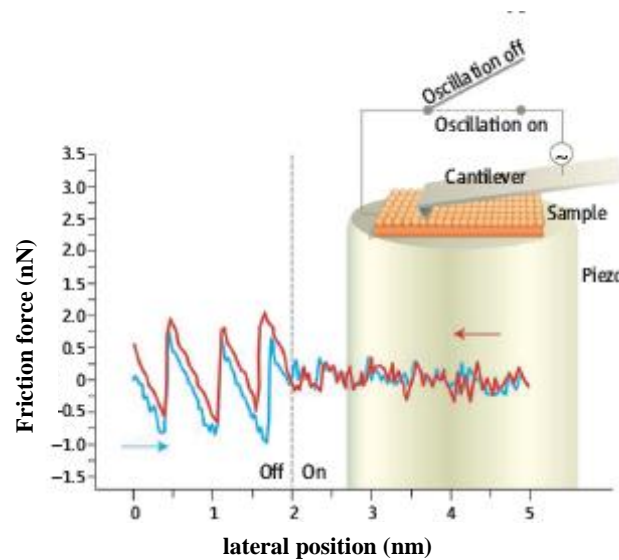
Figure 2.7 Friction in a nanometer-scale contact, in the form of atomic-scale stick-slip instabilities (left), is dramatically reduced (right) when a modulation in the normal force by an external electrostatic actuation is applied.[6]

The setup is shown in Figure 2.7. The ionic crystals KBr and NaCl are used as samples and all experiments are under ultra-high vacuum. The AC voltage for actuation is connected between a conducting AFM cantilever and a metal plate placed under the sample. Both the normal load F_N and the lateral force F_x between the tip and the sample were monitored.

A common observation for ionic crystals is atomic scale stick-slip motion, as shown for the KBr sample in Figure 2.8a. Here, the friction force sticks and then slips (i.e. slides) as the tips moves along the surface with a periodicity equal to the atomic lattice spacing. The friction increases as expected when the applied force is increased (the dotted line in Figure 2.8a).

It was found that the atomic scale friction force could be made negligibly small by applying an oscillatory voltage between the substrate and the AFM cantilever at a particular frequency, as shown in Figure 2.8b. The superlubricity effect was only observed at sufficiently high voltages and at certain actuation frequencies. The frequencies corresponded to the resonance frequencies of the cantilever in the surface normal direction (not the torsion direction) and when the frequency moved away from a natural frequency of the AFM cantilever, the tip-surface friction force returned to a high value. The transition between high and low friction was fully reversible.
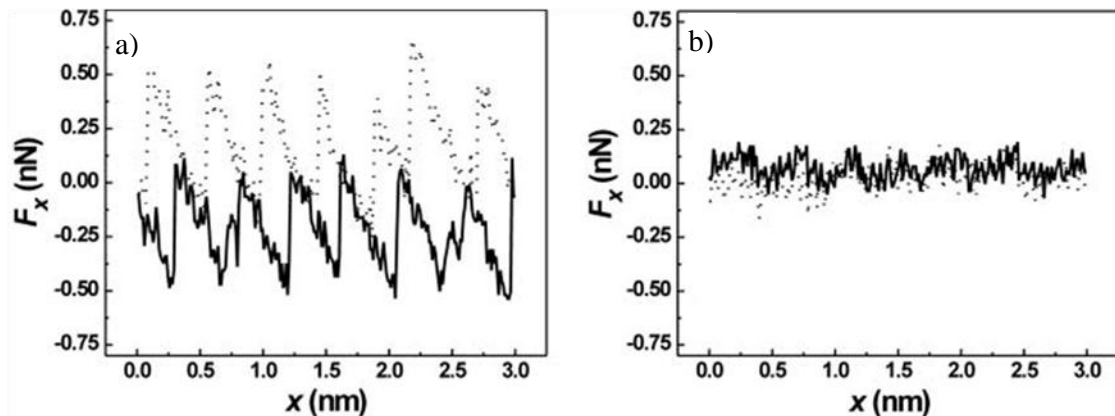
Figure 2.8 a) The lateral force F_x shows stick-slip with spatial periodicity of 0.5 nm corresponding to the atomic lattice of the surface. b) When the resonate frequency is actuated, the stick-slip disappears with negligible lateral force detected. [6]

The applied voltage causes an electrostatic force to act on the cantilever in the surface normal direction. Analysis shows that for a tip to move along the surface it must

overcome the potential barriers between adjacent sites, and the tip displacement (in the vertical direction) caused by the actuation voltage changes the energy landscape by lowering the energy barrier between adjacent sites. In effect, at a resonance frequency, the displacement of the tip in the direction normal to the surface is sufficient to "lift" the tip over the potential restricting the lateral motion.

This report suggested a practical way to control friction and limit wear in MEMS systems, and formed the basis of initiating the work presented in this thesis. The possibility of applying this phenomenon to larger sliding surfaces is very attractive when the actuation can be applied electrically or magnetically, because this opens a possible route to realistic low friction motors and robots compatible with MEMS fabrication approaches.

2.4 Measuring very low friction forces

The creation of low friction devices and systems is very challenging. Equally challenging is the measurement of ultra-low friction in such systems. This is particularly the case for MEMS because the contacting area is small and this means that the overall forces acting are also small. For example, in our work we require friction measurements in the nano-Newton range on a relatively large MEMS structure (~100 µm size). This problem is discussed in Chapter 5 but we note below some additional background information.

Friction is usually measured using a tribometer, such as the classic pin-on-disc arrangement. However, commercial tribometers (even so called nano-tribometers) cannot measure either lateral friction or normal forces in the nano-Newton range. Specially designed approaches for nanoscale work are required. Nano-indentation can also be adapted for friction measurements on surfaces, but again suffers from a lack of resolution,

both force and spatial.

For the characterization of surfaces and lubricants used for MEMS, specialized tribometers can be microfabricated. Examples are the Sandia micro-tribometer shown in Figure 2.4[41], and the Leiden MEMS tribometer for dynamic friction measurement[42]. These tribometers are suitable for tribology studies of MEMS surfaces but cannot be used for more general investigation of MEMS structures (e.g. a sled) because the tribometer design is very specific (usually a comb drive type structure).

AFM can also measure friction, using the adaptation called friction force microscopy (FFM).[43,44] Basically, when an AFM tip slides along the surface, frictional forces can arise and can be measured by monitoring the twisting of the AFM cantilever. In comparison to macroscopic friction experiments, AFM measure the friction at a single asperity contact. This is an important attribute because the sliding and contact mechanics of a single asperity forms the basis of all mechanisms leading to friction.

In FFM it is difficult to extract absolute values of the friction forces because the contact area and tip geometry is usually not well known. However, AFM offers the best means to measure ultra-low forces. It has been demonstrated that measurements even at the atto-Newton scale are possible[45] using a pendulum mode AFM setup[46] in *non-contact* mode operation. We also explore the use of pendulum mode AFM but suggest that the method can be adapted for measuring ultra-low friction with the tip *in contact* with the substrate. We further adapt AFM methods to the measurement of friction on a MEMS device (a sled) and show that using AFM approaches can push down the force detection limits for MEMS to the nano-Newton range.

2.5 Summary

This chapter briefly reviews friction problems in sliding MEMS and possible solutions. The method of actuated superlubricity and low friction force measurements are discussed in detail to link with the present effort.

Chapter 3 Experimental Procedures and Processes

3.1 Microfabrication

3.1.1 Standard microfabrication processes

Microfabrication forms a major part of the thesis and standard silicon based microfabrication techniques (lithography, deposition, etching, release) have been used throughout. Processing is undertaken in a class 1000 cleanroom, except for lithography which is done under class 100 conditions. The microfabrication steps are simply introduced below and any discussion is limited to methods or processes which differ from standard procedures. Further details of specific new steps developed are described later for the fabrication of the sleds (Chapter 4) and specific AFM cantilevers (Appendix).

3.1.1.1 Lithography

Mask aligner based lithography is most often used in this work. The mask aligners used are Suss MA8 with a wavelength of 405nm and Suss MA6 with a wavelength of 365nm. The alignment resolution is 1µm on the front side alignment and 20µm on the backside alignment.

Different types (positive and negative tone) of photoresists and polymer films are selected based on the sample topology and the processes to be used after lithography. We have developed recipes for AZ9200 photoresist that can provide a photoresist thickness of 100µm suitable for lithography. The thick photoresist allows for pattern transfer on substrates with varying topology, and a smooth photoresist coverage around etching cavities up to 30µm. The thick photoresist is especially useful for local metallization or

post-process of the MEMS devices made by deeply etched features, and is used to support dry etching and plating.

3.1.1.2 Low pressure chemical vapor deposition (LPCVD) processes

This module adds a thin layer on a silicon sample surface. The samples are first thoroughly wet chemical cleaned and are then loaded in a high temperature furnace. In the thermal growth, wet oxidation and dry oxidation are used.

This thesis work includes forming sharp nitride tips on the thin sled devices. For LPCVD nitride, low stress (LS) nitride and stoichiometric nitride processes are used. Both recipes are run in the same tube with different process parameters. LS nitride films have lower stress value (~600 MPa) than stoichiometric nitride film of the same thickness (~1200MPa); however LS nitride films tend to produce more particles. The stress effects are particularly important when sleds formed from large silicon plate as thin as 300nm are made. If excessive stress is present, the final thin sled curls and distorts after the structure release.

3.1.1.3 Etching

Either wet etching by solution or dry etching are used. In wet etching, potassium hydroxide (KOH) is used to etch cavity structures in silicon. Buffer oxide etchant is applied to etch oxide layers to release the MEMS devices. In dry etching, plasma etching, reactive ion etching (RIE), deep reactive ion etching (DRIE) and XeF_2 vapour etchings are used in this thesis. The dry etching tasks include forming and sharpening the silicon tips on the sled device using a combined RIE and DRIE dry etching technique.[47]

A submicron dry etching recipe on silicon has also been developed with the ZEP 620 photoresist patterned by e-beam lithography as the mask. In the typical Bosch DRIE recipe, two repeating steps are followed: a step of sidewall passivation by C_4F_8 plasma and a following step of silicon etching by SF_6 plasma. However, the Bosch recipe is unable to etch submicron features on silicon. In the recipe we developed, two steps are still used but SF_6 and C_4F_8 gases are flown together in Step 1 enabling in-situ sidewall protection while etching is on-going. Step 2 consists of cooling and pumping the sample to remove reactive species from the submicron features. Parameters such as pressure, power, and gas flow combinations are fine-tuned to achieve the best sidewall profile. With the established recipes we are able to process submicron features or fabricate a silicon device on SOI wafer with a device layer only 340nm thick. In this thesis, this process is used to fabricate the ultra-thin sleds (Chapter 4) and ultra-thin cantilevers (Appendix A).
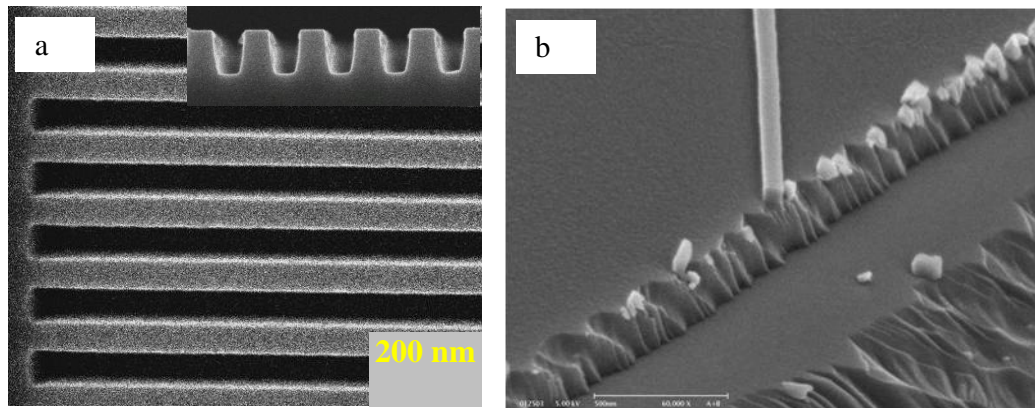
Figure 3.1 SEM micrographs illustrate results of submicron dry etching recipes on silicon. a) A grating structure of 220nm width. The insert shows the profile. b) A single silicon submicron beam of 50nm width is produced while most of the silicon is removed.

Etching results for two types of submicron silicon features are shown in Figure 3.1. Different parameters are used since the gas loading are different depending on the exposed silicon. In Figure 3.1a, only a small portion of silicon is etched away from the grating and most of the sample is covered by photoresist. In Figure 3.1b, most of the

silicon is etched away, leaving the submicron line protected by photoresist. Notably this etching result is achieved on SOI wafer and etching is stopped on the oxide layer. The result demonstrates that the recipe does not generate footing effects and the final surface and silicon profile is clean.

3.1.1.4 Metallization

Thermal evaporation, e-beam evaporation and sputtering are used to deposit thin layers of metal on the sample surface. The main consideration of the metallization is the stress on the thin devices and post-metallization processing.

In electron beam or thermal heating of a source material, metal is deposited onto a substrate directionally from the source, and thus has a poor step coverage. This coverage effect is utilized for the lift-off process. Metal evaporating and lift off is usually conducted to form patterns when the particular metal is difficult to be etched away.

Sputtering is generally applicable to all materials. Since the ejected atoms are energetic, their high surface mobility leads to good step coverage. Sputtering is normally not suitable for a lift-off process, and additional lithography and etching are required if a metal feature needs to be fabricated.

Electroplating is a useful method for producing a thick metal layer onto a substrate, although the metals are typically limited to nickel, copper and gold. We have fabricated thick nickel blocks and Co-Pt hard magnet alloys on silicon cantilevers, as shown in Figure 3.2.[48] Pulse plating is adopted as it improves the properties of nickel such as grain size, smoothness and internal stress.[49] The electroplated magnetic materials can be used to actuate the cantilever. In this thesis, magnetic particles are glued to sleds to enable magnetic actuation (see 3.1.2.3) because the incorporation of electroplating in the sled

fabrication process would make the microfabrication unnecessary complicated. However, in principle, sleds could be made in future with integrated microfabricated magnets.
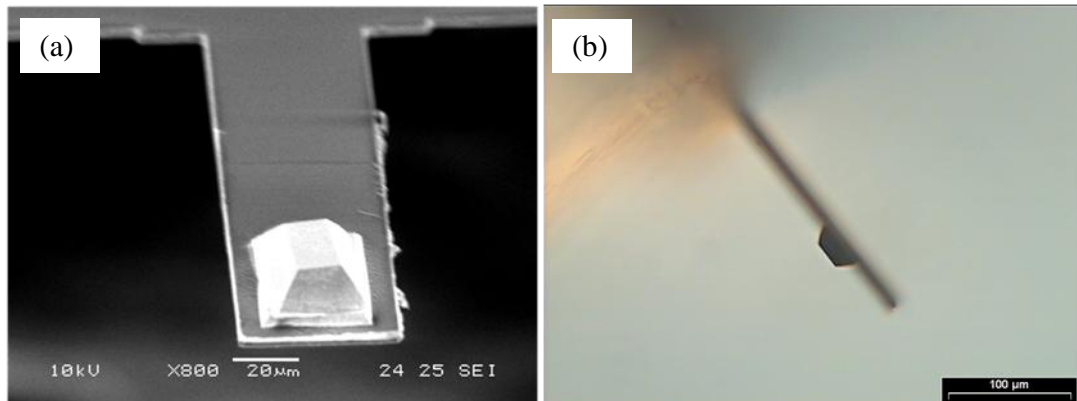
Figure 3.2 a) SEM micrograph of an AFM cantilever with a pyramidal nickel block as magnet. b) Optical image of the nickel plated AFM cantilever.

3.1.1.5 Release of MEMS devices by wet etching

Release is the last step in the MEMS fabrication of sleds and special cantilevers in this thesis. Release is generally performed by sequentially immersing the samples in several beakers filled with solutions.

In a typical release, a chip is first transferred to a the solution of buffer oxide etchant, such as hydrogen fluoride (HF) or buffered hydrofluoric etchant (BHF). The oxide layer is removed and free standing MEMS devices are formed on the chip. The liquid surrounding the sample is then replaced by transfer through an ordered sequence of different solutions. DI water, methanol and isopropyl (IPA) are generally used as the replacement sequence. In the final step, the chip is transferred out of IPA and is air-dried.[50] In each transfer, careful handling of the sample is critical since agitation could break the microstructure. The sample is generally kept in each new solution for at least 20min after transfer.

3.1.2 Special microfabrication processes developed

3.1.2.1 Release of mini-size chips

Mini-chips of size of $2 \times 2\text{mm}^2$ containing released sleds are required for two of the characterization methods, namely sled vibrometer measurements using piezoelectric (PZT) activation (see 3.3.3) and initial magnetization of ferrite particles placed on the sled (see 3.1.2.3). The small size chip is needed because of space restrictions in the test setups. During particle magnetization the chip with the sled and attached particle must be inserted into the gap between the poles of a permanent magnet, and the pole gap is ~4mm wide. In PZT actuating, it was found that a low noise floor was only achieved if the PZT actuation plate was of small area (about $3 \times 3\text{mm}^2$) and no portion of the MEMS chip extended off the PZT plate.

It is not possible to mechanically dice a large chip with sleds to a smaller size, as most of the devices will be damaged. In our approach, laser dicing (355nm pulse laser, power 1.6W) is used before sled release to define grooves delineating 2×2 mm areas on a large 1×1 cm chip. By suitable adjustment of the groove depth, the 2×2 mm areas can be broken off manually along the dicing lines (Figure 3.3c).

Particles are produced by laser dicing and manual break off as seen in Figure 3.3a. The particles must be removed; otherwise the sliding of the sled maybe impaired. By trying various release methods, it was found that only a solution based wet release can remove the particles. Figure 3.3b shows the same chip in Figure 3.3a after the wet release process.
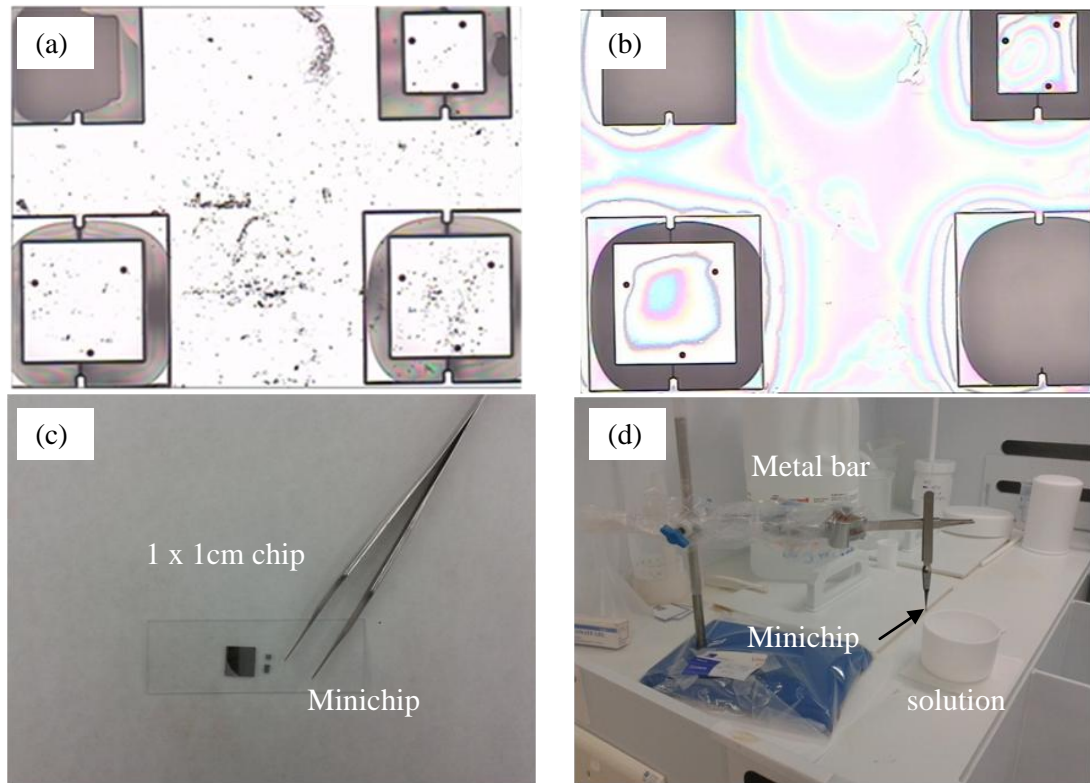
Figure 3.3 Minichips fabricated with released sleds a) The minichip after laser dicing and manual breakage. b) The same minichip after wet release. c) The dimension of a released minichip versus a normal 1 by 1cm chip. d) Simple minichip setup for wet release.

The sleds on a mini-chip can be released by the wet solution methods described in 3.1.1.5. However, special care must be taken when the chip size is small. Figure 3.3d shows the simple setup for minichip sled release. A metal bar is used to hang the chip and can be steadily moved up and down vertically along a shaft.   The chip is positioned perpendicular to the solution and the chip can be gently transferred in and out of the solutions with the smooth movement of the metal bar.

3.1.2.2 HF vapor etching release developed for MEMS/NEMS

The yield of devices depends heavily on the process control in the release step. In a standard release method, solution based HF/BHF and water are used and capillary forces are always present and can cause stiction. The transfer of the sample between different liquids is risky. For nanometer scale structures (NEMS), this standard wet release

method is not suitable. Various approaches are described in the literature, such as supercritical phase drying and freeze sublimation drying.[51] However, those techniques require a complex setup. HF vapour etch release is an alternative approach and the technology can be developed in a research lab environment.[52]

We designed and constructed a simple HF vapour etcher in a well-ventilated acid wet bench hood. The setup, shown in Figure 3.4, comprises 1) a Teflon acid beaker, 2) a customized PTFE chuck with suitable hole sizes, 3) a Teflon plate embedded with heater, and 4) a calibrated temperature controller.

HF solution is put inside the Telflon beaker. A fabrication chip with devices is put on top of the PTFE chuck with the etching surface facing the acid. The Teflon plate heats the sample to a chosen temperature (typical range from 28–33°C). The chuck design maintains a very small gap (~100μm) between the chip and the heated Teflon plate. Thus the devices are not damaged accidently when the Teflon plate is removed for device inspection.

The chemistry of SiO_2 etching by HF vapour generally follows two steps[53]

$$\text{Step 1} \quad 6HF + SiO_2 \rightarrow H_2SiF_6 + 2H_2O \tag{3.1}$$

$$\text{Step 2} \quad H_2SiF_6 \rightarrow SiF_4 + 2HF \tag{3.2}$$
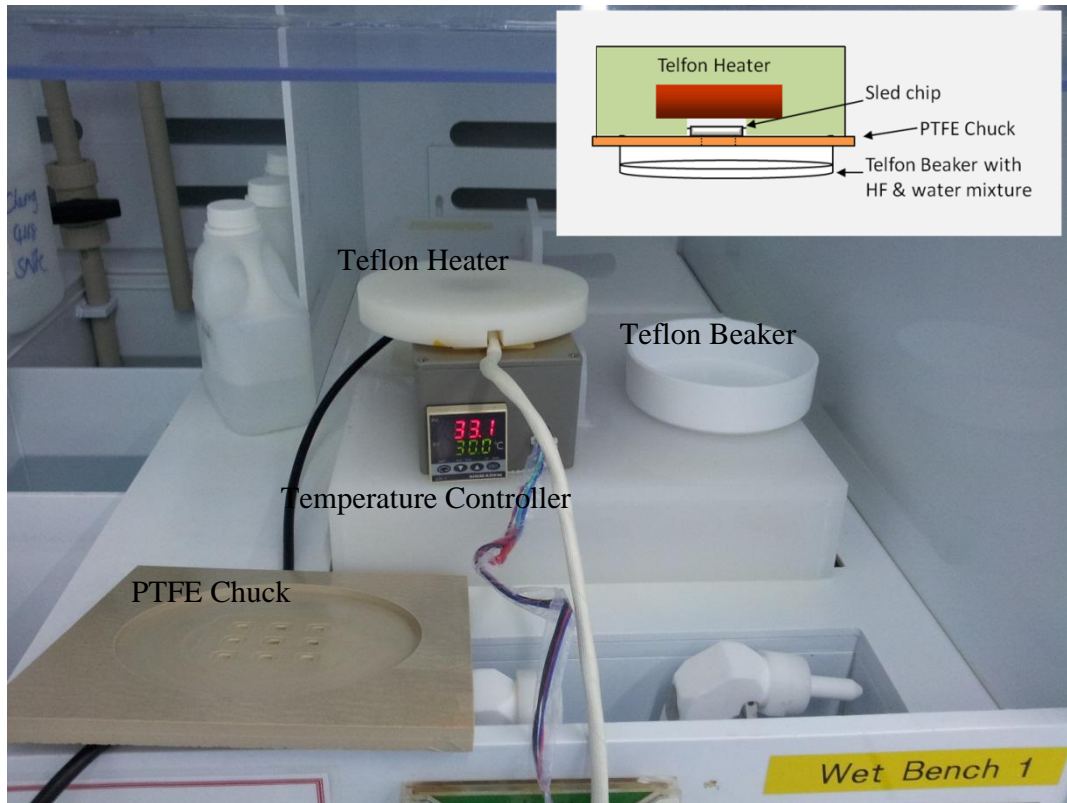
Figure 3.4 The components of the HF vapor etcher and a running set up is schematically shown in the inset

The key factor necessary for the etching is the surface adsorption. Water and HF are first produced in the gaseous form, and adsorb on the SiO_2 surface. The adsorbed water catalyzes the HF etching of SiO_2. The water on the etched surface is controlled by the HF and water mix ratio, the heating temperature and the humidity. Since the cleanroom humidity (RH) is maintained at 45-50% and a fixed mix ratio (49% HF: H_2O= 1:1) is used, the etch rate is strongly dependent on the temperature of the MEMS chip.

In our testing, the etch rate of SiO_2 is inversely proportional to the MEMS chip temperature. A high temperature inhibits the presence of water and results in a drop of the SiO_2 etch rate. However, a low temperature will promote moisture formation on the silicon surface and give rise to stiction. The best process condition for thin sleds is a chip temperature setting of 31 to 33°C, giving a thermal oxide etch rate of about 55nm/min with minimum water moisture formed.

The setup is especially suitable for releasing a NEMS device with a whole oxide etching area smaller than $100 \times 100 \mu m^2$. It remains challenging to release devices if the sample etching area is more than $100 \times 100 \mu m^2$.

3.1.2.3 Sticking a magnetic particle onto a sled and magnetization

For magnetic actuation, a magnetic particle is glued onto a 3μm or thicker sled. It was found to be impractical to glue magnetic particles on thin sleds (300 nm thick) since the structure is too delicate. The magnetic particle (Iron oxide, Magnequench, www.magnequench.com) is in the form of a powder with diameter range from 30–70 μm. Large particles are preferred to increase the magnetization volume and hence provide a large actuating force. Such particles have been used for magnetic actuation of AFM cantilevers.[54,55]

A home-made 3-axis micron-positioner with a thin gold wire as probe (60μm diameter) is used for the particle gluing. The gluing process is monitored under a long working range microscope. The sled backside is deeply inside a release hole and careful methods of picking up, releasing and aligning the particle inside the hole are needed.

The method of gluing is schematically shown in Figure 3.5. A chip containing sleds is put onto a probe station with the sled tips facing to the probe station stage. The soft metal wire is used to apply a small amount of vacuum glue (Ablebond 2025D from Ablestik, USA) onto the backside surface of the sled (Figure 3.5a). Since adhesion exists between the glue and the wire, detaching the wire from the sled must be done carefully; otherwise the adhesion force can break the sled. A magnetic particle is selected, picked up by another wire and placed onto the glue (Figure 3.5b). It is important that the particle is picked up on the tip apex of the wire to ensure the particle can touch the glue during the

placement. The exact location of the particle on the sled is difficult to control because 1) both the particle and the glue appear black under the microscope illumination, 2) the wire blocks the view at high magnification, and 3) reflection from the backside surface degrades image quality.
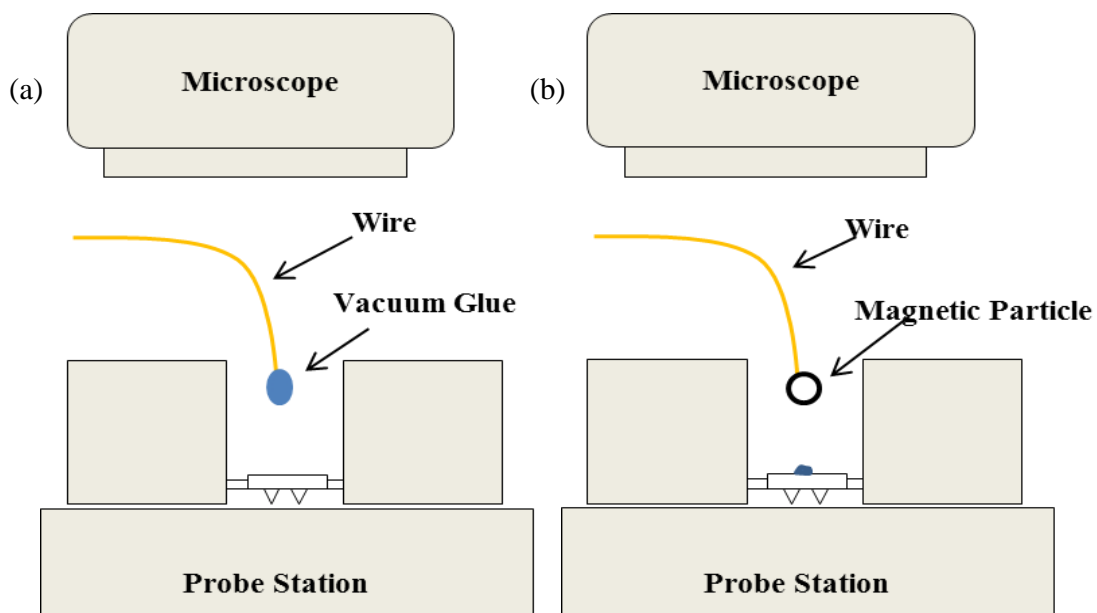
Figure 3.5 Schematic diagram to illustrate the gluing of a magnetic particle onto a sled. a) Vacuum glue is applied on the sled backside. b) A magnetic particle is dropped on the sled backside.

The vacuum glue is cured by heating in an oven (130 C° for 45 min) and the magnetic particle is firmly held to the sled surface, as shown in Figure 3.6.
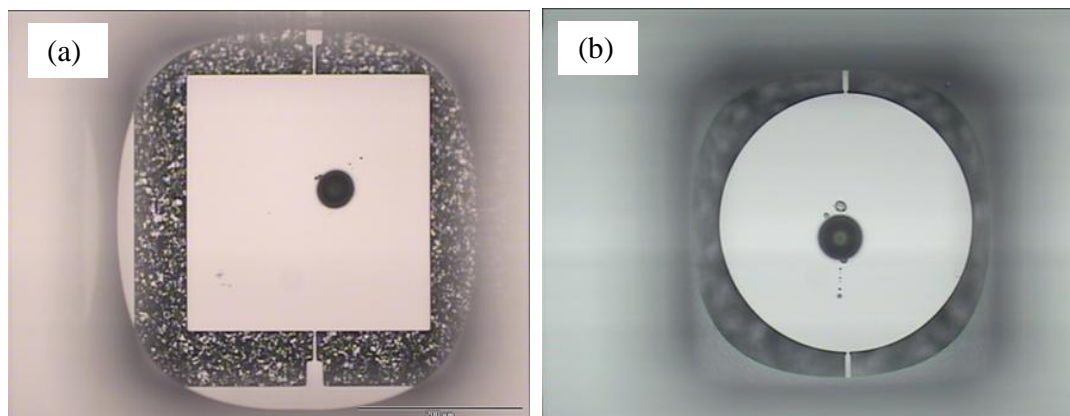
Figure 3.6 A magnetic particle is glued onto the backside of a square sled (a) and a circular sled (b).

After the magnetic particle is glued, the particle is magnetized in a chosen direction. Two methods were used. In the early experiments, the micro-chip containing the sleds was placed onto a metal rod and inserted into a ~4mm hole cut into a circular permanent magnet (Figure 3.7a). The magnetization field is measured to be ~0.9T, which is slightly less than the saturation magnetization of ferrites (~1.6 T).

Recently an electro-magnet has been used (Figure 3.7b), with a magnetization field of 1.4 to 1.6T. The pole gap separation is adjustable and even large 1×1 cm chips can be accommodated. Also, the chip can be orientated inside the pole gap allowing the magnetization direction to be readily defined.
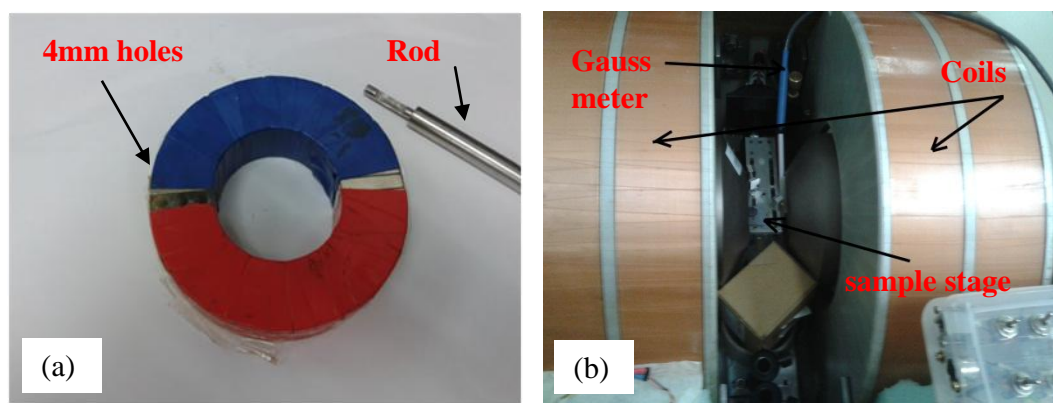
Figure 3.7 a) Permanent circular magnet used in early particle magnetization work. The metal rod holds the sample chip and is inserted into the ~4mm magnet hole. b) Electro-magnet used in later work for particle magnetization.

3.2 Atomic force microscopy

3.2.1 Introduction

The link between Microfabrication and AFM is strong because the core AFM technology involves the fabrication of cantilevers and nanoscale sharp tips. These issues will be discussed more fully in the following chapters.

Atomic force microscopy (AFM) is directly used in this work to measure friction forces on a sled (Chapter 5). As such, a brief description of AFM and also a new AFM we have constructed will be given below.
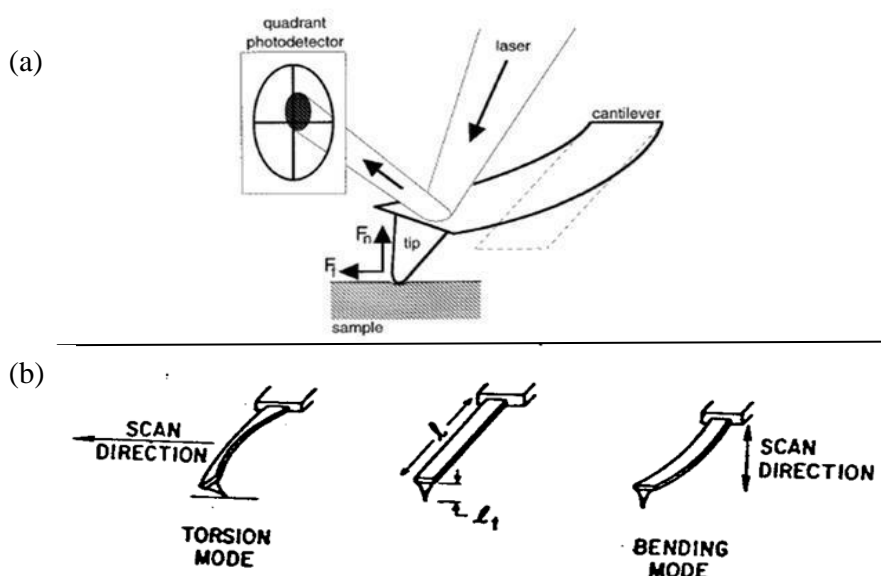
Figure 3.8 showing a) Diagram of the AFM setup for the optical beam deflection method b) Schematic showing the main cantilever modes used for AFM, the bending mode in the surface normal direction and the torsion mode in the lateral (friction) direction.

AFM is the most versatile scanning probe instrument.[56] In most AFM, a laser beam hits the cantilever and is reflected to a four quadrant photo-detector (Figure 3.8a). The normal deflection and lateral deflection of the cantilever cause a shift in laser position on the photodetector in either the vertical or lateral direction, respectively, which can be independently monitored to generate information about topography (the vertical signal) and friction (the lateral signal). This simple technique can readily measure cantilever deflections in the order of ~ 0.1 Å or lower.[57] Further, knowing the cantilever spring constant for the normal (k_c) and torsion (k_L) cantilever bending allows the normal force (F_n) and friction force (F_L) acting on the AFM tip apex to be found (Figure 3.8b).[43]

3.2.2 AFM imaging and control

Various modes of operation are available for AFM imaging. Contact mode can be used to measure the forces at the tip by measuring the static deflection (Δz) of the cantilever, and $F_n = k_c \Delta z$ provides the simplest possible measurement of the force acting. In this thesis, contact mode is used to measure the forces on drops and bubbles attached to special cantilevers in liquids (Appendix B) and a new contact mode measurement for AFM operating in the pendulum geometry is proposed (Appendix A). Importantly, contact mode control is also required in the measurement of friction or lateral forces acting between an AFM tip and a surface.

In lateral force microscopy (LFM) the tip is scanned over a surface and the lateral twist of the cantilever (Figure 3.8b) gives information about variation in friction acting between the AFM tip and the sample surface. On very smooth or atomically flat surfaces, the lateral twist due to topographic effects can be neglected, and the lateral twist will only be due to the variation in friction acting on the tip.

The introduction of LFM in 1987[43] invigorated the entire field of tribology because LFM enables the measurement of friction at a single asperity contact, which is the basic starting point of all fundamental friction studies. The technology has been applied to dry sliding[58], solid boundary lubricants[23] and liquid lubricant films[59]. Indeed, most samples in air are covered by a "lubricating" thin layer of water and other condensed contaminants. These contaminants often form a capillary bridge between the tip and the sample, generating large adhesive forces in addition to friction, also referred to as capillary forces.

In this thesis, the LFM approach is used to measure the friction between a microfabricated sled and a surface (Chapter 5).

3.2.3 High Vacuum AFM

For AFM friction measurements on microfabricated devices it is desirable to have an easy access, controlled environment from vacuum to gas phase; the ability to position the AFM tip at any chosen location on a device; and a range of movement from nanometre to centimetre of both AFM tip and the sample. Since no commercial AFM is available to satisfy all these requirements, a purpose built AFM was constructed (Figure 3.9). The setup consists of a high vacuum chamber (10^{-7} Torr) with gas feed through enclosing the AFM for controlled environment. The sample device is mounted onto a tube type piezoelectric scanner (Staveley Sensors EBL#2, 1/4" diameter, 3" long), giving a large ~120μm square scanning area. The entire piezoelectric scanner is itself mounted on a 3-axis Attocube^{TM} piezoelectric for precise positioning and coarse approach of the sample plate with respect to the AFM tip. The AFM cantilever holder is fixed and a 3-axis stage moves a miniature laser diode such that the focused laser beam strikes the AFM cantilever. A camera (Edmund Optics EO 3112C with long focal length lens) is placed above to view the relative alignment of the AFM tip and the sample. Surface imperfections and scattering can be used to observe the relative motion of both the sled-cantilever and sled-substrate movement. The image quality can be rather poor, depending on illumination and the type of substrate, and this limits the smallest detectable movement of the plate (optical resolution of ~3.4 μm).

To reduce noise, the AFM is placed on a Viton O-ring vibration stack resting on the base of the vacuum chamber. The vacuum chamber is placed on a vibration isolation table and the vacuum pumps (a rotary and turbo-molecular pump stack) are connected by a flexible hose. All wiring runs through vacuum feed throughs to connect to the appropriate electronics (AFM controller, piezoelectric high voltage amplifiers, Attocube 3-axis controller, photodiode current amplifiers).

A 4-segment position sensitive photodiode (PSD) is used as the photodetector in the AFM instead of a more typical split quadrant photodiode[60] because this allows the absolute deflection of the laser beam to be found directly.[58]
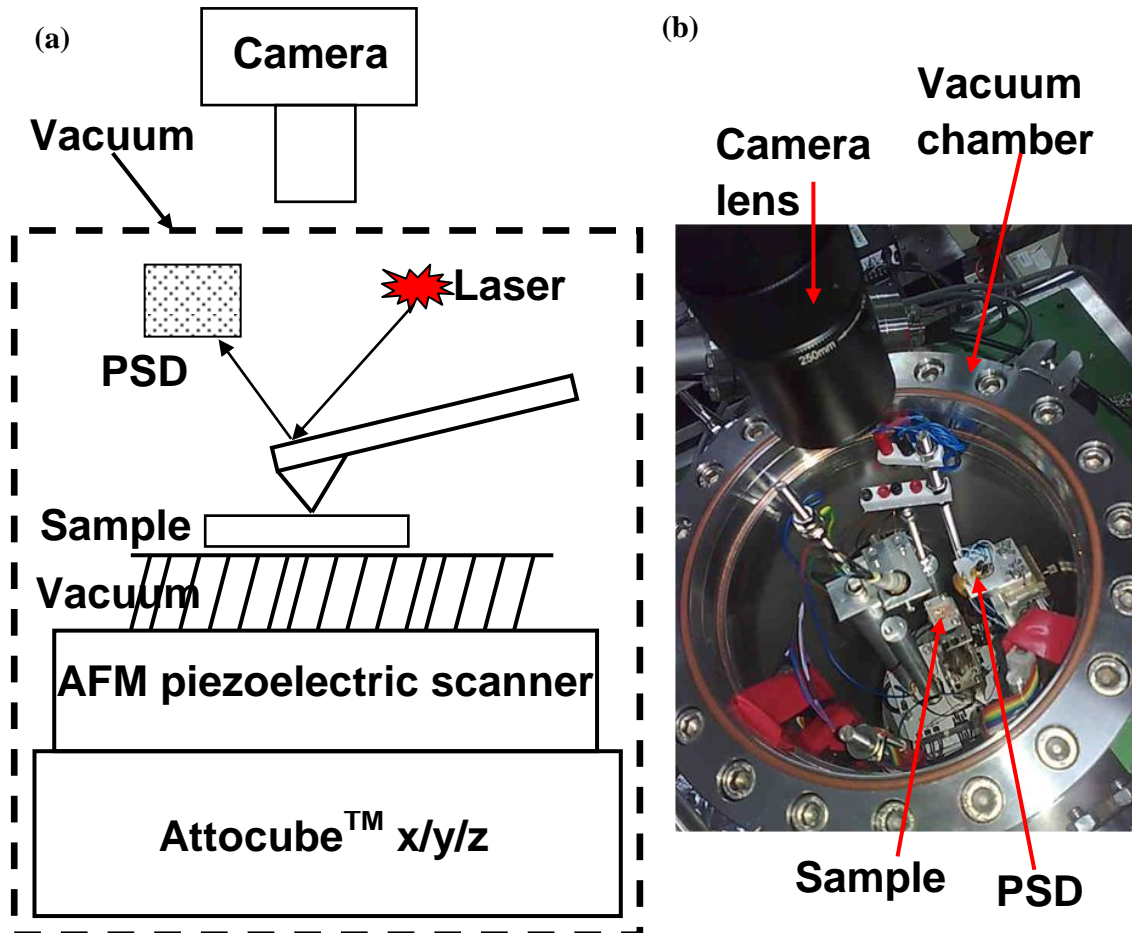
Figure 3.9 Basic outline of the home built AFM constructed for the study. (a) Schematic showing the major features of the AFM (video camera with long focal length optics, high vacuum chamber, AttocubeTM 3-axis positioner). The sample is mounted on the piezoelectric scanner. A position sensitive detector (PSD) is used. (b) Photograph of the AFM sitting inside the vacuum chamber. A glass load-lock window covers the top flange.

3.3 Vibrometer and Actuation

3.3.1 General

A commercial Polytec Scanning Vibrometer (PSV) 300-F is used to experimentally determine the modal shapes and natural frequencies of a sled. The heart of the PSV is a

laser Doppler vibrometer (LDV), which measures the surface velocity and allows non-contact vibration measurements of a surface to be made. Various optical and stage fittings were constructed to hold the sled chip during measurement, including a vacuum enclosure.
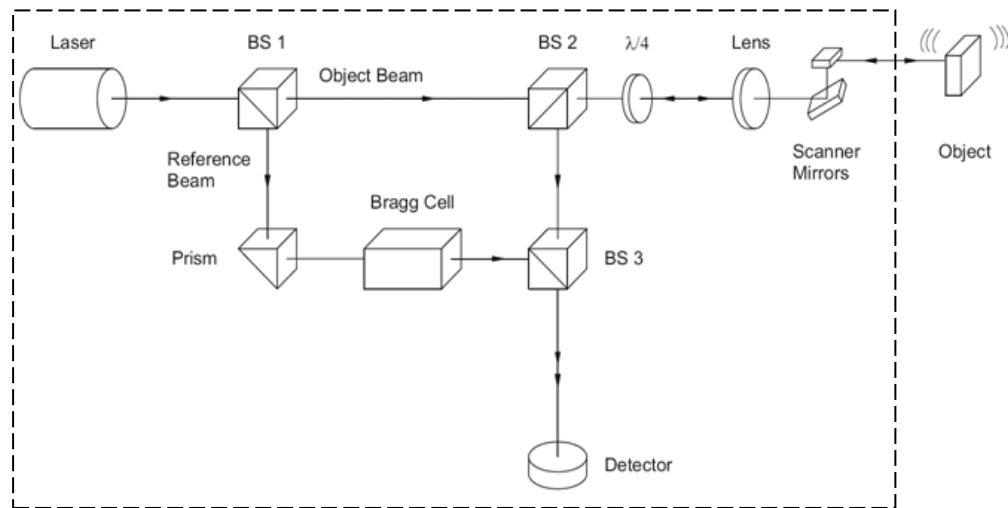
Figure 3.10 The schematic configuration of the PSV head[62]

Figure 3.10 shows the PSV head. A helium neon laser provides a linearly polarized beam. The polarized beam splitter BS1 splits the beam into an object beam and a reference beam.[62] The motion of the sample target adds a Doppler shift to the object beam frequency given by $f_d = 2 \times v(t) \times \cos(\alpha)/\lambda$, where $v(t)$ is the velocity of the target as a function of time, α is the angle between the laser beam and the velocity vector, and λ is the wavelength of the light (633nm).

The velocity of movements arising from sample vibrations can thus be extracted from the Doppler shift. The output of the PSV is a continuous analog voltage that is directly proportional to the object velocity component along the direction of the laser beam.
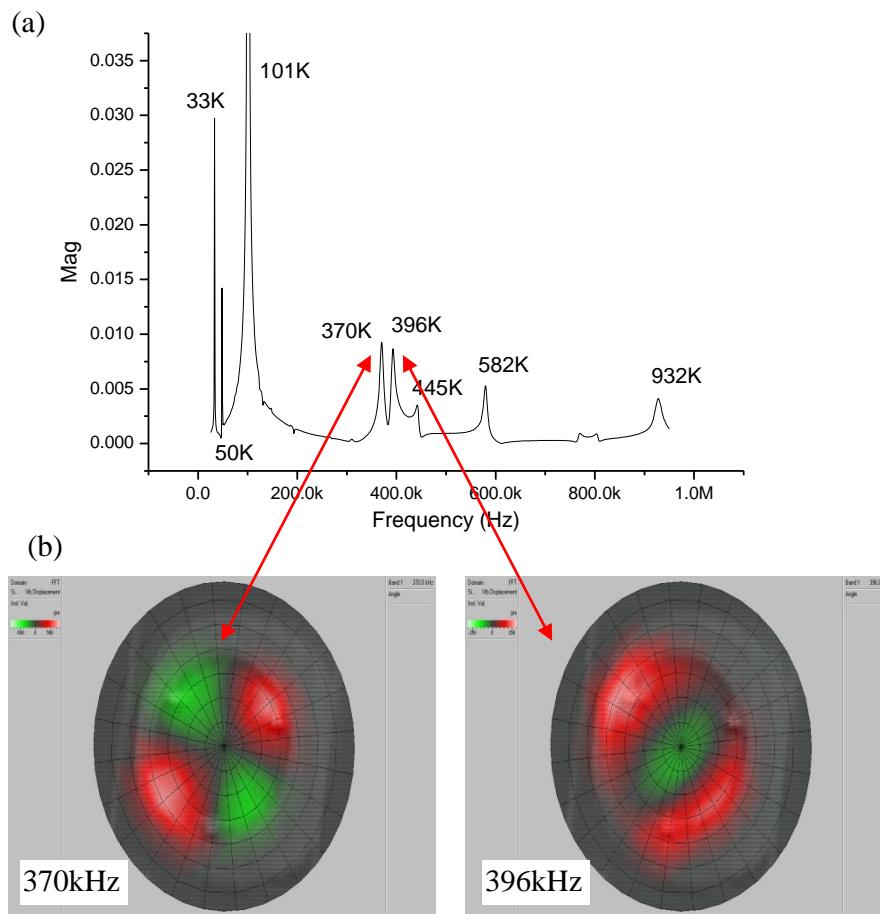
Figure 3.11 a) shows spectrum data where the resonate frequencies are labeled. b) shows mode shape data measured at 370kHz and 390kHz.

There are two types of vibrometer measurements undertaken using PSV, namely; a) Spectrums are taken at one point of the sled and the vibration frequency is swept, and b) Mode shape is measured over many points of the sled at a single fixed vibration frequency. The spectrum data Figure 3.11a is used to determine the sled resonant frequencies over a wide frequency range. By proper setup we are able to measure the frequency peaks up to 1MHz. The mode data Figure 3.11b is used to obtain the modal shape of a sled when the resonant frequency is already known. When a sled is processed by HF vapor etching (see 3.3.2), the minimum diameter of PSV laser spot on the sled is about 20 µm and this defined the best spatial resolution obtained. Good measurement

results (e.g. Figure 3.11b) can only be obtained if the resonant peaks are significantly higher than the noise.

3.3.2 Requirements of the Sled surface for PSV measurement

A strong intensity of light scattered from the sample surface to the PSV scanning head is found essential for measurement. Very thin sleds (~300nm) are optically transparent. Most of the laser light will pass through the sled plate and not scatter enough back to the scanning head. Thicker sleds (~3μm) are not transparent, but the PSV measurements were found dependent on the surface scattering capability. The tip side of the sled (front side) is roughened by the tip formation processes and is suitable for PSV measurement. However, the other surface of the sled (backside) is not, and this is the surface that must be measured when a sled is placed onto a substrate. The scattering capability of the back side surface can be improved by plasma etching which roughens the surface. A better roughening method was found by using HF vapor etching during the release step and useful PSV measurements could thus be obtained for thick sleds (~3μm).

A 10nm gold layer is also deposited on the back side of the thick sleds. The metal slightly enhances the scattered light intensity; however the main purpose is to obtain improved contrast for video camera monitoring. For example, a sled with clean Si surfaces resting on a silicon surface is very difficult to observe under the video camera, whereas a gold coated sled greatly improves the visibility.

Even with HF vapor etching thin sleds still have the problem of poor reflected-scattering to the PSV. We also explored coating a thin layer of Au (about 4-10 nm thick) onto the sled surface to increase the reflectivity. However, the metal deposition increases the stress and we observed that the surface of the plate becomes curved and cracks can form

(see section 4.1.3.3). Unfortunately, a similar metal layer cannot be deposited on the other side to balance the stress because the metal layer will coat the tips. Thus, the yield is low for the thin sleds needed for PSV measurement.

3.3.3 Setup for piezoelectric (PZT) actuation

In general, there were two major tasks to measure the movement of a sled under actuation, namely (a) to measure the vibration resonance modes, and (b) to observe if the sled moves as the frequency and amplitude of the actuation is varied.

The vibration resonance modes (task (a)) were measured using PZT actuation, as shown in Figure 3.12. Two cases are studied, namely with the sled still attached to the process chip (Figure 3.12a) and the sled free standing on a surface (Figure 3.12b). In both cases the sled chip or the substrate are directly attached with adhesive to the PZT plate. A typical PZT plate has dimension of $5 \times 5\text{mm}^2$, thickness 1mm, and material EBL#2 poled in the thickness direction. The camera within the PSV helps to align the PSV laser spot and also to monitor any actuation induced movement of the device on the surface.

Using PZT actuation, the second task (b) is simple. A chosen substrate is mounted (e.g. by glue) onto a piezoelectric plate. A sled is dropped onto the substrate and the sample placed under an optical microscope (similar to Figure 3.12b). Any movement of the sled under varying actuation can be observed and recorded. The results are discussed in Section 6.4.
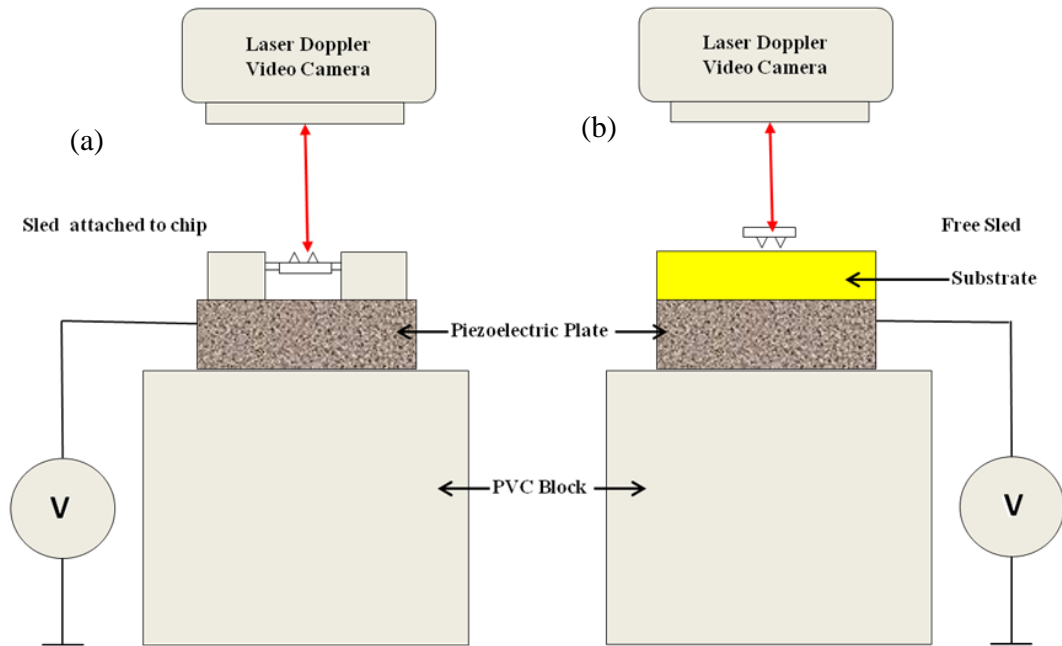
Figure 3.12: PZT actuation in the vibrometer setup. a) Schematic showing the set up for measuring resonant frequencies of a sled which is not yet released from the process chip. b) Schematic showing the setup for actuating a dropped sled on a surface. In both cases, the laser can scan across the surface and measure the mode shapes and the mode frequencies. The piezoelectric is mounted on a large PVC block to increase damping and hence decrease spurious mechanical excitations.

Figure 3.13 shows schematically the implementation of the PSV measurement. The sample is attached onto the PZT plate. The laser is aligned to the sample area of interest and focused. A 45° mirror directs the laser perpendicular onto the sample because the out of plane motion of the sled is required. A function generator (HP 33120A) supplies a variable frequency/variable amplitude voltage to drive the PZT motion. Typically, sinusoidal waveforms are used and if required a high voltage amplifier can increase the PZT drive voltage up to ±100 V. Lock in detection can greatly improve measurements in which the frequency is swept (see Section 3.3.5).

It was found to be challenging to measure the resonant frequencies and the mode shapes of a sled, because i) the sleds are free standing, ii) the sleds are very thin, iii) the

displacement amplitude of the sled is small, and iv) PZT actuation produces much unwanted noise. Increased noise and the excitation of unknown resonances restricted the use of PZT actuation to frequencies less than ~250 kHz. To decrease the vibration noise to acceptable levels, the entire PSV is placed onto a vibration table, and the mirror stand and sample stage are bolted to the table.
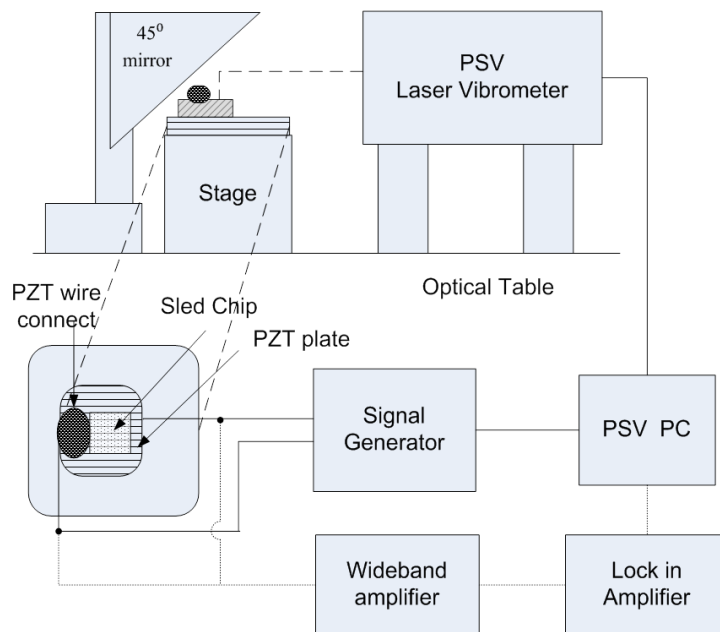
Figure 3.13 Schematic drawing of the method using PZT actuation to measure the sled vibration.

The PZT plates are relatively small and their first resonance is high. Thus noise from the PZT plate vibration is not significant. However, noise generated from the stage that holds the PZT plate is high because the plate directly couples to, and excites the vibration of the stage. Efforts were made to seek a suitable type of material to damp this source of mechanical noise. Ideally, the vibration of the PZT should show no resonances over the frequency range of interest. Vibration tests with a few stage materials are illustrated in Figure 3.14.
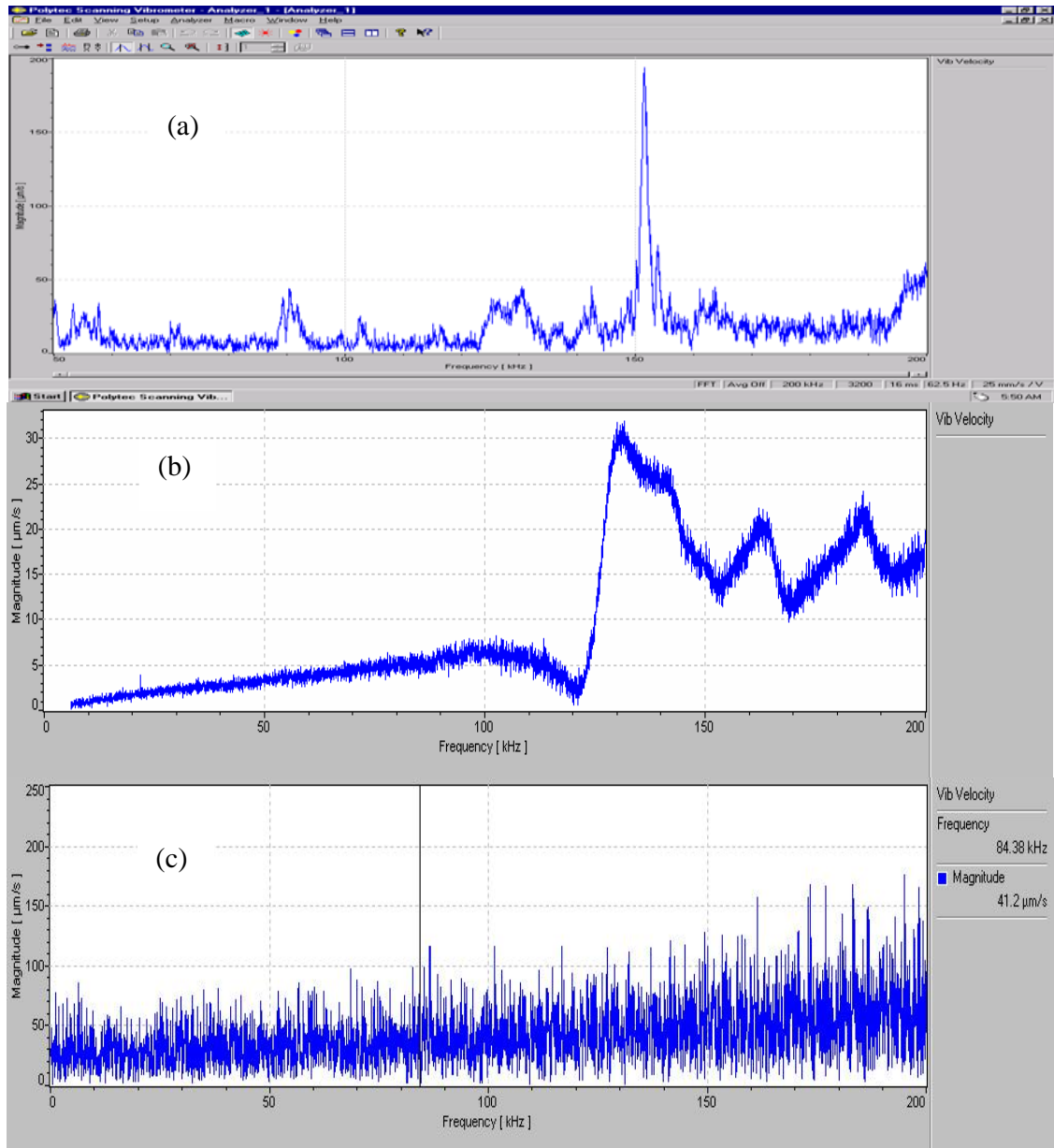
Figure 3.14 Example of raw data PSV measurement results from stages made of different materials. (a) a commercial optical stage, (b) a stage made of rubber/Al block, and (c) a stage made from PVC block. Stage (c) can best damp the mechanical noise.

In the tests, a 10V periodic chirp waveform was used to drive the PZT plate glued directly onto the stage, while the laser was focused on the PZT surface. Frequency spectrums show several strong peaks for a commercial optical stage (Figure 3.14a). An aluminium block was also tested as a stage with a rubber pad to hold the sled chip. However, the results show high noise peaks above 120 kHz (Figure 3.14b). A stage made from a lossy

material (PVC) is found to provide the best damping effects (Figure 3.14c), with the PZT response being liner up to ~250 kHz.

Two types of PZT stages are constructed and are shown in Figure 3.15. Stage (a) is used for small samples which are firmly stuck onto a single 5x5mm PZT plate with super glue. Stage (b) is made of copper tape connecting cross four separate pieces of 5x5mm PZT plate. Whole large pieces of PZT were found to be unsuitable because plate resonances occurred at relatively low frequency. Double sided tape is attached to the top of the copper plate. Large size samples, such as a silicon chip, can be easily stuck on and taken off. However, the double sided tape is not as rigid as the glue method and the four pieces of PZT plate are not identical. Both effects lead to small spurious resonances and in general stage (b) is noisier than stage (a).
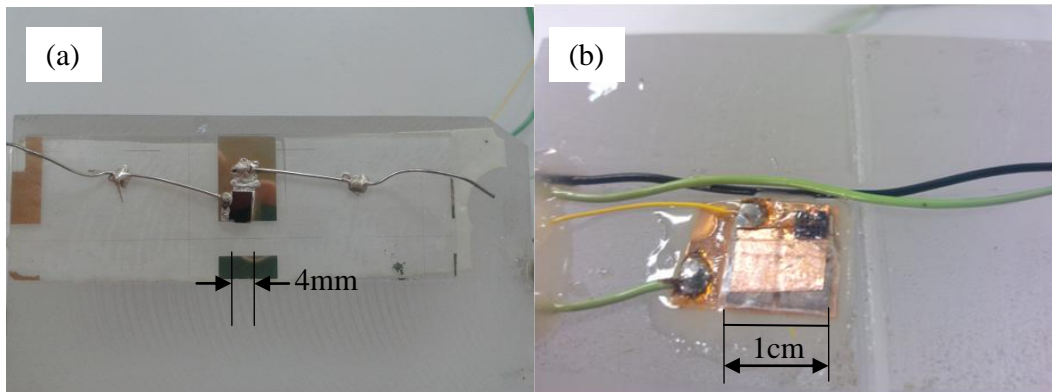
Figure 3.15 Two PZT stages used. (a) The stage used for testing small samples, showing a silicon piece glued directly to the PZT plate. (b) The stage used for larger substrates.

3.3.4 Magnetic actuation

The problems of mechanical noise in PZT actuation can be circumvented if magnetic activation of the sled is used. A magnetic particle is glued to the sled and an external, oscillating magnetic field is generated by a solenoid (Figure 3.16). The magnetic field results in a force exerted on the magnetized particle, actuating the sled motion. Only the sled responds to the magnetic force and thus the method has lower noise than the PZT

approach because no other mechanical resonances are excited. Compared to PZT activation, magnetic actuation provides clean frequency responses up to the PSV instrumentation capability (1MHz). A disadvantage with magnetic actuation is the driving force is weak.
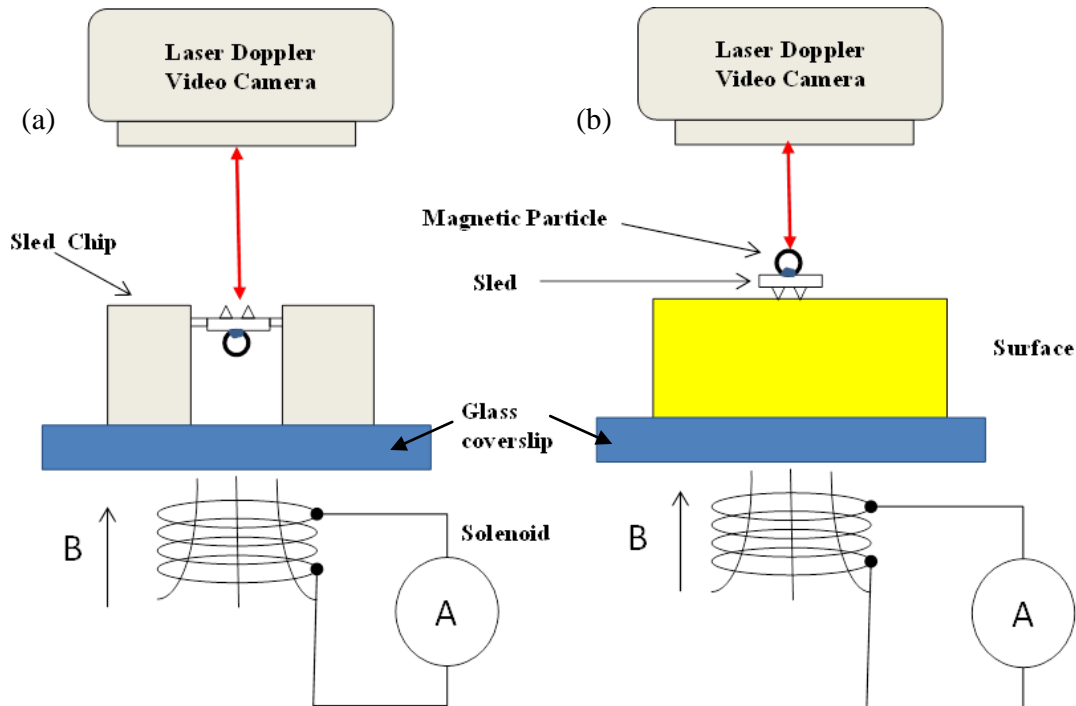
Figure 3.16 a) Schematic showing the laser vibrometer set up for magnetic actuation to measure resonant frequencies of an unreleased sled. b) Schematic showing the setup for magnetic actuating of a sled placed onto a surface. A magnetic particle is glued onto the sled. The magnetic forces on the particle are produced from the field B which is created by the solenoid. Current to the solenoid coil is provided by a function generator (HP 33120A).

The solenoid consists of insulated copper wires wound around a ~3mm diameter ~8mm long ferrite core. The solenoid is pushed into a hole machined into a large Teflon block (Figure 3.17). The solenoid is glued underneath a glass coverslip and two wires of the coil extend out from slots to connect a function generator. Samples can be attached directly onto the glass coverslip. It is found that the spectrum can change depending on the location of the sled above the solenoid. This is not surprising given that the magnetic

field lines diverge from the surface normal direction the further one moves from the center of the solenoid. Both the direction and magnitude of the actuation force at a given location depends on the strength of the local magnetic field (B) and the angle of the particle magnetization (M) with the field. In the simplest case, the force (F) from the magnetic particle is given by,

$$\mathbf{F} = V_n \nabla (\mathbf{M} \cdot \mathbf{B}) \tag{3.3}$$

where V_n is the volume of the particle.

The torque (τ) applied on the magnetic particle is,

$$\tau = V_n \mathbf{M} \times \mathbf{B} \tag{3.4}$$

In general, the actuation displacement generated by the torque (τ) is significantly larger than the force (F).[48]
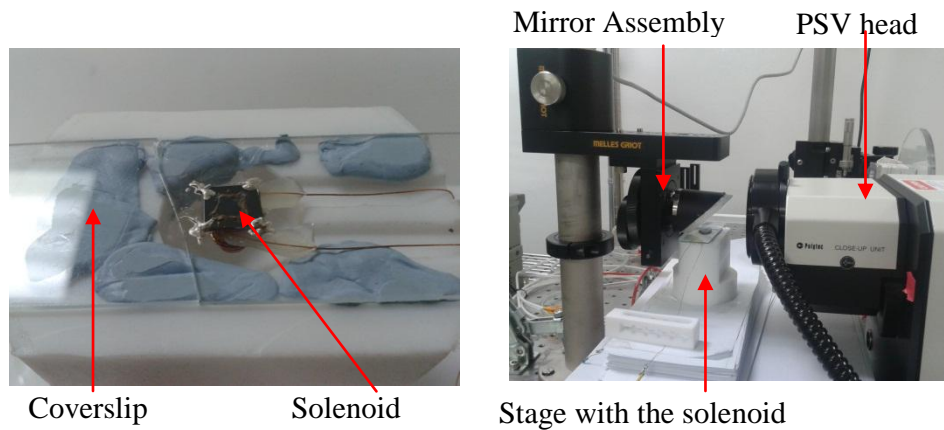
Figure 3.17(a) Teflon stage used for magnetic actuation. (b) The stage is aligned with the mirror assembly and the laser vibrometer.

One drawback of magnetic actuation is that the applied forces are rather small. This is not an issue in the measurement of the sled resonances and mode shapes (Figure 3.16a), but it is a problem for experiments attempting to move the sled across a surface (Figure 3.16b). The maximum AC current that can be driven through the 0.79 Ω solenoid is

$355mA_{pp}$, and generates an oscillating field of 8mT measured at 50Hz using a Hall probe. The field falls to around half this value at 500 kHz because of the coil inductance. A particle of diameter 60μm has a volume of $V_n = 1.13 \times 10^5 μm^3$. Hence from Equations 3.5 and 3.6, the maximum toque that can be generated for a ferrite particle is ~ 1nN·m.

3.3.5 Lock-in detection with PSV

The PSV vibrometer uses fast flourier transform (FFT) to obtain the frequency spectrum response, typically using a chirp waveform to drive the actuation. For very small displacements of structures of narrow (high Q) resonance, the FFT approach does not work well as noise and poor spectral resolution mask the signal. We therefore use a lock-in amplifier (Figure 3.13), giving high noise rejection[63] and flexibility in acquisition parameters.

The input of the lock-in amplifier is connected to the PSV velocity output. The oscillator voltage from the lock-in used to drive either the PZT or the magnetic solenoid. The maximum lock-in voltage output is about $2V_{pk-pk}$, and to increase the activation displacement the output is amplified up to $20V_{pk-pk}$ using a variable gain WA301 wideband amplifier.

Table 3.1 Typical Settings Used for Spectrum Acquisition Using Lockin Amplifiers Connected to the PSV

	EG&G Model 7265	SR844 RF
Frequency Measurement Range	0-250kHz	25-950KHz
Oscillator output	Sinusoidal	Square
Sensitivity	3mV/10mV	10mV
Frequency Step	0.1or 0.2kHz	0.5, 1 or 2kHz
Time Constant	0.2ms	1s

Two types of lock-in amplifiers, EG&G Model 7265 for low frequency and SR844 RF for high frequency, are used. Typical settings are shown in Table 3.1. Both lock-in

amplifiers are connected to a PC for data acquisition and analysis of the amplitude and phase of the PSV signal.

3.3.6 Vacuum chamber for PSV measurement

The mechanical motion of MEMS structures can be significantly damped by air or gas surrounding the structure. Viscous damping broadens the vibration resonance peaks and decreases their amplitude for a given actuation force. Both of these effects are undesirable, the former because it becomes more difficult to analyze broader peaks in a PSV spectrum, and the later because for actuation we require access to the highest possible displacement to move the sled.

In order to remove viscous damping a vacuum chamber enclosing the MEMS device was constructed (Figure 3.18). A vacuum environment not only removes viscous damping but also minimize contamination of the sample surfaces. In particular, adsorbed water can lead to meniscus formation under ambient conditions. The resulting capillary forces can be very strong, leading to the well-known stiction which often occurs in MEMS devices. Note that water meniscus formation can also be avoided by using a hydrophobic surface, as discussed in Section 3.4.

An experimental problem is to determine the focus on the sled when the sled is in vacuum. Laser light scatters at the glass window resulting in additional spots, as shown in Figure 3.18d, making it difficult to determine the exact laser location. Also, the modal shapes can be distorted by the laser scattering. Consequently, vacuum conditions can be used to measure the frequency spectra of a sled, but not for modal shape measurement.
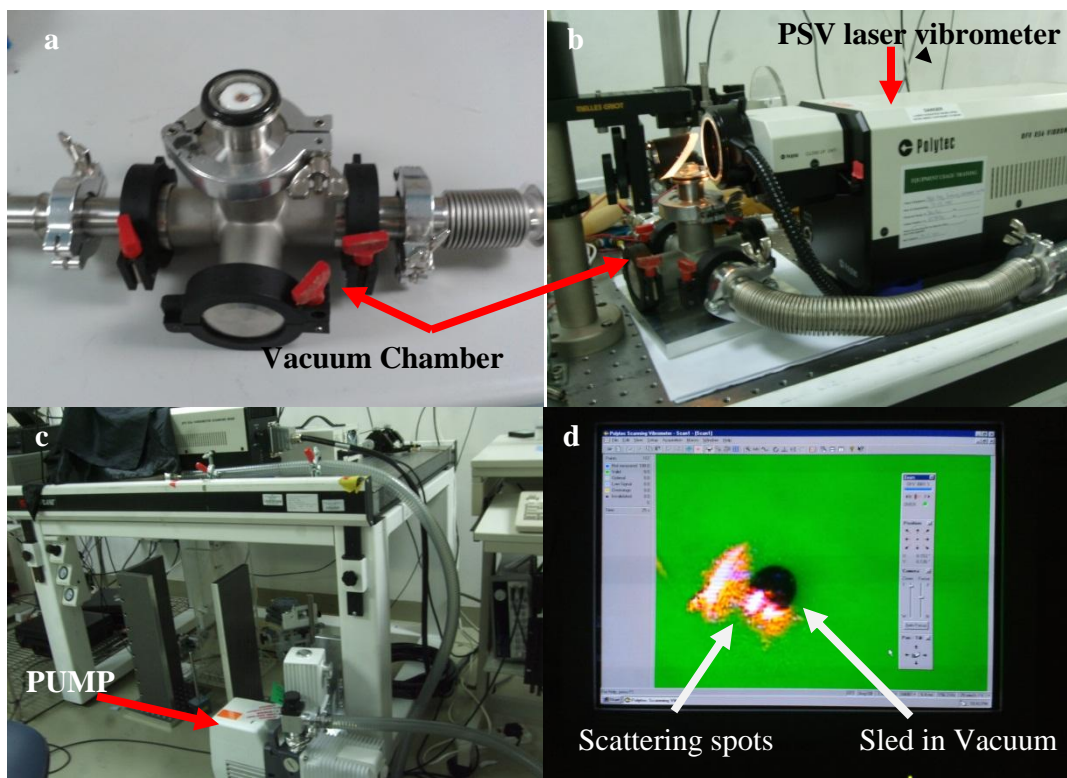
Figure 3.18 a) The vacuum chamber with a magnetic stage sitting just below a glass window. The window rest on a Viton O–ring for vacuum sealing and can be easily removed for sample transfer b) the vacuum chamber aligned for PSV measurement, c) the pump rests on the floor and connects to the vacuum chamber by plastic and flexible hose tubing, and d) In vacuum, scattering spots are observed. Only one spot is focused on the sled surface; the other two spots are reflected from the glass window interfaces.

3.4 Surfaces used

Three substrates are used, namely freshly cleaved mica and graphite, and silicon coated with perfluorocdecyltrichlorosilane (FDTS) to produce a fluorine terminated monolayer on silicon (F-Si). F-Si is used as a lubricating substrate and can effectively minimize water absorption and significantly reduce stiction and adhesion.[64,65]

In our work, FDTS is coated on very smooth silicon chips, produced from the prime silicon wafers for silicon fusion bonding (Ultrasil Corporation, resistivity 1-30 ohm-cm, TTV < 2μm, particle number < 10 at 0.2μm). The silicon chips are first dipped in a fresh

diluted HF (1:100) for 15 sec to remove the native oxide. The chips are then rinsed by DI wafer, transferred inside IPA, and ultrasonic cleaned with IPA. The samples are then rinsed by DI water and blow dried. A 3 min oxygen plasma cleaning is then conducted (Trion Sirus) to remove surface organics. Within 10min, the chips are loaded inside a SAM coater (AVC-150M, Sorona) for FDTS coating. The coating temperature is 120°C.

AFM images over a 10μm square area show that the FDTS coating only slightly increases the surface roughness from 0.97 to 1.09 nm rms, although occasional large particles (~20nm) can also be observed.

A sled is difficult to clearly observe when placed on F-Si and a thin layer of gold (4-10nm) is required to enhance the visibility. In contrast, mica is transparent and a sled on the surface can be clearly observed. It is also generally found that both thin and thick sleds are easier to place on mica compared to F-Si. One problem with mica is that the surface readily absorbs water and leads to meniscus formation around the sled tips under ambient conditions. The resulting capillary forces can be very strong and lead to stiction. Thus, actuating tests were typically conducted for a sled on mica within half a day. The sled was typically gently pushed with a wire before actuating tests. The graphitic substrate is only limitedly explored as on actuation the sled appears to stop almost immediately, presumably because the sled tips encounter and stop at step edges.

3.5 Summary

This chapter discusses the experimental procedures and processes that are related to the sled fabrication, characterization and actuation. Several Specialized fabrication processes were developed (submicron etching, HF vapor release, tip sharpening, magnetic particle

actuation). A home built AFM was constructed for the new method of measuring friction on free standing structures, and some details of the construction are described. The plate resonances were recorded using a commercial laser vibrometer. However, our experimental requirements are more stringent than typical dynamic MEMS measurements, usually limited to bulk micromachined membranes or cantilevers. Very small displacements are encountered (<1 nm) in our experiments and the sleds can have important resonance modes up to ~900 kHz. Considerable effort was therefore made to reduce the vibrometer noise levels. We built special piezoelectric actuation stages, magnetic actuation stages, and a vacuum chamber to integrate with the vibrometer.

Chapter 4 Fabrication of Sleds

The fabricated sled structure is shown in Figure 4.1. Circular, triangular and square sleds are fabricated, all with three sharp tips, and of edge dimension of 100, 200 or 300μm.

Very thin sleds are preferred since the plate resonance frequencies desired for actuation can be low (less than 500 kHz), making measurement and actuation easier to perform. Processes for making 300nm thin sleds are described in section 4.1. However, the handling of very thin sleds is difficult and the most useful measurements were undertaken on 3-6μm thick sleds. The process flows to fabricate the thicker sleds is described in section 4.2.

Delicate spring legs are used to hang the sleds. The legs can be broken to drop the sled onto a new substrate, with the 3 tips touching the substrate surface. The legs are composed of a wide portion at the base, a centre beam and a short neck near the sled. The large wide portion of the base is to anchor the sled onto the substrate and solve alignment shift during fabrication.   Since the spring constant is mainly determined by the centre beam, an extended etch does not change the spring leg performance.

The tips should be as sharp as possible and located at anti-node positions of a plate resonance mode to achieve the largest amplitude under activation. The mode shapes and frequency are studied using finite element modelling in section 4.3. While the modelling results are clear for hanging structures as in Figure 4.1, it turns out that the addition of a magnetic particle or the touching of the 3 tips on a surface complicates the problem considerably (see also Chapter 6 experiment data). Thus, for practical application, the tip locations chosen in the present designs are probably not optimal and further work is needed on this issue.
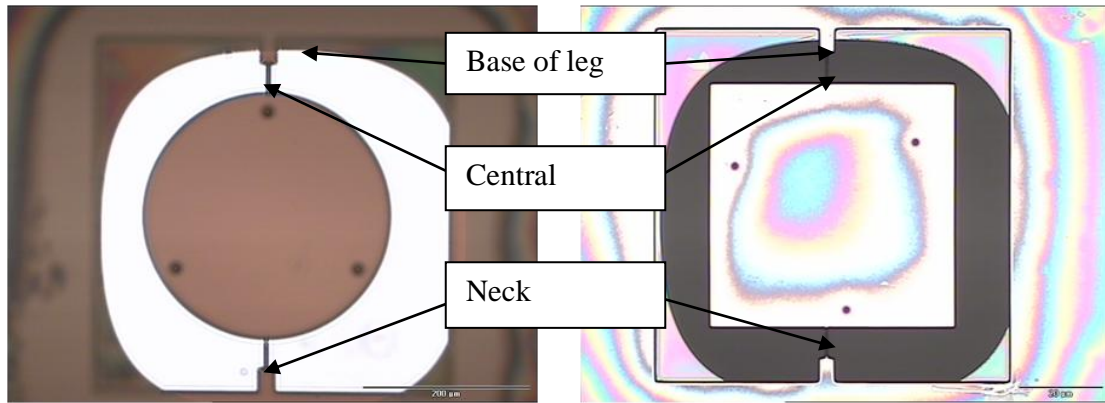
Figure 4.1 Designs of legs are shown on a circular and a square sled. The alignment error can be seen between the device and the release hole, and the leg design must accommodate for this error.

4.1 Thin sleds

We have fabricated extremely thin sleds down to only 300nm thick. Using very thin sleds is desirable to (1) decrease the resonance frequency of the free sled, allowing superlubricity actuation to occur in an experimentally more accessible frequency range of <500kHz , and (2) ensure the inertia (i.e. the mass) is very small, thus giving a very low load when in contact with a surface. The sled must integrate sharp nitride tips for realizing three point contact and have a uniform thickness.

However, the vibrometer testing of the ultrathin sleds proved challenging because there is little scattered light. A full or partial metal reflection coating is required but the stress must be kept low to prevent curling of the ultrathin silicon plate. Handling the sled is also difficult because the sleds are very fragile. Due to these difficulties, the vibrometer testing results obtained on the ultrathin sleds were limited and most data is taken on thicker (~3µm) sleds.

4.1.1 Thin sled fabrication flow
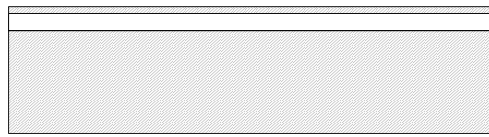
(a)
Start of SOI wafer with 340nm thick silicon device layer
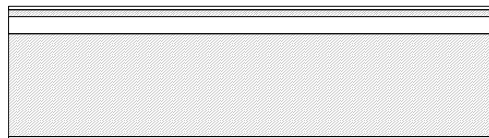
(b)
Thermal oxidation and device silicon layer is ~ 300 nm thick
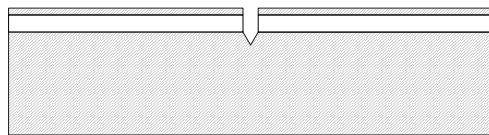
(c)
Pattern and etch holes through the interlayer oxide and then use KOH etch to form sharp cavities on substrate layer
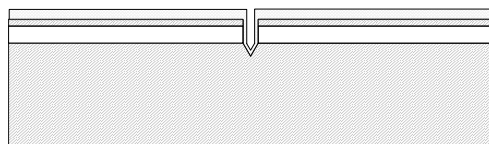
(d)
Deposition of 400nm LPCVD nitride
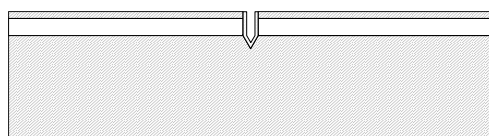
(e)
Pattern and etch away the nitride thin film outside the cavity. Remove thermal oxide layer

Figure 4.2 Fabrication sequence for ultrathin sleds

(Continued)
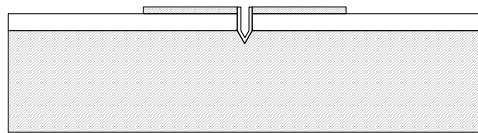
(f)
Pattern and etch silicon to form sled structure
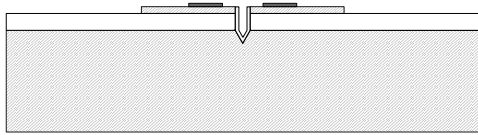
(g)
Pattern and E-beam evaporation
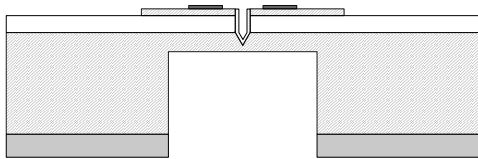
(h)
Pattern the release hole on SOI backside, and DRIE etch silicon
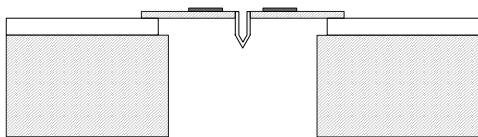
(i)
XeF$_2$ silicon etching until buffer oxide layer. HF vapor is used to release the sled device.

| Silicon | Silicon oxide | Photo-resist | Nitride | Metal |
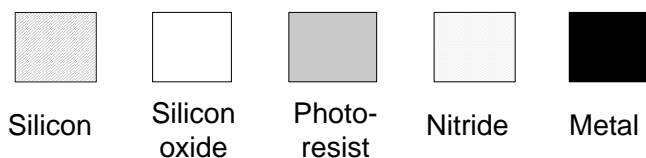
The fabrication process starts on a 4 inch SOI wafer (SOI Tech) with an ultra-thin silicon device layer. The silicon device layer is 340nm thick, the interlayer oxide is about 1 μm thick and the substrate silicon is about 500 μm thick (Figure 4.2a).

A 90 nm thick thermal oxide is grown onto the SOI surfaces by dry oxidation at 1000°C using pure oxygen only (Figure 4.2b). The dry oxide layer is used as a good mask to protect the ultra-thin device layer in subsequent etching steps, specifically to withstand

KOH wet etching (Figure 4.2c) and to withstand the dry etching of the LPCVD nitride film (Figure 4.2e).

The sequence of forming nitride tips into the SOI substrate layer is shown in Figure 4.2c-e. The lithography defines the tip regions in 4 x 4µm square shapes on the silicon device layer using 3 µm thick photoresist. Reactive ion etching (Oxford 80) follows to etch 3 layers of materials inside the patterns with the photoresist as the mask, i.e., the 90 nm thick thermal dioxide, 340 nm thick silicon device layer and the 1 µm thick buffer oxide layer. The etching is stopped once the underneath substrate silicon is exposed. The photoresist is then stripped off and the wafers are put into KOH (30% wt KOH, 65°C). With the dry oxide as the mask, sharp silicon cavities are fabricated after 15 min silicon etching (see Figure 4.2c). The dry oxide is measured to be about 70nm after KOH etching.

After a thorough cleaning with hot Piranha and RCA clean, LPCVD nitride deposition is carried out (LPCVD nitride tube, Centratherm). To ensure the nitride tips are sharp, immediately before being loaded into the nitride furnace tube, the wafers are dipped into diluted hydrofluoric acid (HF 100:1) for a short period to remove the native oxide. The stoichiometric nitride deposition is then conducted with combined gas flows of dichlorosilane (DCS) and NH_3 (250mTorr, 775°C). Alternatively, low stress (LS) nitride can also be deposited in a separate run under different process conditions (150mTorr, 800°C). Both nitride deposition thicknesses are controlled at about 400nm. (Figure 4.2d).

The nitride layer is only kept in the cavities and a second step of lithography and dry etching removes the unwanted nitride. In this step, the mask in Figure 4.2c is reused. However the photoresist tone is reversed by a image reversal technique (HMDS oven,

Yes Engineering). A plasma etching follows (Plasma etcher, Trion Sirus) and all the exposed nitride film is etched away, except for the regions inside the cavities protected by the photoresist. The etching is stopped when the nitride is completely removed and the dry oxide layer is exposed. After nitride etching, about 50nm oxide layer remains and is removed by buffered oxide wet etching (Figure 4.2e).

A third step of lithography and dry etching is conducted to pattern the thin sled plate structure and legs. Using the submicron silicon etching recipe (Section 3.1.1.3), the sled plate and legs are fabricated (Figure 4.2f).

A forth step of lithography followed by Cr/Au evaporation is conducted to form gold marks for backside alignment (Figure 4.2g). An optimized process is attempted to solve cracks caused by metal stress, as discussed in Section 4.1.3.3.

The formation sequence of the backside release hole is illustrated in Figure 4.2 h-i. A 24 μm thick photoresist (AZ9260) is prepared on the backside surfaces of the wafers, and lithography using backside alignment is conducted to pattern the release hole on the SOI backside. Using the thick photoresist as the mask, deep reactive ion etching (DRIE) is used to deep etch the release holes from the SOI backside (Oxford 100). Since DRIE also attacks the nitride films, the silicon etching is stopped when ~10μm thick silicon is left of the buffer oxide layer (Figure 4.2h). The etching depth is controlled by the total number of DRIE loops based on the depth measurement from the initial 50 etch loops. The etch rate is 0.8μm per etch loop.

Finally, XeF_2 vapor etching is used to etch the silicon residue inside the release hole (XeF_2 vapor etcher, Xactix). XeF_2 is used to etch the silicon because XeF_2 vapor is

reported not to attack nitride,[66] and thus a sharp tip is maintained. The sled release process follows and the SOI oxide is etched away using HF vapor etching (section 3.1.2.2). The final structure is shown in Figure 4.2i. For an optimized process, the release is conducted by heating a thin sled chip at 32°C in a 49% HF and DI water mixture at 1:1 ratio. It takes about 90 min to release a sled chip, and the best yield is about 60%.

4.1.2 Fabrication Results for thin sleds
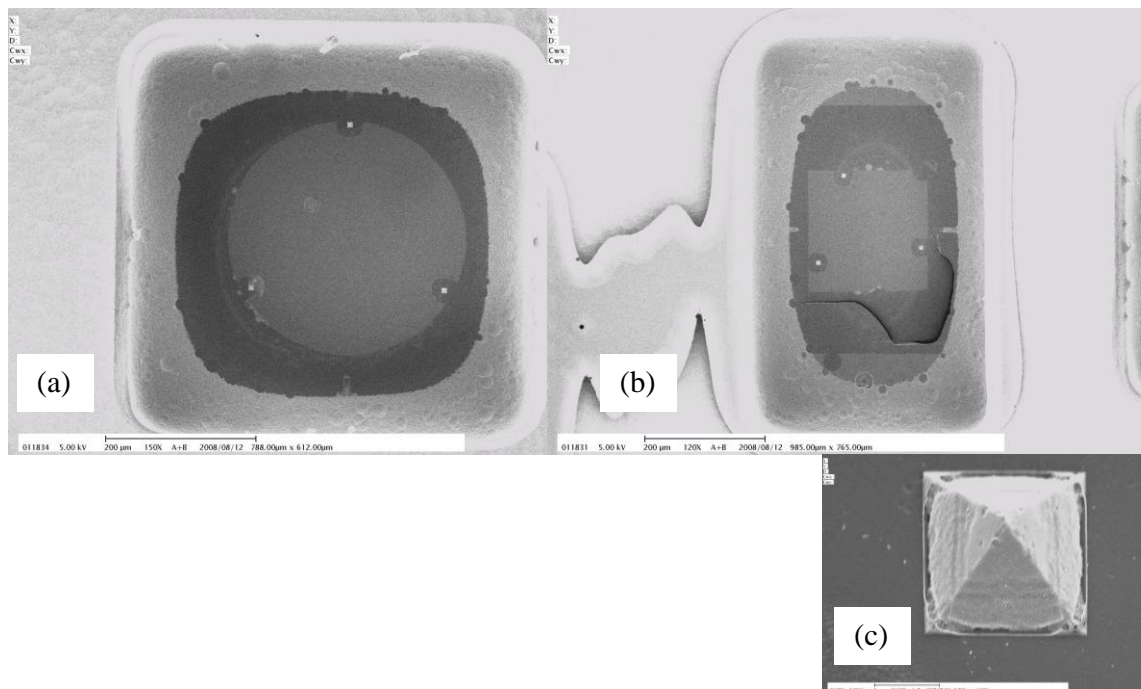
Figure 4.3. SEM of microfabricated thin sleds with plate thickness 300 nm: a) a circular sled and b) a square sled, c) close-up SEM of a nitride tip.

Figure 4.3 shows typical fabricated ultrathin sleds of circular and square shapes. The tip dimensions (Figure 4.3c) are ~5 µm x 5 µm square base with an angle slope defined by the KOH etching. The sled thickness is uniformly controlled at ~ 300 nm.

4.1.3 Fabrication challenges for thin sleds

4.1.3.1 Thin film residue in HF vapor etching

During HF vapor etching, a layer of residue membrane was observed on the area of exposed SOI oxide layer. The membrane has a very slow etch rate and could take an additional ~60 min to disconnect from the sled. We suspect the membrane is related to the manufacturing dopant used for the very thin SOI wafer made by Smart Cut™.[67]
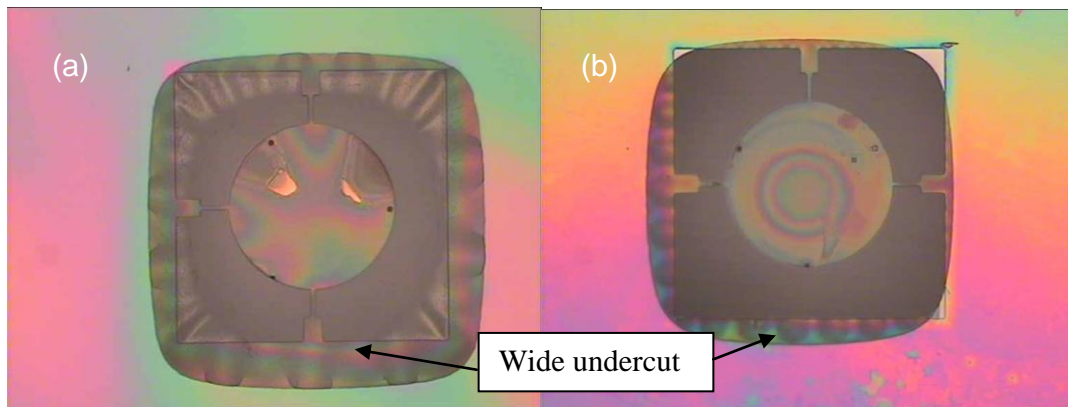
Figure 4.4 optical images showing a) a sled device with wide undercut in all in-plane directions. This device was etched for 80min at 33°C in HF vapor. A thin residue membrane can also been seen. b) A better release result is achieved with less undercut by controlling the formation of the release hole.

Figure 4.4a shows a circular sled after 90min HF vapor etch with the thin film residue at the corners. The sled is not entirely released but further etch of the device is risky because all the sled devices in the whole chip can suddenly break off from capillary forces. Wide lateral undercuts are observed around the release hole (more than ~ 30μm in Figure 4.4a). The HF vapor etches the interfacial oxide faster than the exposed sacrificial oxide. To overcome this problem, the backside release hole is not at first fully opened by a controlled XeF_2 etching, resulting in less undercut and improved yield in the subsequent HF etch (Figure 4.4b).

4.1.3.2 Nitride tips

Both stoichiometric silicon nitride and low stress (LS) nitride are used as the tip materials. LS-nitride was initially proposed to maintain the tip sharpness since XeF_2 vapour is reported not to attack the LS nitride film.[67,68] However, more particles are produced during LS nitride film deposition.[69] Further, LS nitride can be removed in diluted HF. We also found HF vapour etching can damage the LS nitride tip, probably as the vapour etches the particles embedded inside the film and diffuses to etch oxide film underneath. Figure 4.5 shows HF vapor exposure has completely etched the underlying oxide film to release the entire tip region. Also note the erosion of the tip surface. Because of these problems, stoichiometric Si_3N_4 is used for tips.
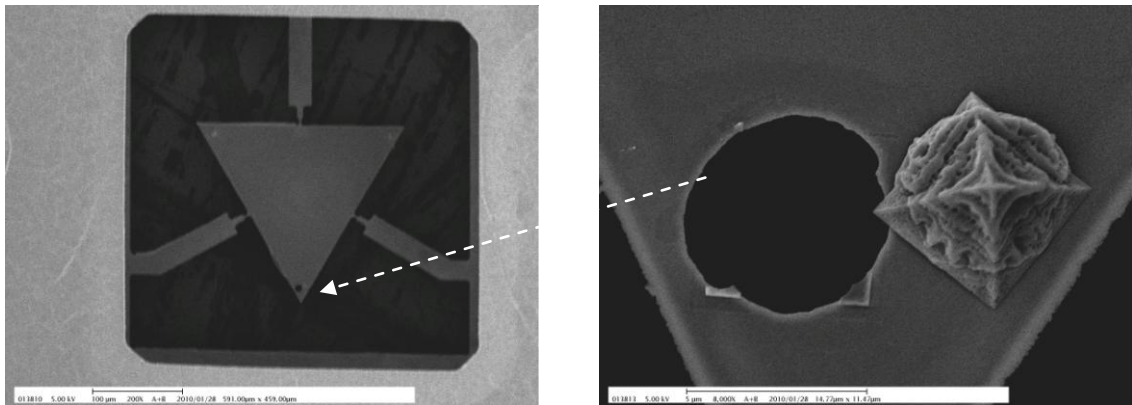
Figure 4.5 SEM micrographs showing a) a triangle sled with LS-nitride tips after 100 min HF vapor etching, and b) the removal of one of the tips.

4.1.3.3 Stress caused by metal film used for optical testing

Metal deposition on very thin sleds is challenging. Figure 4.6a, b show the sleds after thermal evaporation of ~5nm gold. The sleds are either broken at the legs or cracks appear at the surface. The sleds with cracks can break along the crack lines.
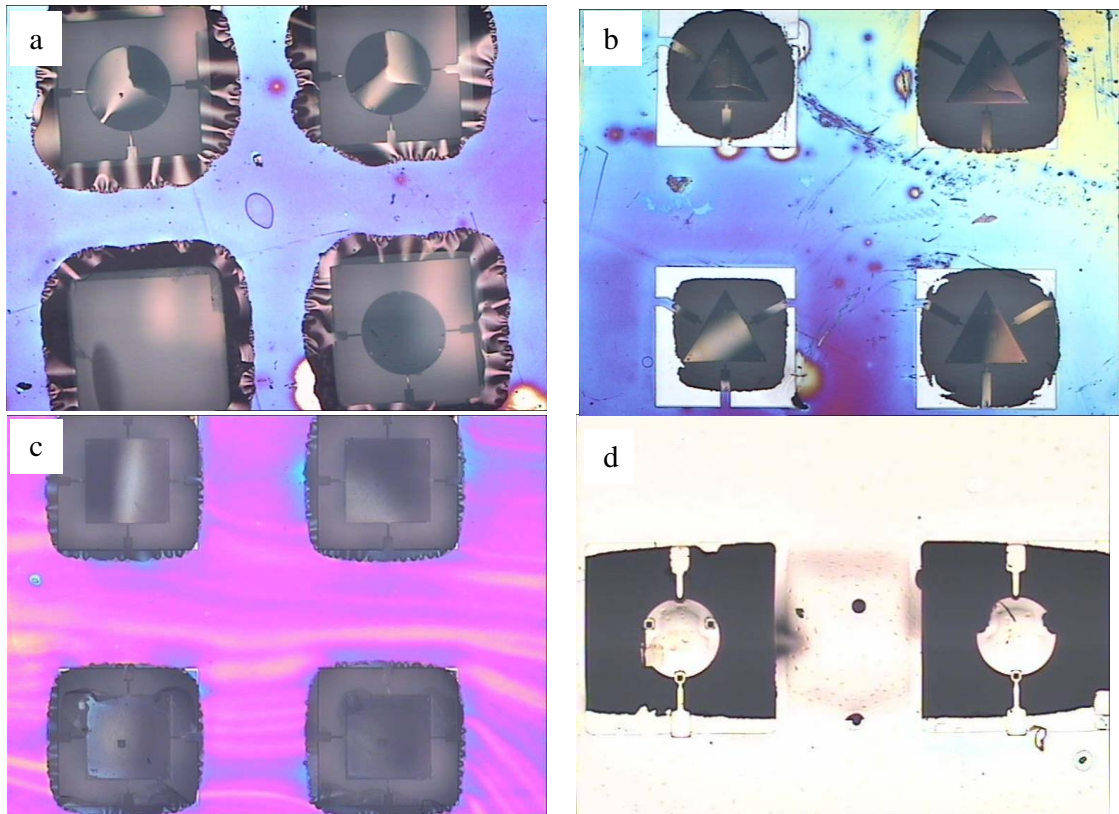
Figure 4.6 Optical micrographs showing the effect of metal deposition on thin sleds. In (a) and (b), cracks are shown on the sleds after 5nm metal deposition. An improvement was made by using quick metal wet etch before the HF vapor etch. Some results are shown in (c) and (d).

To minimize the stress, chrome/gold metal deposition is done (Figure 4.2g), and a quick gold metal wet etching inserted between the XeF_2 etching and HF vapor etch (Figure 4.2i). With SiO_2 membrane still holding the sled, the devices can still withstand the wet etching by careful chip handling. In the wet etching, the MEMS chip was immersed in gold etchant for 10 sec, replaced with DI water and IPA, and then moved out of IPA and air dried. The quick etch removes most of the gold thin film but some gold residues remain on the chrome layer. The HF vapor release is then conducted and Figure 4.6c, d shows some results. There is no cracking but some of the sleds still shown buckling, presumably from the ~1nm Cr layer.

4.1.3.4 Thin sled Removal

For friction tests, the ultrathin sleds need to be cut and placed onto another substrate i.e. the spring legs must be broken. Simply pushing using a metal wire to break the legs does not work because the metal wire can easily damage the ultrathin silicon plate.

Dicing using laser cutting (µVia driller ESI 5200) was unsuccessful. Even with the minimum laser energy settings (laser power 0.08W, velocity 10mm/s), the laser power can ablate the thin sleds.

Mechanical cutting using a Nanoindentor with a sharp diamond tip was tried. In the operation, the diamond tip is aligned onto the leg and the tip is pushed downward as a point load. However, in this method it proved difficult to break 4 separate legs to release a sled.
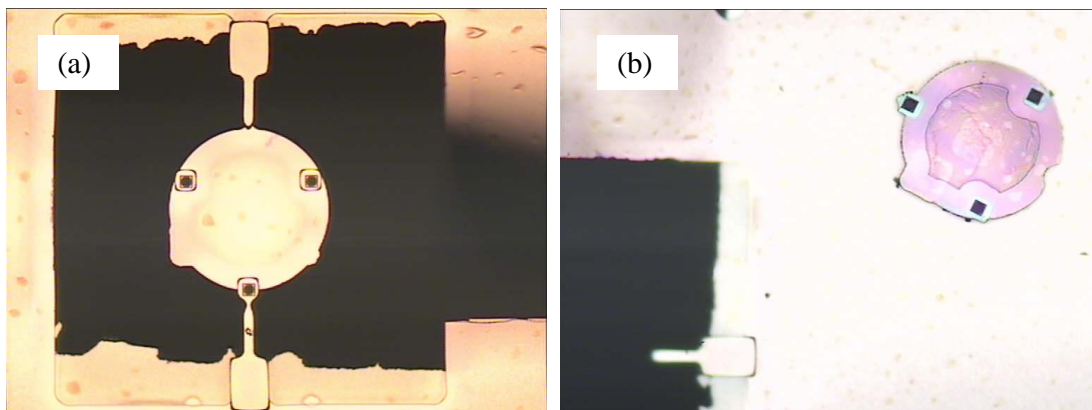
Figure 4.7 a) An ultra-thin sled attached to the process chip, and b) after FIB cutting the sled drops onto the substrate.

Focus ion beam (FIB) is the best approach to cut the thin sled legs. We used a dual beam FIB i.e. a SEM monitors the sled cutting area while a focused gallium beam physically cuts the legs. The sled shown in Figure 4.7a was cut by FIB and after taking the sample out of the FIB vacuum chamber, the removed sled is found nearby on the substrate surface(Figure 4.7b).

4.2 Thick Sled

Thick sleds were made to overhang a free space etched through the entire wafer and connected to the chip substrate by 2 legs. The sleds can be handled easily, and a magnetic particle can be glued on the backside to enable magnetic actuating.

In the thick sled approach, the tips are fabricated in silicon by dry etching, and the sled plate is simultaneously etched with the tip process. The sled plate thickness will vary slightly due to dry etching, and the variation will change the plate resonate frequencies. However, measurement of the mode resonance frequencies can be used to determine the plate thickness if required (section 4.3.1).

Figure 4.8 shows the process flow for thick sled manufacture. The silicon device layer of the SOI wafer is 10 μm thick, the buffer oxide layer is about 1 μm thick, and the substrate layer is about 500 μm thick. The SOI wafers are purchased from UltraTech, USA and are double-side polished. The fabrication starts with a thermal oxidation step (Figure 4.8a). After a RCA clean, a 500 nm thick thermal oxide layer is grown on the SOI surfaces at 1000°C with O_2 and H_2 (Centratherm).

The first lithography step is to form the sled structure on the SOI device layer. A 1.4μm thick photoresist is used as the mask (Suss MA8) and the 500nm thermal oxide is then dry etched (Oxford Plasmalab 80). A second dry etching step follows and around 5μm thick silicon is etched by DRIE (Oxford Plasmalab 100) using the photoresist and oxide as a combined mask. The final structure is shown in Figure 4.8b.

4.2.1 Thick sled fabrication flow
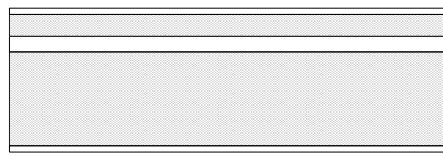
(a)
 SOI wafers with LPCVD oxide grown
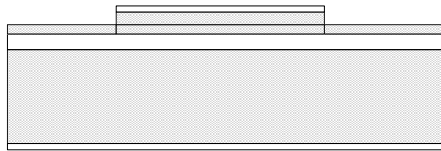
(b)
Formation of sled structure via lithography and DRIE
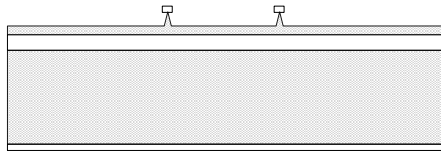
(c)
 Formation of Si tips via Lithography and DRIE etching
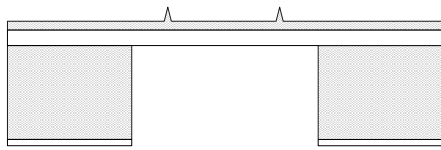
(d)
 Formation of backside hole and tips via lithography and DRIE/RIE, Followed by XeF$_2$ etch
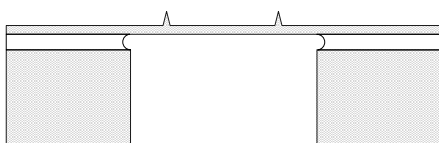
(e)
 Wet etching to release the structure
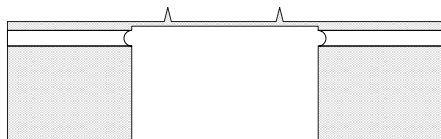
(f) Post process (Optional)
 Metal Evaporation or
 Sled thinning from backside

Silicon   Silicon oxide

Figure 4.8 Fabrication sequence for thick sleds

The second patterning step is to align and form the tip features. A 5.5µm thick photoresist is used to planarize the wafer topology and there follows alignment, photoresist exposure and development (MA6, Suss). RIE etching is then used to remove thermal oxide with photoresist mask. A short period of silicon DRIE etching follows to etch silicon for an additional 5µm using photoresist and oxide as a combined mask. The final structure is shown in Figure 4.8c.

The last patterning step is to etch the backside release hole on the SOI substrate layer. Lithography with backside alignment is conducted using 24µm thick AZ9260 photoresist followed by RIE oxide etching. With oxide and photoresist as a combined mask, a silicon DRIE process is conducted to etch through the substrate layer and the etching progress is stopped when the etching almost reaches the interlayer oxide, when a small dot of light on every sled center can be observed under a microscope when light is shining from the backside release hole.

The wafer is broken into chip sizes. The tips are sharpened by an isotropic etching of the silicon by RIE (Plamalab80). XeF_2 vapor etching (Xactix) is then used to remove the silicon residue underneath the sled structure and the legs (Figure 4.8d).

The release step is conducted by HF vapor etching (Section 3.1.2.2.) Since the thick sled is robust, a fast vapor etching can be used. The HF vapor etching is conducted by heating the chip at 28°C with 49% hydrofluoric acid (HF) for about 5min to completely release a sled (Figure 4.8e). The yield is about 90%.

Some optional post-processes are as follows (Figure 4.8f). A thin gold layer can be evaporated (Edwards 360) onto the sled backside to enhance the visibility for sled tests on

silicon surfaces. The sled can also be thinned from the backside by RIE etching (Oxford Plasmalab 80). The thickness can be made less than 1 micron so that the mode resonate frequencies can be low, with the surface also roughened and hence removing the need for metal evaporation. However, the spring legs become delicate. This approach could be optimized in future and also provide an easier method for ultrathin sled fabrication.
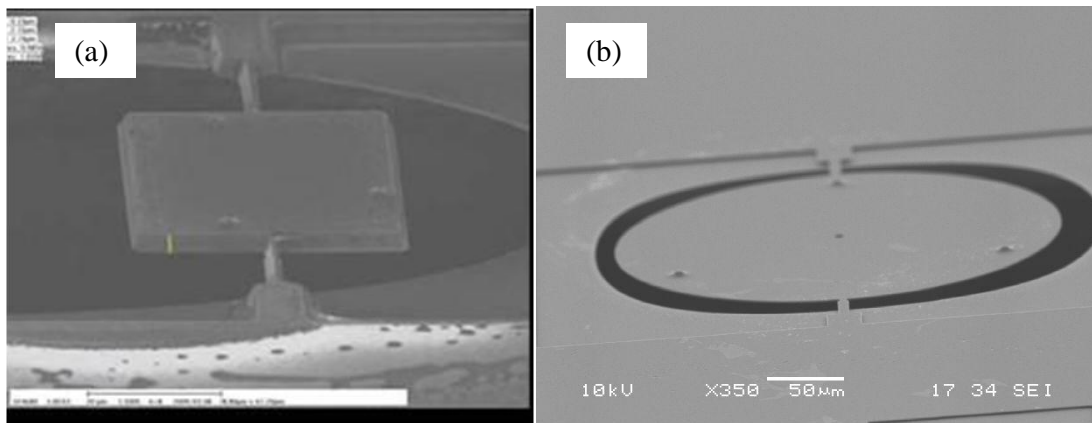
Figure 4.9 Released thick sleds the fabrication. a) A square sled and b) a circular sled, each with 3 tips

Figure 4.9 shows fabrication results of a square and circular thick sled. The design allows the sled to be placed onto any free surface by i) moving the substrate chip to the desired surface, and ii) pushing out the sled by breaking the legs (e.g. by using a ~50μm diameter, stiff metal wire) such that the sled falls on the surface underneath.

4.2.2 Fabrication challenges for thick sleds
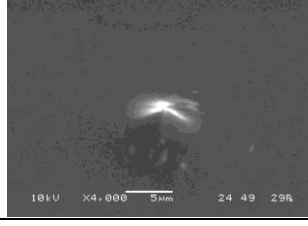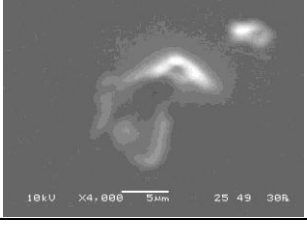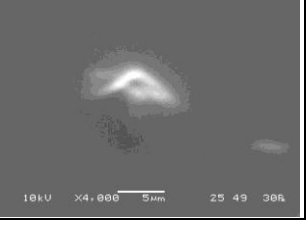
4.2.2.1 Tip sharpening

The tip sharpening is by silicon plasma etching (Figure 4.8d) and similar techniques are used to fabricate sharp AFM tips.[70-72] Protected by the oxide mask on the top, the tip sidewall is isotropically etched away in a SF_6 plasma (Oxford Plasmalab 80). Although the pressure of the basic silicon etching recipe is 175mT, a high pressure of 300mT is found best for sharpening.

The etching progress is difficult to monitor optically since the tip apex is very small, even under the highest magnification. The sled tips are thus inspected by SEM after etching, although this is also difficult because of oxide charging. Thin gold can be deposited selectively over the tips to minimize the charging, but the sled must be discarded if the etching is not completed.

With experience, SEM inspection is not required after an etching recipe is established. Table 4.1 summarizes the typical tips made. The profile of type I tips is good and shows the tip sharpening process works. If the tips are over etched, then the profiles of type II are produced. These two types are commonly observed with all three tips of the same sled being similar. Three tips of a sled might not always be similar, as illustrated in tip type III. In this example, the chips are located on the outside region of a 4 inch wafer with non-uniform plasma intensity; such tips can be very blunt.

Table 4.1 Sled Tip Types after Sharpening Process

	Tip 1	Tip 2	Tip3
type I (common)			
type II (common)			
type III (near the wafer edge)			

4.2.2.2 Removing a sled with an attached magnetic particle

A gold or copper wire can be used to gently push the sled backside and break the spring leg, and the sled drops onto the underlaying surface. Even if the sled falls with the tips facing upward, the metal wire can be used to flip the sled such that the tips contact the surface.

However, it is challenging to remove a sled with an attached magnetic particle because the wire can firmly adhere to the magnetic particle. For the same reason, it is awkward to flip a sled with magnetic particle by using a wire.

A laser dicing method can be used to overcome the problem. The sled chip is first aligned on a desired surface with the tips facing the surface. A suitable gap of ~100-150μm is needed between the sled chip and the substrate so that the chip will drop without flipping. A smaller spacing can give problems since the sled can re-attach to the chip, probably due to the electrical charges generated by the laser cutting. The laser (ESI 5200) is focused on the legs. A minimum laser power of 0.08W and fast laser velocity (10mm/s) are used to give a minimum laser ablation area (~30 x 30 μm), with few particles generated. Alignment of the laser spot on the leg is critical to avoid accidental damage of the sled structure. Before actual cutting, several test cuts are repeated on other non-used sleds to optimize the cutting precision.

4.3 Simulation of the sleds

4.3.1 Analytical solutions for plates

Approximate solutions for the resonance frequencies and mode shapes are known analytically for completely free square and circular plates.[73] For example, the frequencies of a completely free square or circular plate are calculated using,

$$\omega_0 = \frac{\Omega}{a^2}\sqrt{\frac{D}{\rho t}} \sim \frac{t}{a^2} \tag{4.1}$$

where Ω is some constant dependent on the particular mode and Poisson ratio [see Table 4.61 in ref 73], a is the side length of the square plate or radius of the circular plate, ρ the density, and D is the bending stiffness of the plate,

$$D = \frac{Et^3}{12(1 - v^2)} \tag{4.2}$$

in which E is Young's modulus, t is the plate thickness, and v Poisson's ratio. One important conclusion is that for completely free plates the model frequencies are linearly proportional to the plate thickness, and this result is also found in the FEM simulations (section 4.3.2). Further, by measuring the plate resonant frequencies, we can estimate the thickness of a sled and our results show good agreement between the analytical value and the thickness of the same sled measured using SEM.

Analytical mode shapes can also be calculated using series solutions of the form,

$$W(\bar{x}, \bar{y}) = \sum A_{mn} X_m(\bar{x}) Y_m(\bar{y}) \tag{4.3}$$

in which $\bar{x}$ and $\bar{y}$ are normalized coordinates given by $\bar{x} = x/a$ and $\bar{y} = y/a$, $X_m(\bar{x})$ and $Y_m(\bar{y})$ are calculated functions [see Eqn 4.58 in ref 73], and A_{mn} are amplitude coefficients given for different modes [see Table 4.61 in ref 73]. Figure 4.10 shows the first 3 mode shapes for a completely free square plate and again the same results are found in the FEM calculations (section 4.3.2).

| Mode 1 | Mode 2 | Mode 3 |
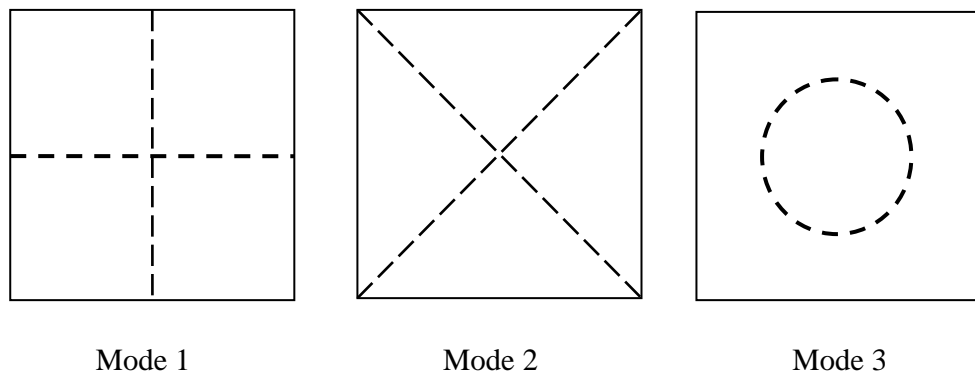
Figure 4.10 Analytical mode shapes for a completely free square plate

4.3.2 Comparison of FEM results between a completely free sled and an attached sled

A design assumption is that for actuation of sled movement we must vibrate at a sled resonance to achieve large movement of the tips and also ensure the tips are at anti-node locations for the given resonance. Therefore, we must measure the resonance frequencies and corresponding mode shapes of the sleds on a surface. This is difficult because the sleds are free standing and there is a problem of how to apply the vibration actuation.

In this section an indirect method is proposed for the measurement of dynamic properties of free standing MEMS structures. Briefly, the vibration modes and frequencies are measured by a vibrometer prior to the full release of the MEMS structure from the supporting substrate. By suitable design and positioning of small spring (cantilever) legs to hold the larger MEMS (sled) structure, one can achieve approximately the same vibration modes as for the free plate. It is much easier to measure a sled anchored to a chip rather than free on a surface.

The FEM vibration analysis of the plates is carried out by ANSYS. The material properties used are Young's modulus 150 GPa, Poisson's ratio 0.17, and density 2330

kg/m^3. Table 4.2 shows the natural frequencies of the completely free sleds studied and Figure 4.11 shows the corresponding mode shapes. For comparison we have also carried out FEM modelling for the sleds with tips, and the modelling results show that the tips have negligible effect on the vibration frequency and mode shape of a completely free plate. We only show the first four natural vibration frequencies. Higher modes are not of practical interest for actuation because the vibration amplitudes become very small.

We now present FEM modal analysis results for Silicon sled structures with attachment legs and compare with the corresponding results for the completely free sleds. Based on the results, the issues which influence the natural frequencies and the corresponding mode shapes, including leg positions, leg stiffness, leg shape and leg number, are discussed. In the modeling, the sled thickness (0.3 µm) and geometry (side length or diameter 200 µm) are the same as for the free plates (Table 4.2).

The natural frequencies and the corresponding mode shapes of square plates with different leg properties are shown in Table 4.3 and Figure 4.12. Three types of leg connections are studied, namely 2 and 4 leg connections of the leg type shown in Figure 4.12 (these are 0.3 µm thick cantilevers consisting of 3 sections of width 24 µm, length 29 µm; width 8 µm, length 29 µm; and width 4 µm, length 2 µm), and a 4 leg connection of a smaller stiffness leg type (cantilever of thickness 0.3 µm, width 8 µm, and length 60 µm). In the FEM modeling, clamped boundary conditions are defined at the leg ends connecting to the substrate chip.

Table 4.2 FEM results for the natural frequencies of free standing plates with different geometry.

Sled Thickness (μm)	Sled geometry	Natural frequency (kHz)			
		Mode 1	Mode 2	Mode 3	Mode 4
0.3	Square (side length: 200 μm)	40.9	58.7	66.1	102.6
	Triangle(side length: 200 μm)	96.2	108.6	242.9	276
	Circular (diameter: 200 μm)	64.4	97.6	148.0	228
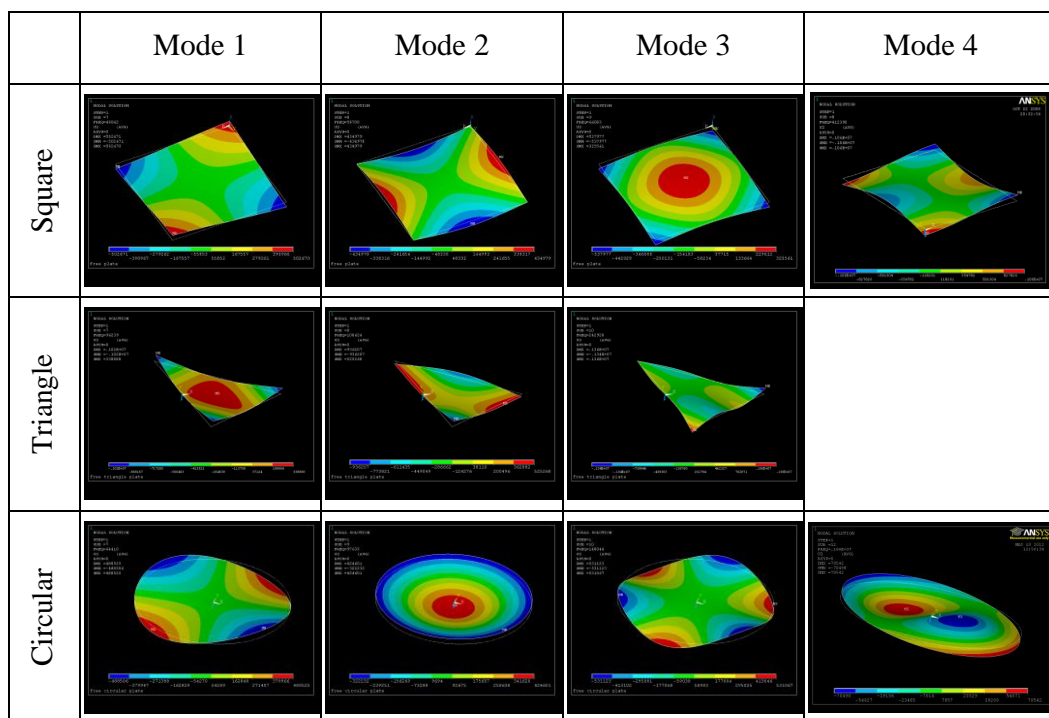
Figure 4.11 FEM results for the mode shapes of free standing plates with different sled geometry. The plate dimensions are given in Table 4.2

The existence of the legs creates additional resonances of the suspended plate structure e.g. modes 1-3 in Table 4.3. Images of all modes up to mode 10 for plates with legs were studied. However, Figure 4.12 only highlights the main data to be discussed and shows the 3rd, 4th and 5th mode shapes for square plates with legs. Only these modes match both

the mode shape and approximate frequency of the 1st, 2nd, and 3rd modes of the completely free plate (see Table 4.3). Note that for the sled with legs, different mode numbers correspond to the completely free plate modes. For example, the 1st mode of the free plate is matched to the 3rd mode of the plate with 4 legs and to the 4th mode of the plate with 2 legs.

In general (but not always) the presence of the legs stiffens the entire structure, resulting in an increase in the natural frequency. Again using the 1st free plate mode as an example, Table 4.3 shows that the resonance frequency increases from the free plate value of 40.9 kHz to 42.8 kHz for the 2 leg plate and 44.7 kHz for the 4 leg plate. The plate with fewer legs has less overall stiffness and hence the resonance is closer to the free plate value.

Similarly, the resonance frequency for the 4-leg plate attached using lower stiffness legs (43. 8 kHz) is closer to the free plate value in comparison with the stiffer leg structure. It is therefore recommended that to measure resonant frequencies that most closely match the resonance of the free plate, the legs connecting to plate should be as few as possible and of low stiffness. However, to faithfully image the mode shape it is also recommended to have symmetrical leg attachments. For example, the 5th mode of the plate with 2 legs is slightly distorted in comparison with the 4th mode of the 4-leg plate which has a totally symmetric arrangement of the legs (Figure 4.12).

The frequencies of plates with legs can also decrease compared to the corresponding free plate value. In these rarer cases we find the mode shape of the plate with legs has some node lines slightly closer to the centre of the plate, making the mode shape more flexible, i.e. a lower natural frequency, compared to its free plate equivalent.

Table 4.3 FEM results of natural frequencies of square plates (length 200µm, thickness 0.3µm) with different legs. The groups of frequency data with the same shading have similar mode shapes. Yellow for free mode 1, blue for free mode 2, pink for free mode 3, and green for free mode 4.

Plate with 2 legs		4 legs		4 lower stiffness legs		Free plate	
Mode	Freq. (kHz)	Mode	Freq. (kHz)	Mode	Freq. (kHz)	Mode	Freq. (kHz)
1	6.8						
2	12.5	1	21.1	1	16.5		
3	30.9	2	32.1	2	26.9		
4	42.8	3	44.7	3	43.8	1	40.9
5	65.0	4	71.1	4	70.3	2	58.7
6	79.1	5	90.9	5	81.5	3	66.1
7	104	6	110	6	108	4	103

geometry	3rd mode	4th mode	5th mode
Square sled with 2 legs			
Square sled with 4 legs			
Square sled with 4 lower stiffness legs			
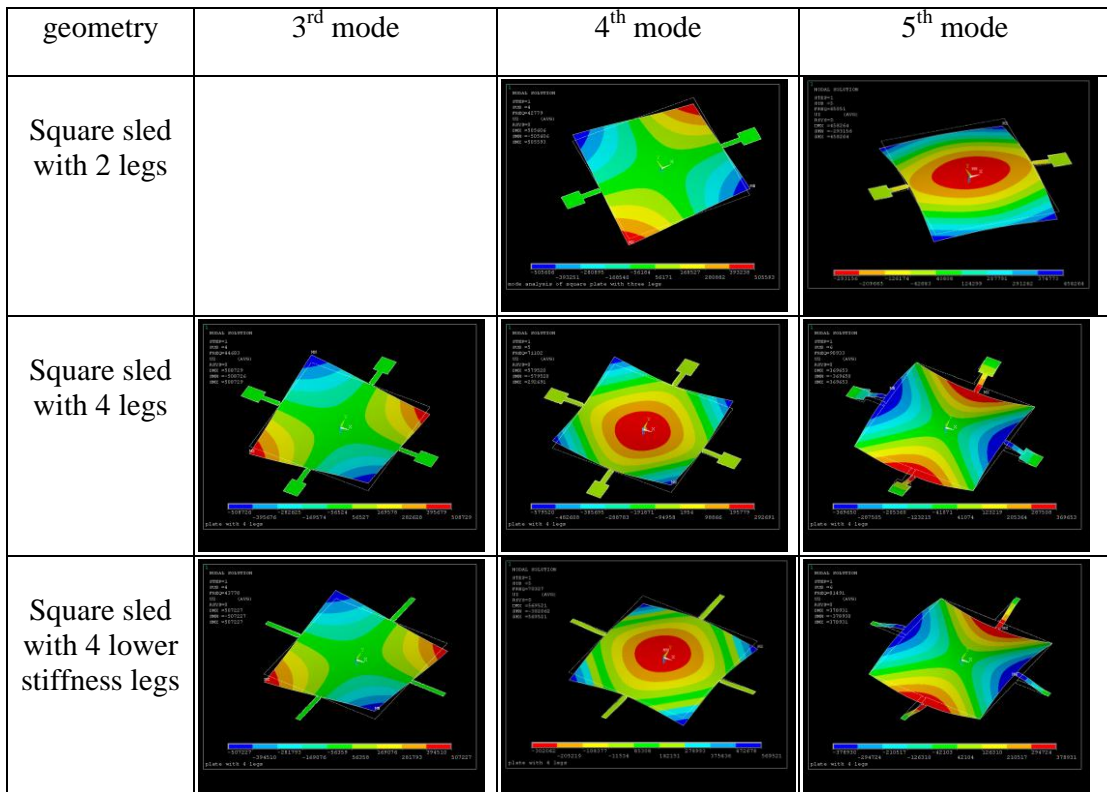
Figure 4.12 FEM results for mode shapes of square sleds with different legs (length 200µm, thickness 0.3µm). Data is shown only for those modes which match a corresponding free plate mode as shown in Figure 4.11.

A more critical factor is the position of the legs. Consider the plate with 4 legs. The 3rd mode matches mode 1 of the free plate but the 4th mode matches mode 3 of the free plate and the 5th mode matches mode 2. That is, the order of these modes has been reversed

comparing the plate with and without legs. Table 4.3 shows the frequency of the 2nd mode of the free plate (58.7 kHz) has increased significantly (to ≥ 80 kHz) because of the leg attachment. This observation also holds for the plate with 2 legs. The reason for this behavior is that in this case the legs are attached at anti-node positions for the 2nd mode of the free plate and this leads to a large effective stiffening of the plate for that specific mode shape. The 1st and 3rd free plate modes are satisfactorily reproduced because the attachment locations are at a node. It is therefore important to place the legs at node positions to faithfully mimic the movement of the free plate. In the example given, if one wish to measure the 2nd mode of the free plate, the legs should attach at the corner of the square plate.

Another interesting observation is that the leg shape can be important. Table 4.4 and Figure 4.13 show FEM results for an equilateral triangular plate attached by 3 legs of different shapes. One set of legs is straight and identical (a three section cantilever structure of thickness 0.3 μm, and width 24 μm, length 86 μm; width 8 μm, length 11 μm; width 4 μm, length 5 μm). The other set has 2 of the legs being longer with a kink near the end connecting to the substrate chip (kink section width 24 μm with one side length 16 μm and the other 28 μm). In the geometry in which all 3 legs are straight, mode shapes can be found which match the free plate modes in both shape and natural frequency. Specifically, the 3rd and 4th modes of the triangular plates with the straight legs match the 1st and 2nd modes of the free triangular plate respectively (see Figure 4.11). However, for sleds having non-straight and asymmetric attachment legs, none of the mode shapes were comparable to the 1st, 2nd or 3rd vibration modes of the free plate. In this case, measurement of the sled structure when attached cannot be used to infer the dynamic properties of the free sled. It appears that the actuation does not couple into the suspended

plate in a simple manner, leading to complex vibration modes of the plate which cannot

be related simply to the free plate.

Table 4.4 FEM results for the natural frequencies of triangle plates (length 200µm, thickness 0.3µm) having different leg shapes. The groups of frequency data with the same shading have similar mode shapes. Yellow for free mode 1, and blue for free mode 2.

Plate with 3 non-straight legs		Plate with 3 straight legs		Free plate	
Mode	Frequency (kHz)	Mode	Frequency (kHz)	Mode	Frequency (kHz)
1	12.8	1	15.5		
2	24.0	2	26.8		
3	25.2	**3**	**95.9**	**1**	**96.2**
4	88.4	**4**	**101.2**	**2**	**108.6**
5	94.5	5	101.2	3	242.9

Geometry	3rd mode	4th mode	Geometry
Plate with 3 straight legs			
Plate with un-straight legs			
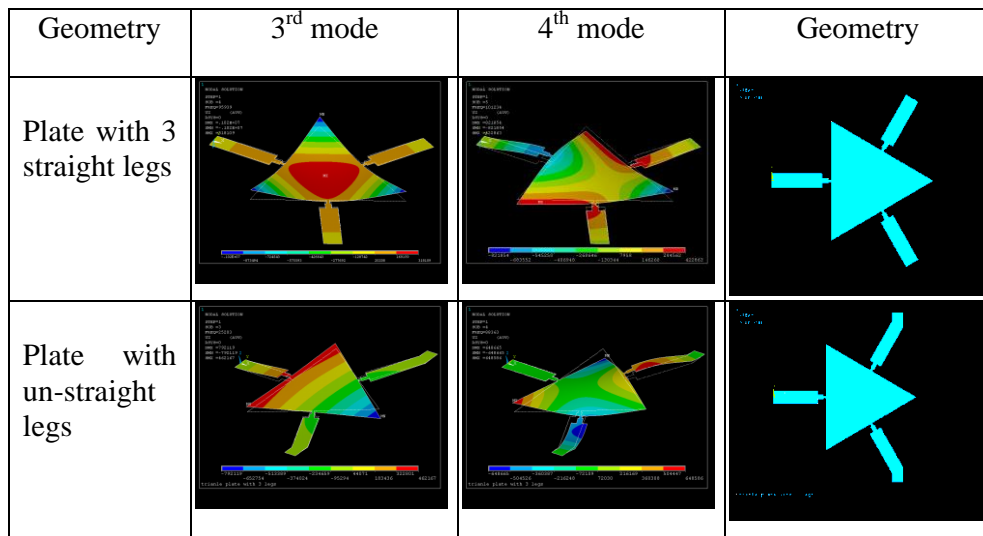
Figure 4.13 FEM results showing mode shapes of equilateral triangle plates (length 200µm, thickness 0.3µm) having different leg shapes.

From the FEM modelling results, it is shown that the resonance frequencies and the corresponding mode shapes of completely free plate structures approximate to those of suspended structures provided the attachment legs are properly designed. The legs should satisfy the following design criteria.

i)   The legs must be identical and their arrangement symmetrical.

ii) The leg stiffness should be low.

iii) To study a particular mode, the legs should be placed at the node of the mode shape.

In the cases studied, the mode shapes are slightly distorted by the presence of the legs but can be discerned; and with suitable design the difference in resonance frequencies can be small e.g. Table 4.3 shows a difference in frequency of ~5% for a square plate with and without legs.

4.3.3 Other factors influencing sled resonance modes

Following the above recommendations, the dynamic properties of a free standing MEMS structure can *in principle* be indirectly measured before release from the supporting chip. However, practical considerations will also influence the outcome of any such experiment and in this section we study, using FEM, changes in sled mode shape and resonant frequency arising from the addition of a magnetic particle on the sled, and the effect of the tip-substrate contact through the tips.

4.3.3.1 Effect on sled resonance of an attached magnetic particle

The effect of placing a large magnetic particle on the resonance modes of a sled was modelled for a silicon circular sled (300 μm diameter, 1.3 μm thickness). Note that in the results presented, the resonance frequencies are scaled by 3/1.3=2.306 (see section 4.3.1) so the frequency data corresponds to a 3 μm thick sled. This enables easier comparison with data taken on the thick manufactured sleds (Chapter 6). In the model, the magnetic particle has diameter 44 μm and density 5000 kg/m^3. Experimentally it is difficult to position a magnetic particle exactly in the centre of a sled and therefore two cases are studied; the particle in the exact center (0,0) or off-center (-24 μm, 17 μm), the later being a measurement from a real sled. Cases were also investigated with and without two

spring legs attaching the sled to the surrounding chip. Two different types of leg were studied; simple rectangle bars (length of 100μm, width 4μm, thickness of 1.3μm), or softer 2-stage legs (thickness 1.3μm).

Results of the resonance modes of a completely free sled (300 μm diameter, 3 μm thickness) with no attached particle are shown in Figure 4.14. The modes are highlighted in yellow for free mode 1, blue for free mode 2, pink for free mode 3, and green for free mode 4. Figure 4.15 shows a free sled with a particle at the center; Figure 4.16 a free sled with the particle placed off-center; and Figure 4.17 a sled with off-center particle attached by 2 legs. In Figures 4.15Figure 4.15-4.17, the modes corresponding to the completely free sled with no added mass (i.e. Figure 4.14) are also highlighted in yellow for free mode 1, blue for free mode 2, pink for free mode 3, and green for free mode 4.

Mode 1	Mode 2	Mode 3	Mode 4
286 kHz	434 kHz	658 kHz	1013 kHz
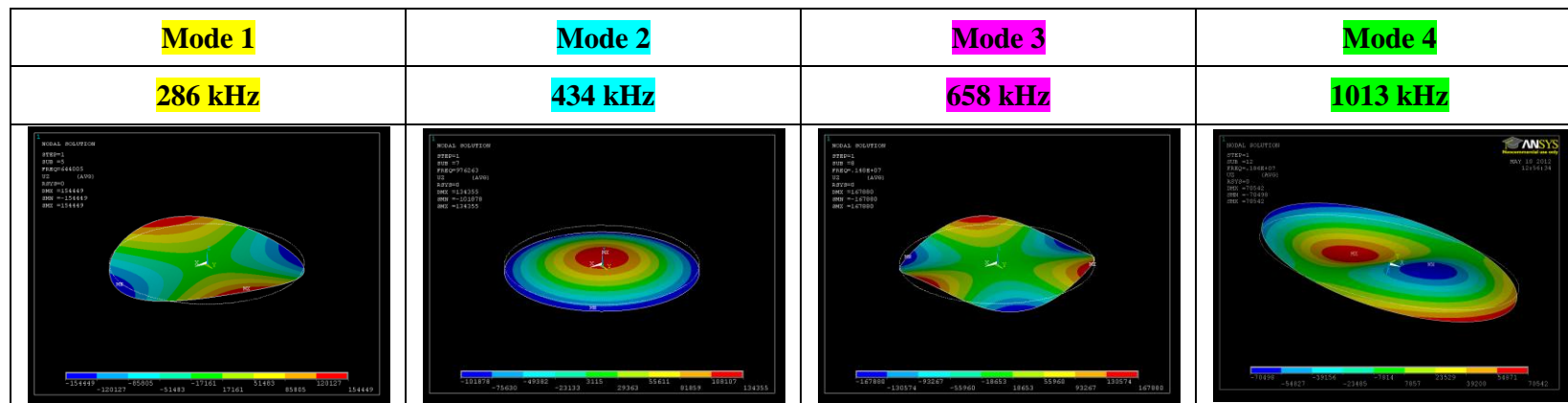
Figure 4.14 Simulation of the resonance modes of a completely free sled (300 μm diameter, 3 μm thickness) with no attached particle. The modes are highlighted in yellow for free mode 1, blue for free mode 2, pink for free mode 3, and green for free mode 4.

Mode 1	Mode 2	Mode 3	Mode 4	Mode 5
4.1 kHz	286 kHz	310 kHz	665 kHz	880 kHz
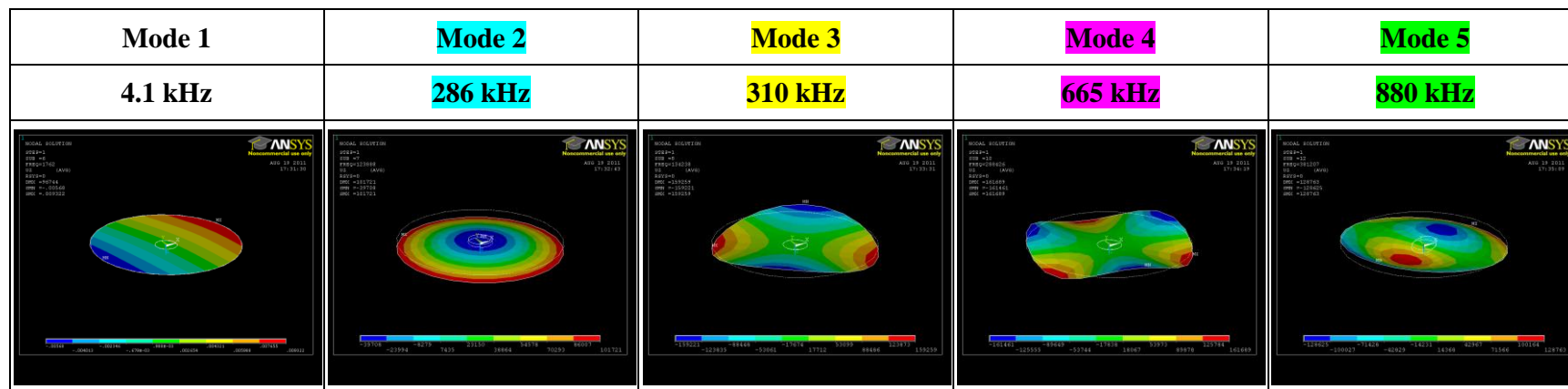
Figure 4.15 Simulation of the resonance modes of a free sled (300 μm diameter, 3 μm thickness) with a particle at the centre. The modes corresponding to the completely free sled are shown in yellow for free mode 1, blue for free mode 2, pink for free mode 3, and green for free mode 4.

Mode 1	Mode 2	Mode 3	Mode 4
4.0 kHz	299 kHz	307 kHz	312 kHz
Mode 5	Mode 6	Mode 7	
670 kHz	850 kHz	904 kHz	
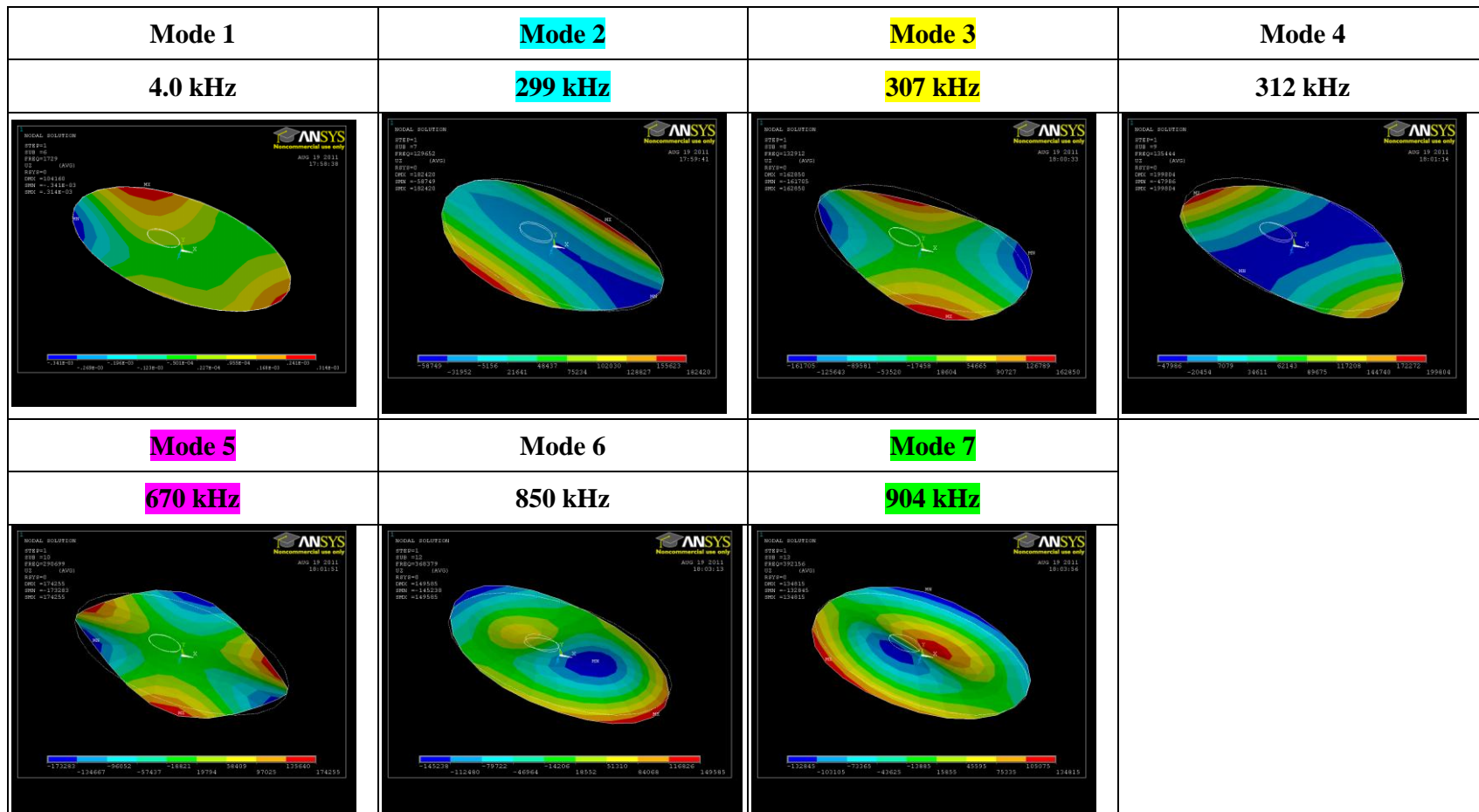
Figure 4.16 Simulation of the resonance modes of a free sled (300 μm diameter, 3 μm thickness) with the particle placed off-center. The modes corresponding to the completely free sled are shown in yellow for free mode 1, blue for free mode 2, pink for free mode 3, and green for free mode 4.

Mode 1	Mode 2	Mode 3	Mode 4	Mode 5
29.4 kHz	50.7 kHz	203 kHz	303 kHz	314 kHz

Mode 6	Mode 7	Mode 8	Mode 9	
457 kHz	676 kHz	732 kHz	855 kHz	
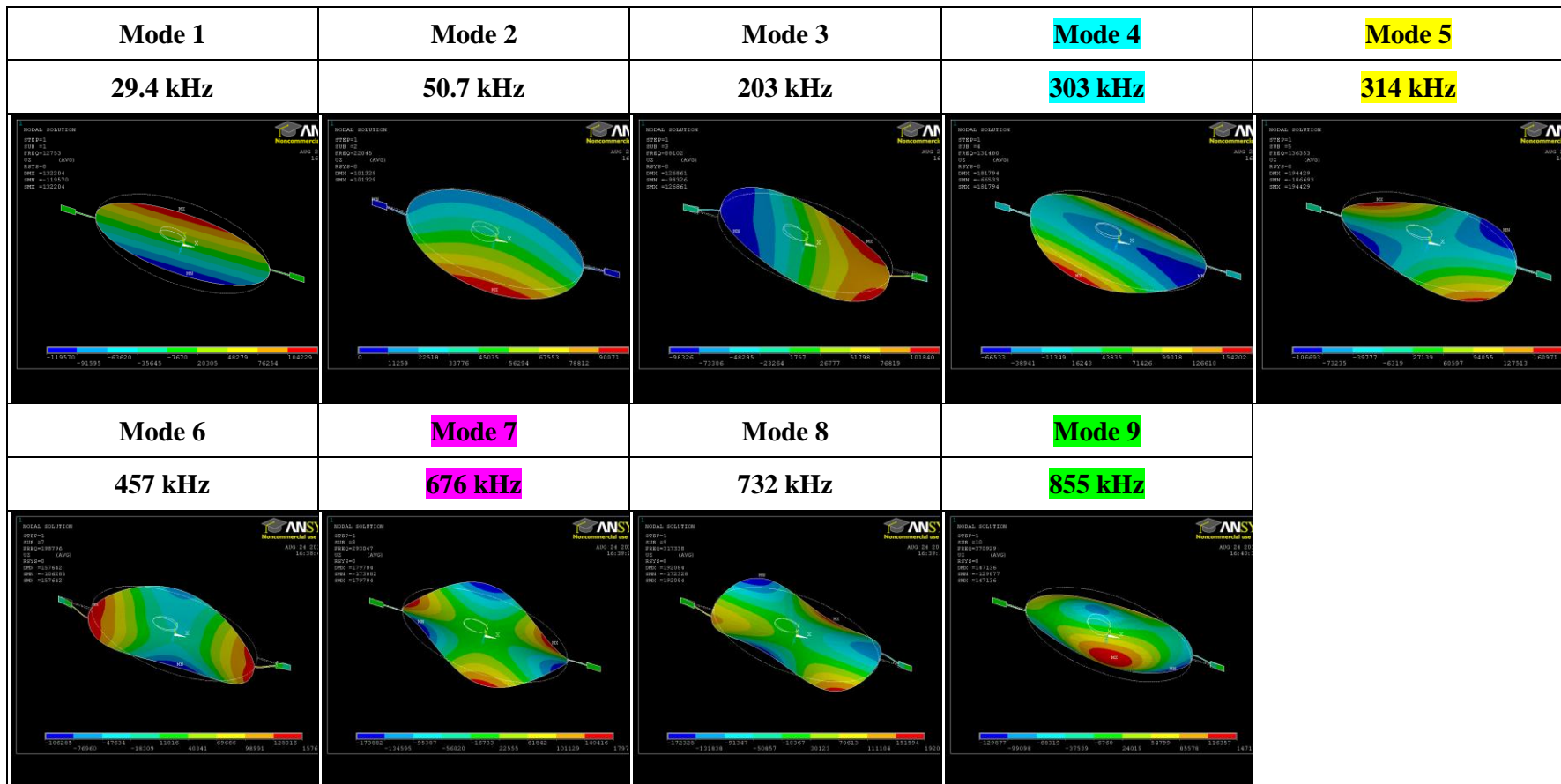
Figure 4.17 Simulation of the resonance modes of a sled (300 μm diameter, 3 μm thickness) with off-center particle and sled attached by two soft 2-stage legs. The corresponding free sled modes are in yellow for free mode 1, blue for free mode 2, pink for free mode 3, and green for free mode 4.

The FEM results for sleds with attached particles can be summarized as follows.

a) The mode shapes are similar or only slightly distorted compared to the free plate modes, except for free mode 2 which becomes highly distorted if legs are attached or the particle is off-centre.

b) The resonance frequencies are close to the free plate values for free modes 1 and 3, but are much lower for mode 2 (decrease ~35%) and mode 4 (decrease ~13%). The reason is that the central region of the plate is moving for modes 2 and 4, so the placing of the particle in the central region changes the effective plate mass for these modes.

c) The changes created by having the particle on or off-centre are important but of modest magnitude. Comparing the on and off-centre cases, free mode 2 becomes distorted but the resonance frequency difference is less than ~5% with simple rectangular legs or ~10% with softer 2-stage legs. The change in resonance frequency for the other free modes is less than ~2.5% with simple rectangular legs or ~7% with softer 2-stage legs. New modes are also generated when the symmetry is broken with the off-centre mass (Figure 4.16), although it is not clear if these new modes could be used for magnetic actuation of a free sled as the amplitude of the motion is not known.

d) Many more modes are created when legs are attached, as previously discussed in section 4.3.2. The frequencies of the free modes change by less than 5% with the addition of the two legs. A useful observation to determine which modes are associated with free modes is that for free modes the legs do not bend appreciably, whereas for non-free modes the legs are displaced (excepting the lowest mode e.g. mode 1 in Figure 4.17).

e) Doubling of the particle mass decreased the frequency of free mode 2 by 5% and less than 1% for the other free modes (data not shown).

In summary, the simulations suggest that with care one can also relate the resonance modes of a sled with an attached particle to the modes of a completely free sled, although the case is complicated by the added mass.

4.3.3.2 Effect on sled resonance on tip location and tip-substrate stiffness

When a sled is placed on a substrate, the three tips are touching and this introduces additional stiffness to the plate motion. In FEM, we model this additional tip stiffness (k_{eff}) as a spring perpendicular to the plate, and $k_{eff} = \left(\frac{1}{k_{tip}} + \frac{1}{k_{contact}} \right)^{-1}$, where k_{tip} is the stiffness of the tip apex and $k_{contact}$ is the AFM tip-surface contact stiffness.[74] This equation is fully discussed in Chapter 5. Briefly, a sharp tip has a small spring constant and a blunt tip has a large spring constant. For a Hertz contact model,

$$k_{contact} \approx 2 \left(\frac{3RF}{4E^*} \right)^{1/3} E^* \qquad (4.4)$$

where E* is the effective Young's modulus, R the tip radius and F the applied force. Even for very sharp tips (R~10 nm) and low load (F~10 nN), one obtains $k_{contact}$~150 N/m for silicon contacts. Such relatively high contact stiffness has been confirmed experimentally using AFM tips.[74] However, very sharp tips can also be flexible from the geometry of the tip shape, giving small values of k_{tip} (~10's N/m)[75] and $k_{eff} \approx k_{tip}$. For these reasons the values $k_{eff} \approx 3, 30,$ or 300 N/m were chosen for study in the simulation.

FEM simulations for a square sled (300 μm×300 μm, thickness 3 μm) with non-symmetrically placed tips are shown in Figure 4.18. Table 4.5 shows that if k_{eff} is small (3 or 30 N/m) the frequency remains close that of the free plate, excepting for an additional low frequency resonance (mode 1) which corresponds to a rocking of the plate

on the tips. The mode shapes are also similar. However, if k_{eff} is high (300 N/m) additional low frequency resonances occur (modes 1-3) and higher plate resonance frequencies (modes 5 and 6) can change significantly from those of a free plate ($k_{eff} = 0$). The reason for this is the mode shapes become distorted if the substrate-to-plate coupling is strong (compare modes 5 and 6 in Figure 4.18 with the free plate modes 1 and 3). If the mode shapes are not strongly distorted (e.g. modes 4 and 7), because the tips are on the node lines, the data remains similar to the free plate case.

Thus to maintain the free standing sled resonance modes close to the free plate values requires low values of k_{eff}. It is difficult to reduce $k_{contact}$ because E* must remain high for superlubricity[5], the inertia of a sled is already very small (typically F~1nN), and a tip radius of R~10nm is a lower limit for practical applications. A possibility is to design flexible tips such that k_{tip} is very small, but such an approach may remove the ability to achieve low friction because stick-slip will be occur.

The best method, which was not considered in the initial designs, appears to be to carefully choose the location of the tips to minimize mode distortion yet maintain tip motion at resonance. Figure 4.19 shows FEM results for a 300 μm diameter circular sled of 5.5 μm thickness with tips placed symmetrically near the rim. In this case the mode shape and resonance frequencies (modes 3-6) are similar to the free plate modes (modes 1-4), even with a high value of tip interaction ($k_{eff} = 300$N/m). Two additional low frequency modes (modes 1-2), arising from a rocking motion of the plate, do depend strongly on the tip-substrate contact.

Table 4.5 Resonance frequencies of square plates (side length 300 μm, thickness 3 μm) with different tip stiffness k_{eff}. The frequency data shown with the same colour have mode shapes comparable to a free plate mode. Yellow for free mode 1, blue for free mode 2, pink for free mode 3, and green for free mode 4.

Mode	Frequency (kHz)			Mode	Frequency (kHz)
	k_{eff}=300 N/m	k_{eff}=30 N/m	k_{eff}=3 N/m		Free plate ; k_{eff}=0
1	101.1	74.7	23.9		
2	131	195	183	1	182
3	201	264	261	2	261
4	286	296	294	3	294
5	300	459	458	4	458
6	338	462	459	5	835
7	474	767	767		

Free plate : mode 1	mode 2	mode 3
k_eff = 300 N/m : mode 1	mode 2	mode 3
k_eff = 300 N/m : mode 4	mode 5	mode 6
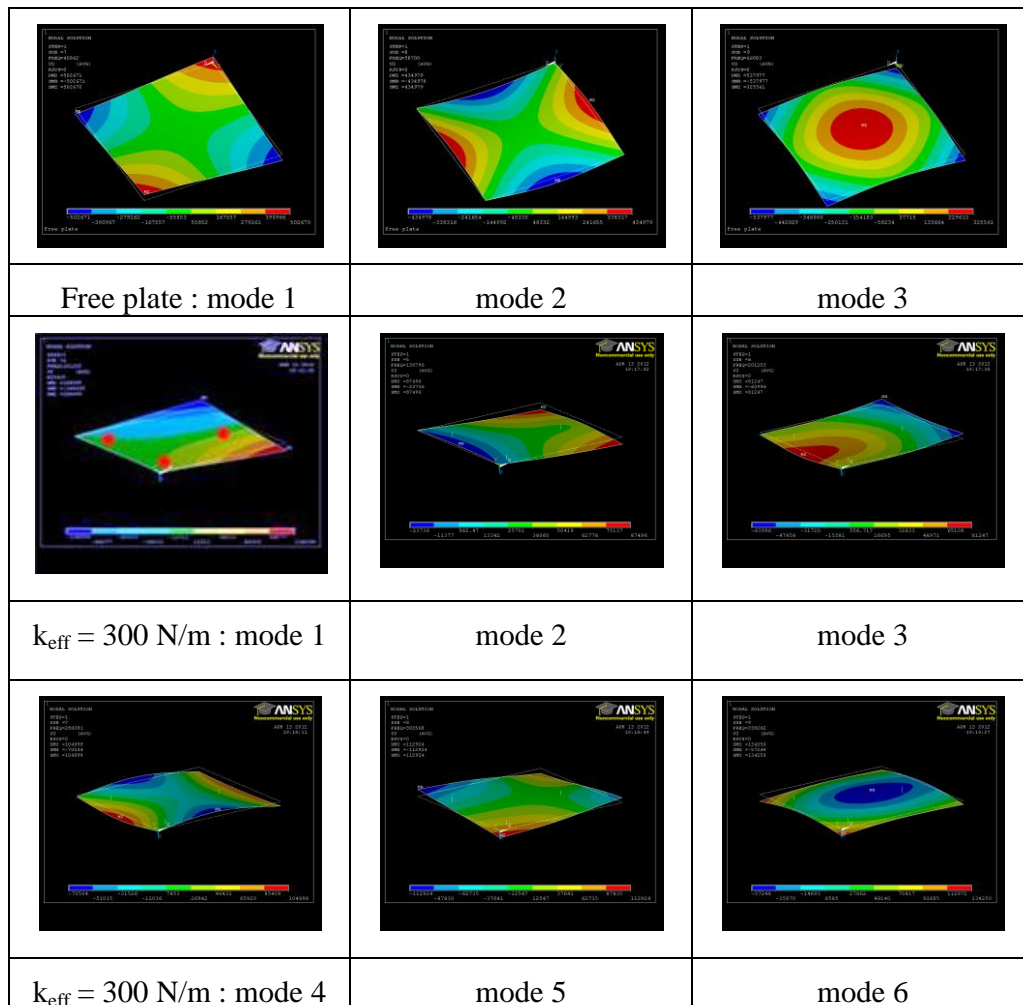
Figure 4.18 Comparison of mode shapes for a square free plate (side length 300 μm, thickness 3 μm) and a plate with tip stiffness $k_{eff} = 300$ N/m. The corresponding frequencies are given in Table 4.5. The red dots in the image for $k_{eff} = 300$ /mode 1 show the approximate location of the tips.

Table 4.6 Resonance frequencies of circular plates (300 μm diameter, 5.5 μm thickness) with different tip stiffness k_{eff}. The frequency data shown with the same colour have mode shapes comparable to a free plate mode. Yellow for free mode 1, blue for free mode 2, pink for free mode 3, and green for free mode 4.

Mode	Frequency (kHz)			Mode	Frequency (kHz)
	k_{eff}=300 N/m	k_{eff}=30 N/m	k_{eff}=3 N/m		Free plate ; k_{eff}=0
1	152	50	16		
2	174	59	19		
3	564	529	526	1	525
4	803	797	796	2	796
5	1240	1210	1207.3	3	1207
6	1859	1858	1858	4	1858

mode 1	mode 2	mode 3
mode 4	mode 5	mode 6
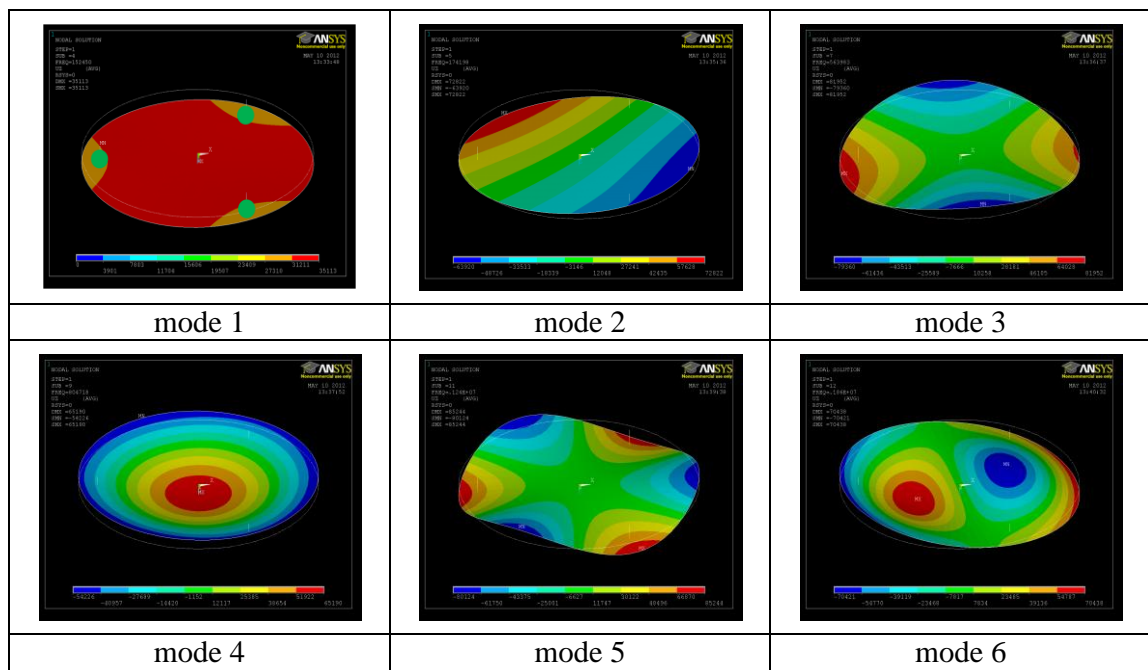
Figure 4.19 Mode shapes for a circular plate (diameter 300 μm, thickness 5.5 μm) with tip stiffness $k_{eff} = 300$ N/m. The corresponding frequencies are given in Table 4.6. The green dots in the image for mode 1 shows the approximate location of the tips. Modes 3-6 are very similar to the free plate modes.

4.4 Conclusion

The work in this chapter reports the microfabrication of the sleds and the FEM simulation results. Two types of sleds, ultra-thin plate (300 nm) and thick plate (3 μm thick), were fabricated incorporating 3 sharp tips. The major fabrication challenges and their solution are described. The FEM analysis was undertaken to understand the resonance modes of sleds attached to the process chip, completely free sleds, sleds placed on a surface, and sleds with and without a magnetic particle placed near the centre.

Chapter 5 Friction Measurement on Free Standing Sleds Using AFM

In this chapter, a method is introduced to measure friction on free standing sleds based on atomic force microscopy (AFM). An AFM tip is brought into contact with the sled resting on a substrate. The substrate is displaced laterally and, provided the AFM tip does not slide over the sled, the twisting of the AFM cantilever is used to measure the friction of the underlying sled-substrate interface. The method can measure nano-Newton to micro-Newton forces (both friction and applied load) and provides a general means to measure friction of small free-standing structures at low load.

5.1 Introduction

There are many instances when it is of interest to measure the friction acting between small, free standing objects and an underlying surface. For example, in the removal of microorganisms for membrane technology,[76] in the cleaning of particles from a surface,[77] in the sliding of two surfaces in microelectromechanical (MEMS) systems,[78,79] or simply moving paper on a desktop. In this thesis, we must measure friction of free standing sleds as a first step toward bridging nanoscale tribology concepts, such as superlubricity and AFM point contacts, to macroscale dimensions.[80-82] However, an experimental difficulty arises, namely how can the friction be measured on a free standing object of only micron dimension? Macroscopic tribometer methods, usually pin-on-disc instruments, cannot be used as spatial constraints e.g. the diameter of the ball in a pin-on-disk tribometer, impose a limitation on the smallest sized object that can be studied. The minimum applied load and friction force are also high for MEMS studies[83] e.g. >10μN for a typical "nano-tribometer[84].
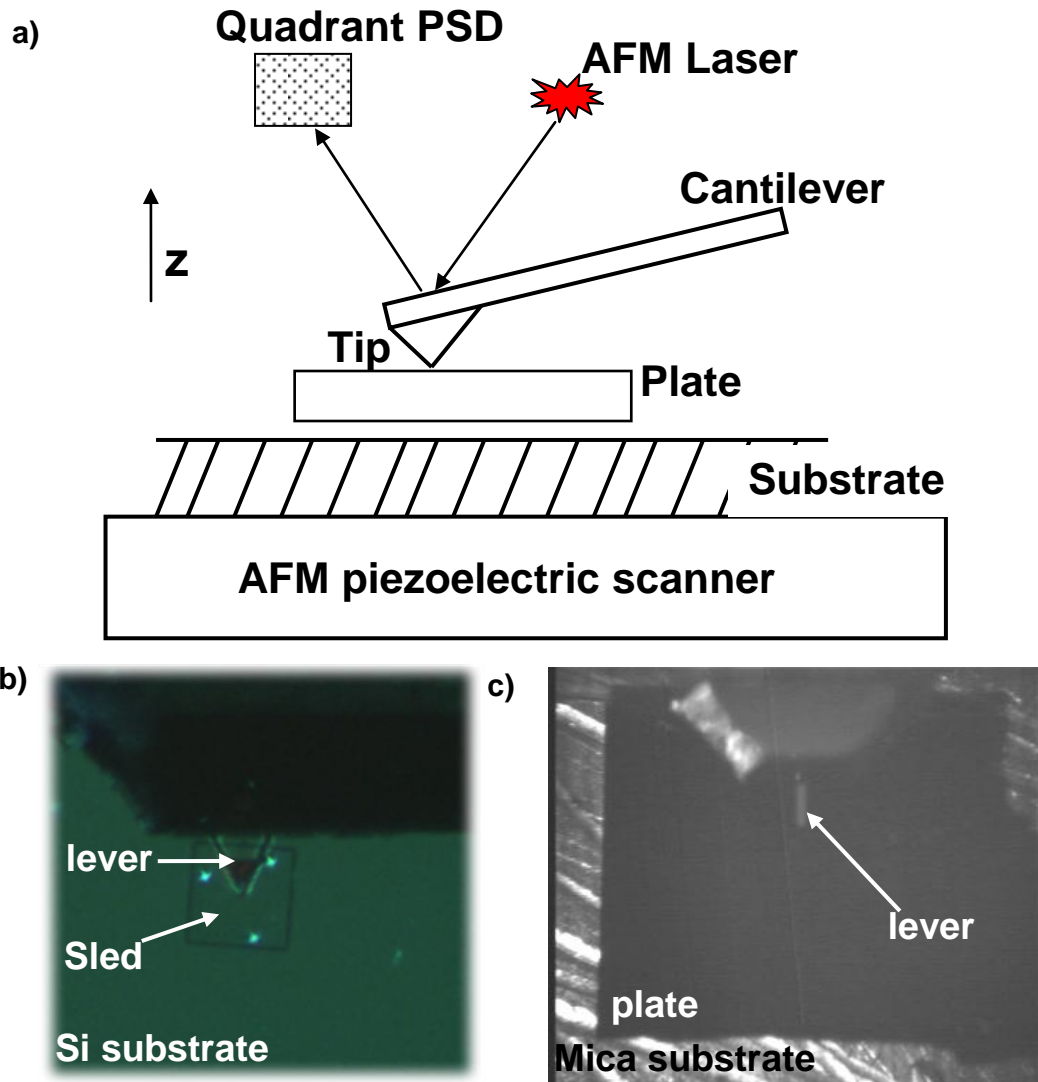
Figure 5.1 a) The friction force measurement approach. The AFM cantilever exerts a force on a free standing plate resting on a substrate. The AFM piezoelectric scanner moves the substrate (or alternatively, the cantilever) laterally. The resulting twisting of the lever can be used to measure the magnitude of the friction forces acting at the plate-substrate interface, provided the tip-plate contact does not slip. A position sensitive detector (PSD) is used so that the absolute movement of the cantilever deflection can be found. b) The method applied using a triangular Si_3N_4 cantilever in contact with a microfabricated (300 μm square) sled. c) The implementation of the method in an AFM, showing a Si cantilever in contact with a large (3 mm square) Si plate.

We introduce a method to measure friction on free standing surfaces based on AFM. The method is outlined in Figure 5.1a and demonstrated using 300x300 μm square sleds as samples (Figure 5.1b). We have also shown the method is feasible on much larger (millimetre) plate structures (Figure 5.1c). The plate is placed on a substrate within an AFM fitted with optical imaging capability. The plate is positioned underneath the AFM

tip and the tip brought into contact with the plate. The AFM tip exerts a force in the normal (z) direction on the plate. If the plate is then made to move laterally with respect to the surface (x direction) the twisting of the AFM cantilever can be used to measure the magnitude of the friction as in standard friction force AFM.[43] The lateral movement can be provided by moving either the sample or the cantilever. Provided the plate slips on the surface before the tip slips on the plate and this can be verified optically. The measurement gives the friction acting at the plate-substrate interface, with the AFM cantilever acting as the sensor element.

The technique is similar to the Mesoscale Friction Tester described by Wang *et al* [85] and similar slider type tribometers[86], excepting that our approach is designed for general AFM usage. Their approach and our method bridge the nano-to-micro measurement range, in terms of both force and length scale. There is a notable gap between nano-tribometer and AFM instrumentation in this force range.[85,86,87] Also noteworthy is the similarity with AFM experiments that manipulate nanoparticles or nano-scale islands.[88,89] These studies use the AFM tip to move a nano-island on a surface and the associated friction is measured by the twisting of the AFM cantilever as the tip *encounters the edge* of the nano-island. The method shown in Figure 5.1 could be adopted to nano-island experiments to measure the friction as a function of normal load; an important additional measurement that is currently not undertaken because the AFM tip simply pushes the edge of the nano-island (or nanoparticle) to initiate lateral movement.

The chapter is organized as follows. We first provide a simple analytical framework for the technique, including the conditions required for the AFM tip to remain fixed to the sample plate during sliding (section 5.2.1) and AFM cantilever stiffness considerations for the friction force measurement (section 5.2.2). The experimental implementation of the approach is then demonstrated (section 5.3) and the results and observed technical

issues discussed (section 5.4). We conclude with a summary of the usefulness, application and possible improvements of the method (section 5.5).

5.2 Theory analysis of AFM–plate sliding

5.2.1 Ensuring no slip of the AFM tip

In the new method (Figure 5.1a) a key requirement is to ensure the tip-plate contact does not slip i.e. the plate must slide on the substrate before the AFM tip slides on the plate. In the simplest case sliding will occur when the measured lateral force (F_L) reaches the limiting static friction force (F_f) at the respective interface, as given by Amonton's Law (see Figure 5.2a),

$$F_L = F_f = \mu_t F_n \ \ or \ \ F_L = F_f = \mu_s F_n \tag{5.1}$$

where the subscript t denotes the tip-plate contact, subscript s the substrate-plate contact, μ the static coefficient of friction and F_n the normal force applied by the cantilever. Note that given the experimental uncertainties in our study we make no distinction between the static and dynamic friction coefficient. The applied force F_n is identical for the tip-plate and the plate-substrate contact. The lateral force F_L is also identical for both contacts if it is assumed the only elastic restoring force is the cantilever spring. Thus in this simple case, Eqn. 5.1 shows the plate will slip before the tip (the desired outcome) provided,

$$\mu_s < \mu_t \tag{5.2}$$

In order to provide a general method over a wide range of samples, a large μ_t is required. In principle, one could glue the AFM tip to the sample so that no possible slip occurs ($\mu_t \rightarrow \infty$) but for a non-destructive technique a strong, reversible contact is preferred e.g. using a tacky tip-sample contact, an adhesive coating on the tip, very rough tip-sample contacts, or specialized tips such as colloid beads. An interesting aside related to

stopping the tip sliding, is that we attempted to lock the AFM tip into micron sized holes microfabricated clear through a Silicon plate. This "lock-key" method does work and the AFM tip moves the plate across the substrate. Unfortunately, the sensitivity of the friction measurement falls dramatically because the effective tip height decreases when the shank of the AFM tip engages the hole (see Eqn. 5.5 below). Future experiments could explore the use of plate surfaces with shallow rather than clear-through holes or simply roughened plate surfaces. However, in the experimental work presented below, no coatings or special tips are used.

Equation (5.2) is itself overly simplistic because in general adhesion forces (F_{ads}) are present.[63] One expects the adhesive force from the small contact area of the AFM tip will be less in comparison with the adhesion at the plate-substrate contact. Van der Waals attraction is also present between two closely spaced surfaces and whilst negligible for the AFM tip contact can be very significant for large area plates.[90,91] Thus, although the applied load F_n is identical for both AFM tip-plate and plate-substrate contacts, the total load ($F_n + F_{ads}$) is not. The adhesion term depends on the surface chemistry and roughness.[18] For very smooth plates the adhesion (stiction) of the plate-substrate will dominate over the AFM tip-plate contact, and even for very rough surfaces the plate-substrate adhesion will probably be larger because there are more asperities in contact at the plate-substrate in comparison to the single asperity of the AFM tip-plate contact. For rough surfaces, if N asperities are in contact, the applied force (F_n) is distributed over all contacting asperities i=1 to N such that $F_n = {}^1F + {}^2F + ... + {}^NF$, with the applied force at the ith asperity being ${}^iF$. Ignoring adhesion, Eqn. (5.2) remains valid if the coefficient of friction is the same for each asperity contact. However, if adhesion is included, the adhesion force for the ith asperity contact (${}^iF_{ads}$) depends on the details of the contact, including the contact area, asperity geometry, and relative humidity (Figure 5.2b), making the analysis

of adhesion effects difficult for real surfaces.[92,93] Another major difficulty is the relation

between friction and adhesion is not well understood, except for molecularly flat

surfaces.[91]
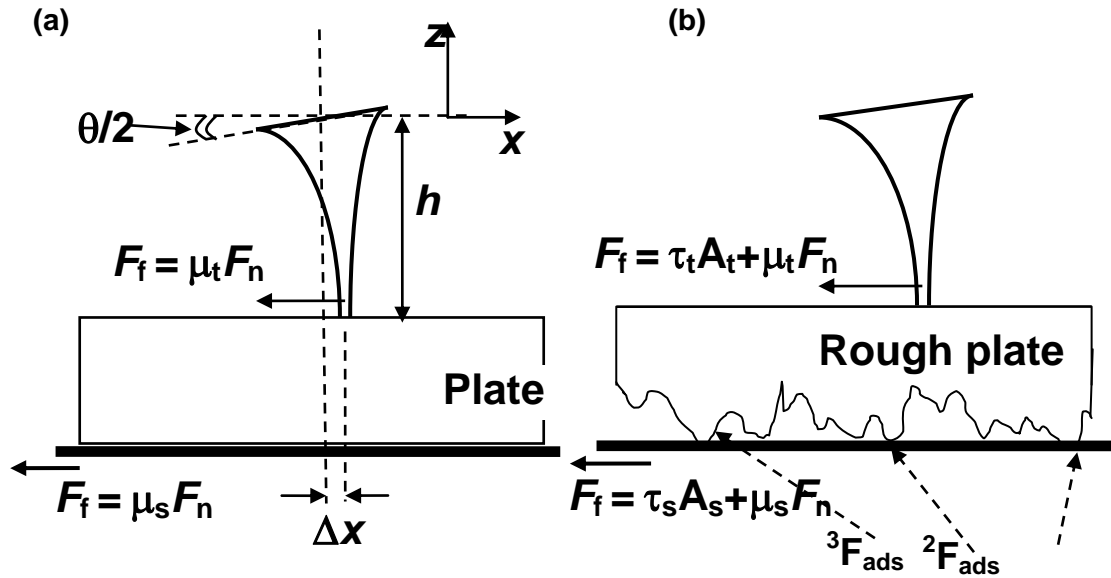
Figure 5.2 Schematics showing the basic analytical elements of the method. (a) The case with no adhesion. (b) The case with adhesion and a rough plate surface.

We assume the friction force in the presence of adhesion is given by,[81,87,94]

$$F_f = \tau_t A_t + \mu_t F_n \ \ or \ \ F_f = \tau_s A_s + \mu_s F_n \tag{5.3}$$

where τ is an interfacial shear strength of the contact,[95,96] A_t is the AFM tip-plate contact

area, and A_s is the total (multi-asperity) plate-surface contact area, assuming τ_s is the same

for all substrate asperity contacts (Figure 5.2b). The condition for the plate to slip before

the tip is,

$$\tau_s A_s + \mu_s F_n < \tau_t A_t + \mu_t F_n \tag{5.4}$$

At high applied force the load is dominated by F_n ($F_n >> F_{ads}$) and the plate slides before

the AFM tip if $\mu_s < \mu_t$ i.e. Eqn. 5.2. Conversely, at low force, the load may be adhesion

controlled [6] and the plate slides before the tip if $\tau_s A_s < \tau_t A_t$. Given that the plate-substrate

area is typically much greater than the AFM tip contact area ($A_s \gg A_t$), the measurement method at low load is only feasible for very low shear strength plate-substrate interfaces (τ_s), unless the tip is, for example, glued to the plate ($\tau_t \to \infty$).

5.2.2 The AFM cantilever as friction sensor

Another important issue with the technique regards the use of the AFM cantilever as a friction sensor.[43] Consider the lateral force measured by the cantilever,[58]

$$F_L = k_{eff} \Delta x = k_{eff}\, h\, tan(\theta/2) \tag{5.5}$$

where Δ x is the displacement of the plate, h is the height of the AFM tip, θ is the angle by which the laser beam is deflected (Figure 5.2a), and the effective lateral spring constant (k_{eff}) is,

$$k_{eff} = \left(\frac{1}{k_{xT}} + \frac{1}{k_x} + \frac{1}{k_{tip}} + \frac{1}{k_{contact}} \right)^{-1} \tag{5.6}$$

where k_{xT} is the torsion stiffness of the AFM cantilever, k_x is the in-plane cantilever stiffness, k_{tip} is the stiffness of the tip apex, and $k_{contact}$ is the AFM tip-surface contact stiffness.[75,97] Note that in friction force AFM, the torsion stiffness k_{xT} is the ratio of the lateral force at the tip and the corresponding lateral displacement, with units N/m.

A first consideration is k_{eff} should be dominated by the cantilever stiffness (k_{xT}) and not k_{tip} or $k_{contact}$. This is because if the springs k_{tip} and $k_{contact}$ are much smaller than k_{xT}, then on displacing the plate the measured AFM friction signal will have significant components arising from large displacements corresponding to k_{tip} and $k_{contact}$; a common situation in AFM when sharp tips are used at low load.[58] Since it is very difficult to accurately find k_{tip} and $k_{contact}$,[75] the best procedure is to negate the effect of these springs by using a blunt tip and/or a high load, thus ensuring $k_{tip} \gg k_{xT}$ and $k_{contact} \gg k_{xT}$, giving $k_{eff} \approx k_{xT}$ (Eqn. 5.6). The effect of blunting the AFM tip can be shown by considering the elastic contact of a sphere on a flat, in which,

$$k_{contact} \approx 8aG^*$$ (5.7)

where a is the radius of the sphere-flat contact zone and G^* the effective shear modulus.[98] The magnitude of the radius a increases with increasing load (F_n) and tip radius (R) e.g. for the well known Hertz contact, $\pi a^2 = RE^*F_n$, where E^* is the effective Young's modulus. Thus $k_{contact}$ increases with increasing F_n and R, and a blunt AFM tip has $k_{contact} >> 100$ N/m at loads of ~10 nN.[58] The value of k_{tip} can be found using finite element modelling of the tip apex and results show that k_{tip}=39-84 N/m for sharp silicon tips ($R \approx 10$ nm) and k_{tip}=100-250 N/m for blunter tips ($R \approx 50$ nm).[58,75] Blunt tips could also be purposely constructed e.g. by attachment of a colloid bead on the tip apex.[99]

A second consideration is sensitivity. Equation 5.5 shows that for a given lateral force we desire Δx to be as large as possible before slip occurs to achieve maximum photodiode signal $h.\tan(\theta/2)$. Hence, $k_{eff} \approx k_{xT}$ should be as small as possible. For a rectangular cantilever of width w, length L, and thickness t, [100]

$$k_{xT} = \frac{Gwt^3}{4Lh^2}$$ (5.8a)

$$k_x = \frac{Ew^3t}{4L^3}$$ (5.8b)

$$k_z = \frac{Ewt^3}{4L^3}$$ (5.8c)

and k_z is the cantilever stiffness in the normal (z) direction. Table 5.1 lists some calculated values for commercially available cantilevers labelled as number no.1-4. The torsion sensitivity is improved (k_{xT} small) with thinner cantilevers and with longer tips. Extra tall tips (No. 4 in Table 5.1), although not available for our study, seem particularly promising as good torsion sensitivity can be achieved whilst maintaining k_z reasonably high (k_z=7 N/m) for high force loading. Of particular interest are colloid beads attached

to the tip apex.[101] Not only do colloid bead tips remove the problem of low tip stiffness, as noted above[99], but a large diameter bead (e.g. ~50μm or greater) can effectively provide a tall tip to enhance sensitivity for stiff non-contact cantilevers.

Table 5.1 The spring constants k_z, k_x and k_{xT} calculated for several commercial rectangular Silicon cantilevers and one triangular Si_3N_4 cantilever. Eq. 5.8 is used with E=169 GPa and G=60 GPa for the rectangular cantilevers. The analytical method of Sader is used for the Si_3N_4 triangular cantilever with E=150 GPa and G=50 GPa. All cantilever dimensions (L, w, t, h) are in micrometres and spring constants in N/m.

no.	Cantilever type	k_Z	k_X	k_{xT}
1	Nanosensors PPP-NCCR-50 Silicon tapping mode,			
	L=225; w=38; t=5.75 (measured thickness); h=12.5	26.8	1170	4109
2	Olympus OMCL-RC800PSA-1 Si_3N_4 contact mode			
	L=100; W=40; t=0.8; h=2.9	0.87	2163	487
	L=200; W=40; t=0.8; h=2.9	0.11	270	243
3	Budget Sensors triangular Si_3N_4 contact mode			
	L=100; w=2x16; t=0.52 ; h=12	0.27	740	7.3
4	Nanosensors Silicon extra tall tips,			
	SD-PXL-FM L=225; w=70; t=3; h=50	7	3817	67
	SD-PXL-CON L=225; w=60; t=1; h=50	0.22	801	2.1

Cantilevers no. 1 and 2 in Table 5.1 highlight an additional problem noted by Sader and Green[102] for rectangular cantilevers of larger length/width ratio, namely that for standard friction force AFM analysis it is assumed $k_{eff} \approx k_{xT}$ and $k_{xT}/k_X << 1$. This is clearly not the case for cantilever no. 1 and marginal for cantilever no. 2. The problem arises because the optical lever arm based detection in AFM is very sensitive to angular deflections of the cantilever (such as the torsion deflection corresponding to k_{xT}) but considerably less sensitive to pure linear displacement (such as the in-plane deflection corresponding to k_x).[101] For triangular levers (e.g. cantilever no. 3) the issue is not important because k_{xT}/k_X is always <<1.[102]

The results for cantilever no. 1 (Figure 5.5 below) are therefore only used to show the *qualitative* change in the friction force at high load, as these were the only high stiffness levers available, and the friction force is estimated from Eqn.5.5 using an effective spring

constant of $k_{eff}=(k_x^{-1}+k_{xT}^{-1})^{-1}= 910$ N/m. For future investigation at loads in the micro-Newton range it is recommended that stiff cantilevers with extra tall tips or colloid bead tips are used.

5.3 Experimental Demonstration

To demonstrate the method experimentally, a home built AFM was used (Section 3.2.3). Movement of the cantilever (which is equivalent to movement of the tip) relative to the sled can be easily observed from the relative movement between the edge of the plate and the cantilever chip holder. Surface imperfections and scattering can also be used to observe the relative motion of both the sled-cantilever and sled-substrate movement. Also note that the camera image quality from the home built AFM can be rather poor, depending on illumination and the type of substrate, and this limits the smallest detectable movement of the plate (resolution of ~3.4 μm). A modern commercial AFM has much superior optical microscopes installed and the method can thus be greatly improved in future implementations.

AFM cantilevers no. 1, 2 and 3 are used (see Table 5.1). The sleds are either 3 or 6μm thick, with 300μm side length. One face of the sled has three sharp tips approximately 3 μm high. When the sled is free standing on a surface, the tips touch the underlying substrate to form a three point contact. The opposite face of a sled was also studied when contacting a surface and is planar silicon or silicon with a sputtered thin gold film. The sleds are placed on two different substrate surfaces, either freshly cleaved mica or a smooth silicon surface with a fluorine terminated monolayer (F-Si) (see Section 3.4). The later (F-Si) surface is hydrophobic and is used in MEMS to decrease adhesion and liquid capillary formation[103].

(a) Sled moving   (b) AFM tip moving
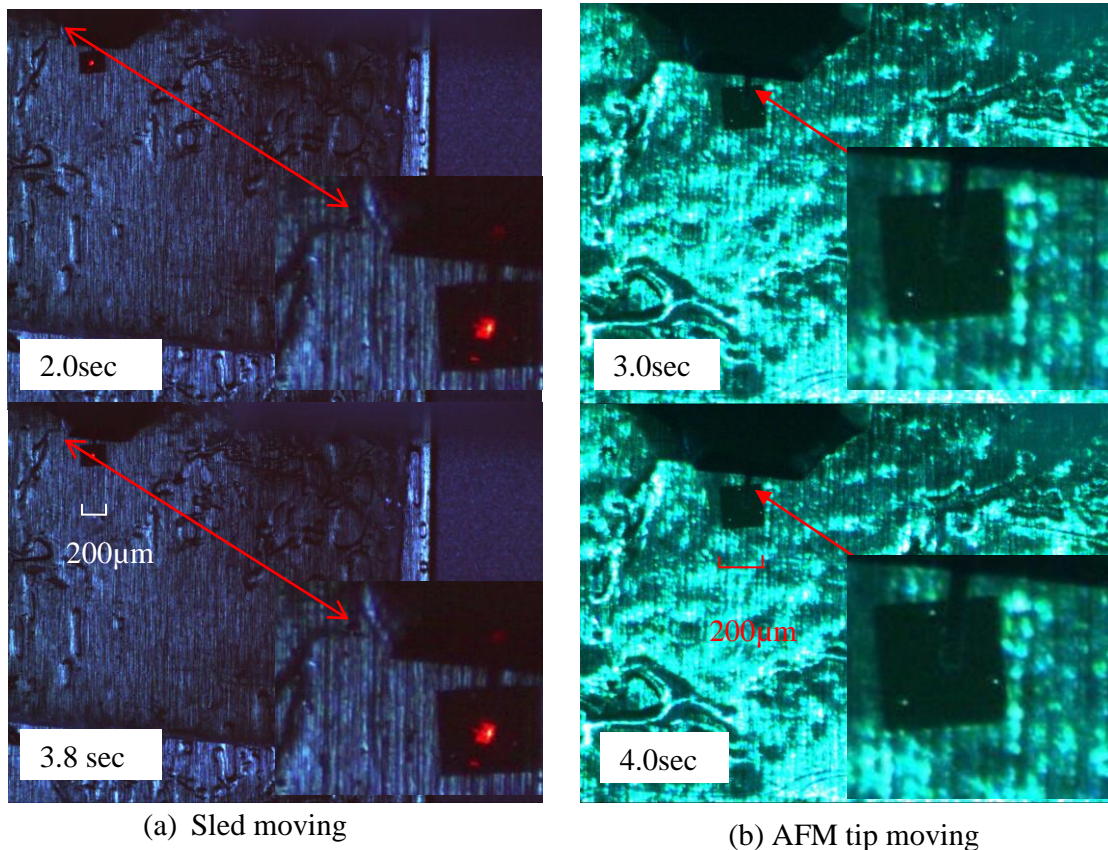
Figure 5.3 Movies from the AFM video camera are used to verify that (a) the sled is moving and (b) the AFM tip is moving under the applied lateral force. The photos are captured from movies 5.1 and 5.2. The movement is clearer in the inset.

Table 5.2 summarizes the different sled-substrate combinations studied, with the number S/N labeling the combination. For application of the method we require the sled to slide on the substrate before the AFM tip slides on the sled, which was only reproducibly achieved for the 3 sled tips on F-Si (S/N #1) and smooth Si on mica (S/N #4). The 3 sled tip on mica interface (S/N #2) was expected to be similar to the F-Si surface (S/N #1), and occasionally sled-substrate slip was indeed observed. However, on many occasions the AFM tip also slid over the sled surface during the experiments, and hence reliable measurement could not be achieved on this system and the slip condition is listed as "variable". Similarly, the flat, etched Silicon surface of the sled plate was expected to display similar behaviour when placed on either F-Si (S/N #6) or mica (S/N #4). However, on F-Si the plate-substrate interface did not move, even under vacuum conditions. The reason for this difference is unknown at present. The adhesion is

expected to be much stronger for the silicon-mica interface than the silicon-F-Si interface, the former surfaces being smooth and hydrophilic whilst the later interface is only slightly rougher but hydrophobic. Thus we anticipate the friction for both interfaces to be adhesion dominated at low load and hence Eqn. 5.4 suggests the plate does not move on the F-Si surface because the shear strength (τ_s) of the plate-F-Si interface is higher than the plate-mica interface. The high shear strength of the plate-substrate interface could also explain why plate-substrate sliding could not be initiated on contaminated F-Si surfaces (S/N #3) and Au coated surfaces (S/N # 5).

Table 5.2 A summary of the experiments for different sled-substrate combinations undertaken (denoted by the S/N number) showing the conditions under which either the sled-substrate contact slips or the tip-sled contact slips, or both (listed as "variable"). For application of the method we require the sled-substrate to consistently slip, which was only achieved for S/N #1 and S/N #4. Note that the table is not inclusive and simply indicates generalisations. For example, for the low friction interface of Fluorine-terminated Silicon (F-Si) and a 3 tip contact (S/N #1), the sled will not move if the F-Si surface becomes contaminated.

S/N	sled-substrate interface	The interface which slips	Lever no.	Environment
#1	3-sled-tips on F-Silicon	Sled-substrate	3	Ambient
#2	3-sled-tips on mica	Variable	2, 3	Ambient
#3	3-sled-tips on F-Silicon contaminated by C_8H_{18} residues	Tip-sled	3	Ambient or vacuum
#4	Flat sled face on mica; The sled surface is smooth Silicon after a 5 min vapor etch using 49% HF	Sled-substrate	1	Ambient
#5	Flat sled face on F-Silicon; The sled surface is thin film Au	Tip-sled	3	Ambient or vacuum
#6	Flat sled face on F-Si; The sled surface is slightly rough SiO_2 after a 80 min vapor etch using 49% HF:DI mixture (1:1 ratio)	Tip-sled	3	Ambient or vacuum

In a typical experiment the AFM tip is placed on top of the sled and the AFM piezoelectric scanner is actuated with a triangular waveform in the lateral direction. The peak-peak waveform amplitude ranged from 1 μm to 13 μm with a frequency range of 0.1Hz to 5Hz. The twisting of the cantilever records the lateral force acting at the AFM

tip apex and Figure 5.4 shows raw data of the lateral signal for a stiff cantilever (no.1) on a sled (S/N #4 in Table 5.2). Optical observation shows the sled moves with the cantilever, and hence the measured friction relates to the sled–substrate interface. The square wave shape is typical of a friction loop in AFM, with the amplitude being proportional to the dynamic friction force as the sample slides over the surface.[104] Figure 5.4 shows the square wave amplitude increases as the normal force increases, and this is again typical of AFM friction measurements at high load and is simply a reflection of Eqn. 5.1 ($F_f = \mu F_n$).
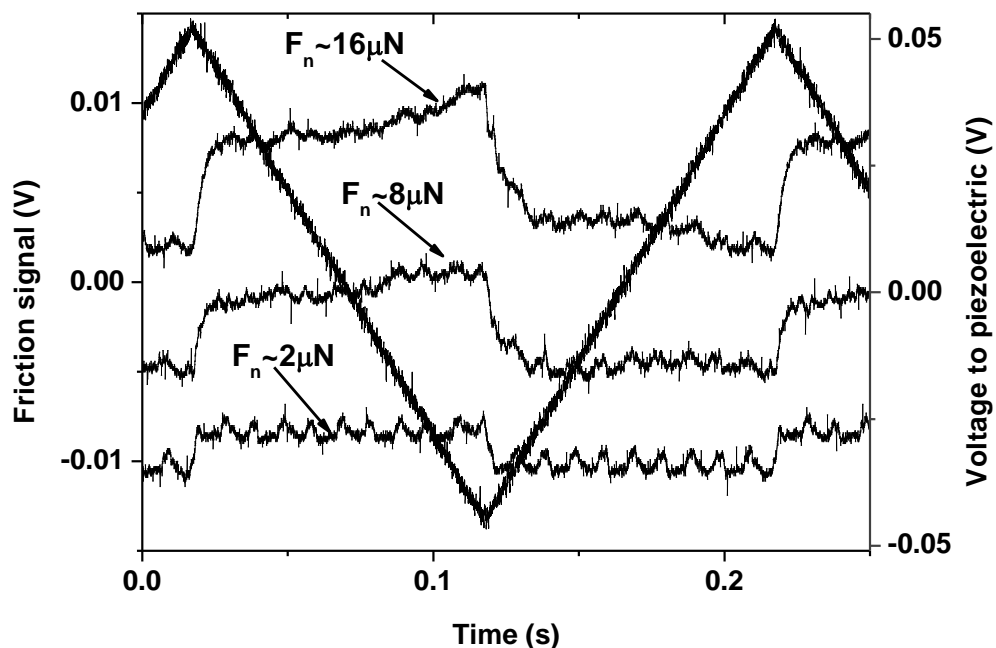
Figure 5.4 Oscilloscope traces showing the raw friction signal (i.e. the PSD signal corresponding to the twisting of the AFM cantilever) at three different applied loads (approximately 2, 8 and 16 μN). The triangular waveform (5Hz, 100mV$_{p-p}$) is the voltage driving the displacement of the AFM piezoelectric scanner. The peak-peak piezoelectric voltage corresponds to a displacement of 670 nm, giving a displacement speed of 3.35 μm/s. The friction signal changes to a new steady state value when the displacement changes direction and half the difference between the two steady state values is the dynamic friction force (F_f).

Rather than measure individual waveforms on an oscilloscope, such as Figure 5.4, we continuously monitor the peak-peak height of the lateral force signal by inputting the

signal into a lockin amplifier (EG&G Instruments 7260). In this way continuous force curves can be obtained[59] in which the friction force is measured as a function of the load, as shown in Figure 5.5.

The normal load is simply found as $F_n = k_z \Delta z$, where Δz is the deflection of the cantilever in the normal direction.[93] The magnitude of the lockin amplifier signal is converted into the friction force as follows.[58,75] Let I_1 and I_2 be opposing currents generated by the laser spot on the quadrant PSD. The lateral position of the spot (p) on the PSD is,

$$p = \frac{I_1 - I_2}{I_1 + I_2} \cdot \frac{l}{2} \tag{5.9}$$

where l is the width of the PSD (l=4 mm, DLS-4 UDT Sensors). A deflection of the cantilever by an angle θ changes the laser spot location by Δp, and since the distance (S) between the cantilever and the PSD is always much larger than Δp (S=20 mm in our AFM) we can write,

$$\theta = \Delta p / S \tag{5.10}$$

The calculated values of θ, taking into account any gain factors, are inserted into Eqn. 5.5 to give the friction force. Note that the dynamic friction is half the peak-peak value of the input square wave.[104] Most lockin amplifiers will provide the root-mean-square (rms) value as the output. Therefore for a square wave the rms output is already half the peak-peak value and no further correction is required to account for this aspect in the friction force conversion, provided the input signal remains a square wave. The lockin technique is not robust if large additional waveform features are present e.g. from topography effects as the surfaces slide over each other.

5.4 Results and Discussion

5.4.1 Flat surface side (non-tip) touching the substrate

Figure 5.5 shows the friction of a flat Silicon surface sliding at relatively high loads (micro-Newton) on mica (S/N #4 in Table 5.2) using a stiff cantilever (no.1). Recall that for this cantilever the results are only qualitative because the effective spring constant is very uncertain.
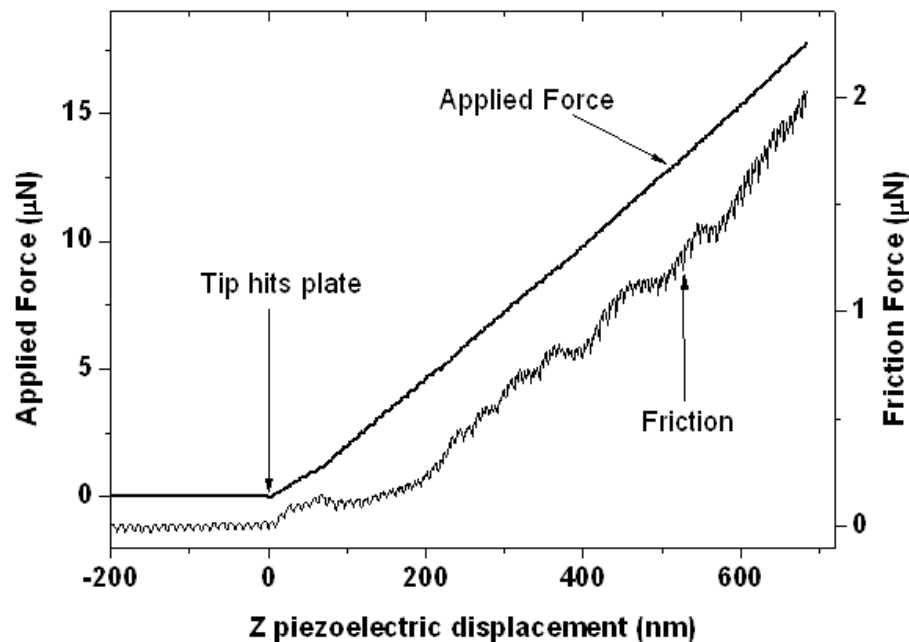
Figure 5.5 A force curve i.e. force as a function of piezoelectric displacement in the normal (z) direction, showing the change in friction as a function of the applied load. In this experiment the flat face (i.e. smooth Si; no tips) of a square sled (300x300 μm^2, 3 μm thick) contacts a mica surface. The AFM tip approaches the sled surface from negative z values and contacts the sled at z=0 nm. Positive z values correspond to the AFM tip being in contact with the sled. At positive z values, the sled is observed (optically) to move with the cantilever, verifying that the measured friction relates to the sliding of the sled and not the AFM tip. The sled moves linearly with speed 0.33 $\mu m/s$ and the experiment is undertaken in ambient atmosphere. The AFM cantilever has calculated spring constants of k_z=26.8 N/m and k_{xT}=4109 N/m.

5.4.2 Tip side touching the substrate

Figure 5.6 demonstrates the method at much lower load (nano-Newton) and shows the friction of a sled sliding with the 3 plate tips in contact with a F-Si surface (S/N #1 in Table 5.2). A more sensitive cantilever is used for low force measurement (no.3).
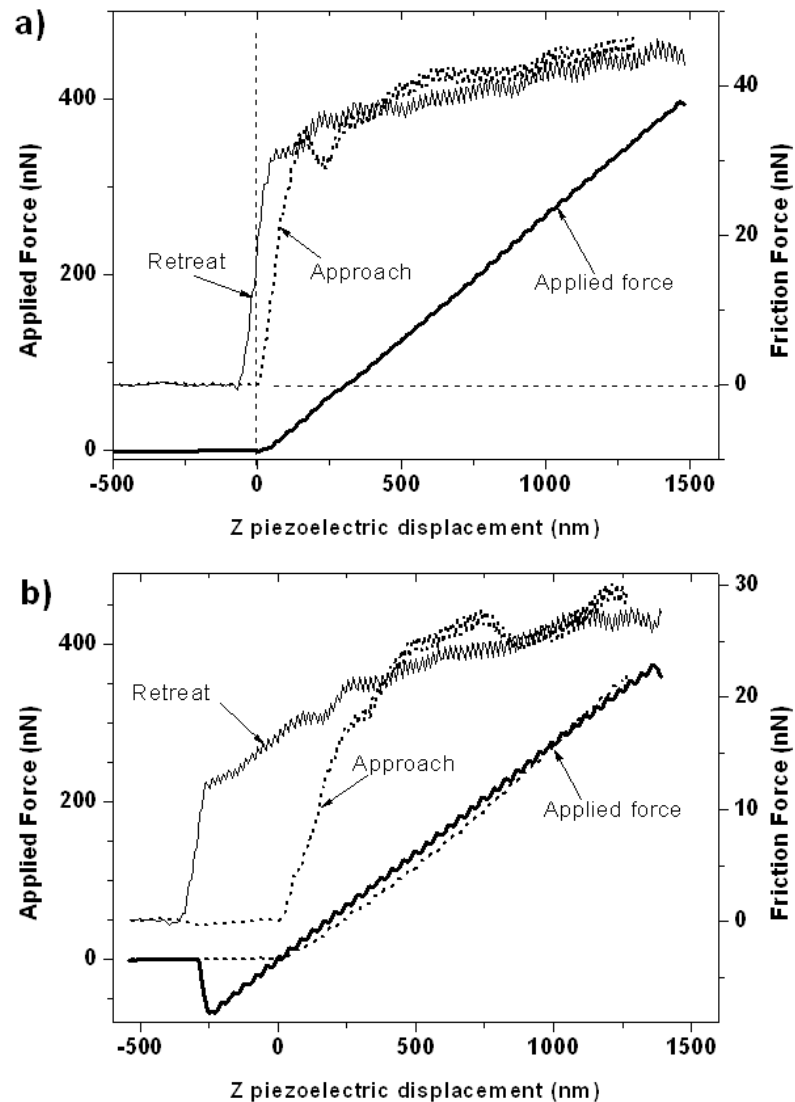
Figure 5.6 Approach (dashed line) and retreat (solid line) force curves as a function of piezoelectric displacement in the normal (z) direction, showing, a) negligible adhesion at the AFM tip-sled contact, and b) strong adhesion at the AFM tip-sled contact. The AFM tip approaches the sled surface from negative z values and contacts the sled at z=0 nm. At positive z values, the sled is observed (optically) to be moving with the cantilever, verifying that the measured friction relates to the sliding of the sled and not the AFM tip. In this experiment the 3 sled tips of a square sled (300x300 μm^2, 6 μm thick) contact a Fluorine-terminated Silicon surface. The sled moves linearly with speed 9.5 μm/s and the experiment is undertaken in ambient atmosphere. The AFM cantilever has calculated spring constants of k_z=0.27 N/m and k_{xT}=7.3 N/m.

An interesting aspect is that different adhesion is observed in Figure 5.6a and Figure 5.6b and arises because the AFM tip is at different locations on the sled Thus, in this example, the adhesion is related to the tip-sled contact and for the sled-substrate interface we can only state the adhesion is greater than ~70nN. In order to measure the sled-substrate adhesion minima requires a stronger bonding of the AFM tip to the sled e.g. by gluing.

Figure 5.6 shows that friction forces can be measured in the adhesive load region and the non-linear variation of friction with force is consistent with a) adhesion dominated friction, and b) only a few asperities (3 in this case) being in contact. To briefly outline these aspects we consider the simplest single asperity model incorporating adhesion, namely the Derjaguin-Muller-Toporov (DMT) model for an elastic sphere (radius R) contacting a flat,[105] in which,

$$F_n = \frac{4}{3} E^* R^{1/2} \delta^{3/2} - 2\pi R \gamma \tag{5.11}$$

$$A = \pi R \delta \tag{5.12}$$

where γ is the surface energy and δ is the indentation depth. For adhesion dominated friction $F_f = \tau$ A (Eqn. 5.3), leading to the relation $F_f \sim F_n^{2/3}$ [96] within the single asperity DMT model and a non-linear variation of friction with load. An alternative means to highlight this aspect is to plot the friction coefficient $\mu = F_f/F_n$, as shown in Figure 5.7. For adhesion dominated friction the DMT model leads to the relation $\mu \sim F_n^{-1/3}$ and Figure 5.7a shows the data at low load follows the general trend of decreasing μ with increasing load. The friction measured over a larger load range (Figure 5.7b) shows the friction coefficient at first decreasing and then reaching a plateau of $\mu \approx 0.09$ for loads great than ~7μN, consistent with a transition from adhesion dominated friction at low load to force dominated friction at high load (see Eqn. 5.3). These results suggest the technique can be useful to study macroscopic interfaces at low load and how friction

evolves from few asperity contacts to multiasperity contact,[79,106-109] and from adhesive

dominated friction to load dominated friction.[81]
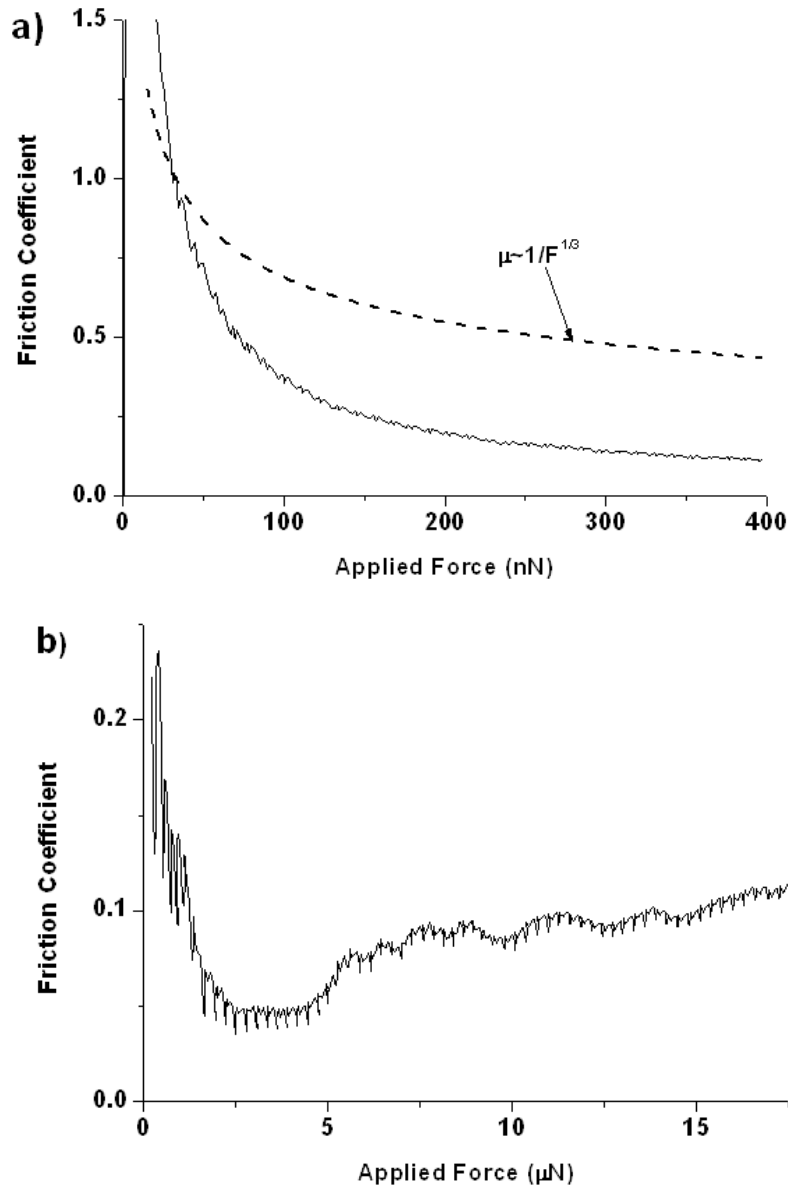
Figure 5.7 The calculated friction coefficient ($\mu_s = F_f/F_n$) of the sled-substrate contact as a function of load. a) Low load data corresponding to Figure 5.6a. Data taken in ambient on a square sled (300x300 μm^2, 6 μm thick) with the 3 sled tips in contact with a F-Si surface, and using an AFM cantilever with calculated spring constants of $k_z=0.27$ N/m and $k_{xT}=7.3$ N/m. The sled moves linearly with speed 9.5 $\mu m/s$. The dashed line shows the theoretical single asperity relationship $\mu \sim F_n^{-1/3}$. b) High load data corresponding to Figure 5.5. Data taken in ambient on a square sled (300x300 μm^2, 3 μm thick) with the flat face (i.e. smooth Si; no tips) of the sled in contact with a mica surface, and using an AFM cantilever with calculated spring constants of $k_z=26.8$ N/m and $k_{xT}=4109$ N/m. The sled moves linearly with speed 0.33 $\mu m/s$.

The present data is too preliminary to justify incorporating more complex modelling[59,105-110] of multi-asperity roughness, capillary condensation and adhesion. Specifically, the data of Figure 5.5 and Figure 5.6 are taken on different sled-substrate interfaces, the adhesion minima of the sled-substrate interface has not been measured, and the surface roughness of the sled is unknown. These issues need to be addressed in future studies.

5.4.3 Technique problems

Figure 5.8 and Figure 5.9 highlight two technical problems to address. In addition to pure translation, as assumed in the above analysis, rotation of the plate can also occur. The lateral force components at the sled-substrate interface change for rotational motion because the applied lateral force is not parallel to the direction of sled motion. Figure 5.8 shows friction data measured in three separate approach force curves in the same experiment in which the sled moves over the surface by translation (Curve A), with a small rotational "jiggle" superimposed on the lateral translation (Curve B), and with a large rotational motion observed (Curve C). The large step in Curve C shows the sled has rotated and then become locked into a state of higher friction during the force curve acquisition. This conjecture is reasonable given that the sled used in Figure 5.8 has 3 sharp tips contacting the substrate, and if one tip experiences higher friction force than the other two tips (e.g. one plate tip is blunt, or one sled tip encounters a surface defect) rotation is promoted until all the sled tips slip in translation. However, Curve B shows that distinct steps in a force curve are not a necessary signature of rotation; rotation can be present even if the friction curve only changes monotonically with load. In this regard, the experimental observation of sled rotation is limited by the resolution of the optics.
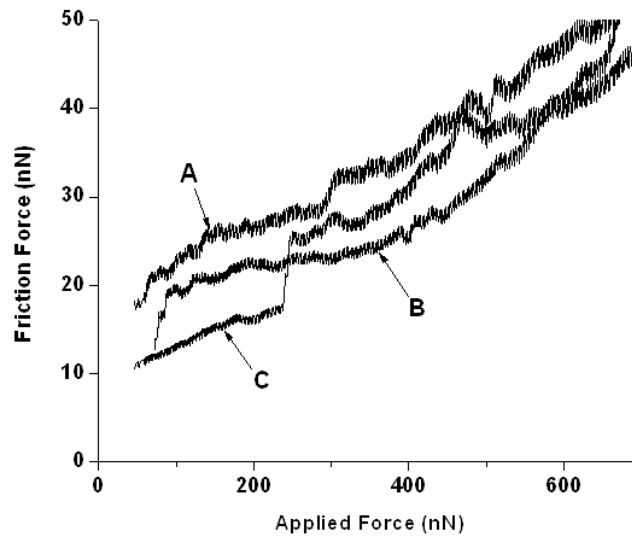
Figure 5.8 Approach force curves showing qualitative effects of sled rotation during data acquisition. Observation shows the measured friction relates to the sliding of the sled and not the AFM tip. Curve A) the sled moves linearly. Curve B) some rotational jiggle is observed superimposed on the linear movement of the sled. Curve C) a large rotational movement occurred during data acquisition giving a step jump in the friction force. In this experiment the 3 tips of a square sled ($300 \times 300 \ \mu m^2$, 6 μm thick) contact a F-Si surface in ambient atmosphere. The AFM cantilever has calculated spring constants of $k_z = 0.27$ N/m and $k_{xT} = 7.3$ N/m.

Finally, if many asperities are in contact at the plate-substrate interface, the force F_n is distributed across the entire interface, as implicitly assumed above in deriving Eqn. 5.2. However, at low load (nano-Newton range) very few asperities may be in contact, even if the surfaces are rough.[79,90,111]

In our experiments the sample plates (sleds) are specially constructed such that on one face of the plate only 3 tip asperities contact the substrate. In cases having very few asperities in contact, the loading of each asperity depends on the location of the normal force applied by the AFM tip. In turn, the different loading of each asperity may critically influence the friction force at the asperity and hence the lateral motion of the plate. Figure 5.9a shows schematically the loading of a plate having three tips located at

(x_1, y_1), (x_2, y_2), and (x_3, y_3), and a normal force P acting at the location (x_0, y_0). The reaction forces F_1, F_2 and F_3 of the 3 plate tips can be written,

$$F_1 = \frac{(y_3-y_0)(x_3-x_2)-(y_3-y_2)(x_3-x_0)}{(y_3-y_2)(x_3-x_1)-(y_3-y_1)(x_3-x_2)} \, P \qquad (5.13a)$$

$$F_2 = \frac{(y_3-y_0)(x_3-x_1)-(y_3-y_1)(x_3-x_0)}{(y_3-y_1)(x_3-x_2)-(y_3-y_2)(x_3-x_1)} \, P \qquad (5.13b)$$

$$F_3 = \frac{(y_2-y_1)(x_1-x_0)-(y_1-y_0)(x_2-x_1)}{(y_2-y_1)(x_3-x_1)-(y_3-y_1)(x_2-x_1)} \, P \qquad (5.13c)$$

Equation 5.13 shows that in general the force acting on each plate tip is not the same, although special cases can be constructed. For example, if the 3 plate tips are placed equidistantly on a circle and the normal force acts in the centre of the circle, as shown in Figure 5.9b, the reaction forces of the 3 plate tips are equal,

$$F_1 = F_2 = F_3 = -\frac{1}{3} \, P \qquad (5.14)$$
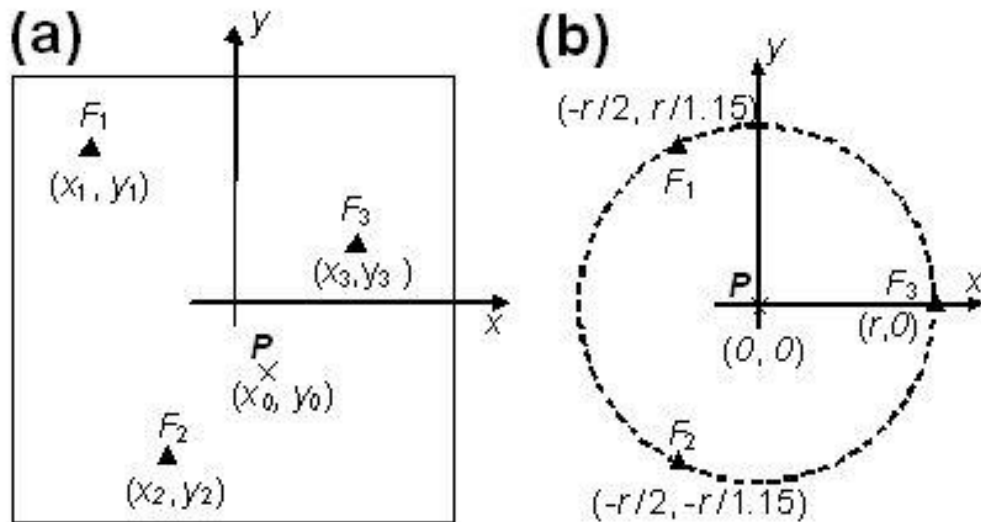
Figure 5.9 Schematics showing the loading of 3 tips (▲) of a plate by a point force applied at position $P(x_o, y_o)$. The force on each plate tip (F_1, F_2, F_3) depends on the location at which the AFM tip exerts the load. a) In the general case, the force on each plate tip is not equal. b) A special case occurs if the AFM tip applies the force equidistant between the 3 plate tips, giving an equal load on each plate tip.

Thus, it may be important to understand the load distribution in cases involving a few asperities in contact e.g. for plates in contact at ultra-low load.[79,107]

5.5 Conclusion

In conclusion, we have introduced and demonstrated a method to measure friction on a small, microfabricated sled by controllably bringing an AFM tip onto the structure. The measurement principle has been demonstrated, but considerable refinement is required to produce reliable instrumentation as there remain many technical issues. For example, the effects of sled-substrate velocity and loading position may influence the measured friction force and need to be further evaluated; often the AFM tip moves across the sled before plate motion occurs; rotation of the sled can be observed, suggesting local regions of the sled-substrate contact experience much higher frictional force; if very few asperities are in contact at the plate-substrate interface, the force acting on each asperity depends on where the AFM tip load is applied, which must also yield different friction forces acting at the asperity.

Engineering solutions are possible for all these concerns. Sample rotation can be monitored optically at high resolution and corrected by suitable analytical modelling. Note that at a fundamental level there is no difference between using low or high resolution optics. Provided one can visualize the relative motion of the sliding bodies one can apply the method to measure the dynamic friction. What is greatly helped by improved or high resolution optics is at the practical level. Not only are the relative motions easier to observe, but smaller rotational movements would be resolved leading to improved correction analysis, and smaller scan sizes could be used, leading to weaker topography effects coupling into the friction signal. For dry sliding conditions, using an AFM combined with a scanning electron microscope (SEM) would be advantageous.[112]

The problem of slipping of the AFM tip could be arrested by a tacky or very rough tip-plate contact, or perhaps using special AFM tips. In this regard the use of colloid probe tips could be particularly important as the technology offers the advantages of decreasing the tip compliance, enhancing friction sensitivity through a large effective tip height, and increasing the tip-plate contact area to promote adhesion and make sliding more difficult at low load. Stronger tip-plate adhesion may also allow the important adhesion minima data of the plate-substrate interface to be measured. The difficultly of accounting for localised plate load when few asperities contact could in principle be overcome by optically monitoring the relative position of the AFM tip and using this information to amend the calculated friction forces. However, such an approach would not be viable for a randomly distributed asperity contact.

Notwithstanding the technical issues, we believe the approach has general application to measuring friction on small, free standing objects. For example, experiments also showed the ability to place the AFM tip onto small samples of Aluminium foil and paper on mica, and subsequently to move the samples laterally (data not shown). Further. the method bridges the nano-Newton to micro-Newton force range for tribology studies and allows low load measurement of macroscopic structures e.g. microfabricated plates. Our preliminary results suggest these attributes enable the technique to study interesting tribology questions, such as the evolution of friction from few asperity, adhesive dominated sliding to multiasperity, load dominated friction.

Chapter 6 Testing of Sleds

6.1 Introduction

This chapter presents experimental results for the vibration and actuation of thick sleds. Only selected data is shown to highlight particular aspects as the amount data collected is large. Vibrometer results on ultrathin sleds are not presented because the data is not convincing, the mode shapes are not easily observed and the noise levels from the substrate signal are relatively high because not much light is scattered back from the sled.

Section 6.2 presents vibrometer spectrums and mode shapes for circular and square sleds still attached to the process chip by spring legs. The results are compared to the FEM simulations of Chapter 4 with particular emphasis on the free sled modes because these modes act as a reference within the multitude of observed modes. Section 6.3 is similar but shows data for sleds which have been placed on a surface.

The actuation of sled movement across a surface proved to be difficult to achieve in any consistent manner, and section 6.4 shows and discusses our results to date. Actuation data for sleds on mica, FDTS coated silicon (F-Si), and graphite are summarized. The magnetic actuation proved too weak to move the sleds, thus all results showing significant sled movement were taken using PZT actuation. Video movies of sled motion are available in the supplementary materials.

For ease of reading, we label the sleds discussed as follows.

 Sleds for PZT actuation across a surface : These circular sleds are labelled the C series.

C1, 300 μm diameter, 3.3 μm thick, used on mica.

C2, 300 μm diameter, 3.3 μm thick, 30μm magnetic particle, used on mica.

C3, 300 μm diameter, 3.3 μm thick, 10nm gold on back side, used on F-Si.

C4, 300 μm diameter, 3.3 μm thick, 10nm gold on back side , used on graphite.

C5, 300 μm diameter, ~4 μm thick, 10nm gold on back side, used on F-Si.

Sleds for magnetic actuation in vibrometer studies : These sleds labelled as the D series.

D1, 300 μm diameter, 3.3 μm thick, ~60μm magnetic particle.

D2, 300 μm diameter, 3.3 μm thick, ~60μm magnetic particle.

D3, 300 μm diameter, 3.3 μm thick, ~80μm magnetic particle, one tip blunt.

D4, 300 μm diameter, 4 μm thick, ~60μm magnetic particle, 4nm gold on back side.

D5, 300 μm square, 4 μm thick, 40μm magnetic particle.

D6, 300 μm square, 4 μm thick, 70μm magnetic particle.

6.2 Vibration of sled attached to the chip

6.2.1 Vibrometer results: Circular sleds with magnetic actuation

The sleds D1 to D4 are characterized with the particles magnetized at 1.4 T. Firstly, the spectrum is taken. The PSV laser spot is focused at different locations on the sled and the PSV output recorded as the frequency is swept (Figure 6.1). Vibration resonance frequencies are observed and the actuation driving voltage can be increased, to raise the resonance peaks above the noise floor, or decreased, to prevent signal clipping e.g. Figure 6.1 compares spectra for 2V and 20V solenoid drive voltage. The spectra can be compared at different locations (e.g. Figure 6.1 compares the centre of the sled with one

of the tips) but it is much more useful to simply use the spectra to find a resonance frequency (f_o) and then map the mode shape over the entire sled, as shown below. The spectra taken at different locations are entirely consistent with the mode shape results (data not shown) but the amplitude of the spectrum data can vary greatly depending on the quality of the backscattered laser signal at a specific location. Mapping the mode shape is also faster and ultimately provides easier interpretation.
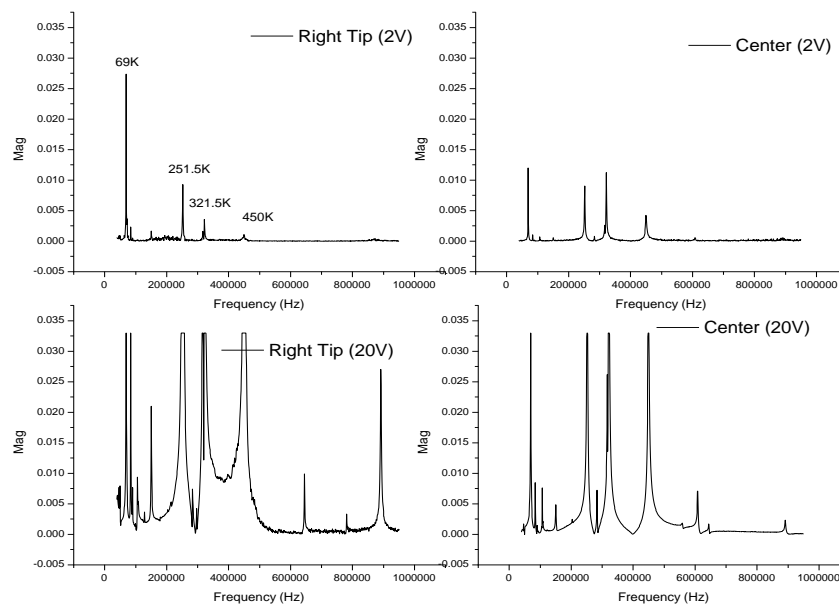
Figure 6.1 Frequency spectra of sled D1. Drive voltages of 2V $_{pk-pk}$ (Top) and 20V $_{pk-pk}$ (Bottom) are compared over the centre (right) and a tip (left) region.

Tables 6.1 and 6.2 show the mode shapes measured for sleds D4 and D1, respectively. The images are snapshots at the phase of the oscillation where the maximum (red) and minimum (green) occur. Note that the color scheme for the PSV is limited and the colour red (or green) will be assigned for the maximum (or minimum) irrespective of the real amplitude of the oscillation. Therefore, to compare the magnitude of the different modes, the value of the oscillation amplitude range is also shown.

In mode shape acquisition, specific areas of the surface can be localized for measurement and Table 6.1 shows two groups of images. The first group (labelled "sled") shows only the area of the sled plate. The second group (labelled "sled and chip") shows a larger area including the sled surroundings. This feature is useful because the vibrometer measurement at each individual point is surface related. If strong scattering occurs near the legs or edge of the sled then false displacement contrast in the mode image may be produced. Typically a false image can be generated if the maximum displacement of the sled is less than ±70pm.

Table 6.1 List of the first 11 *measured* experimental modes, in sequence of increasing resonance frequency (f_o in kHz), for the sled D4 (300μm diameter, 3.9μm thick) still connected to the chip. The voltage used to drive the actuation and the maximum measured amplitude range is shown. The data labeled "sled" shows measurement defined only over the sled, whereas the "sled and chip" data shows a measurement area over the sled and surrounding chip. The label "mode" is the mode number for the corresponding FEM *simulation* for a circular sled (Figure 4.17) with 2 legs and an attached off-centre particle, with the calculated f_o in kHz shown in red. The legs are perpendicular in the vertical direction.
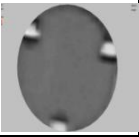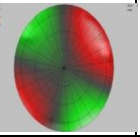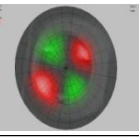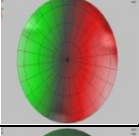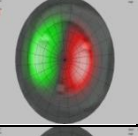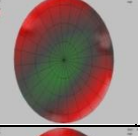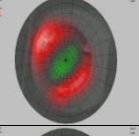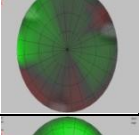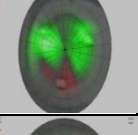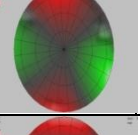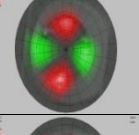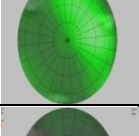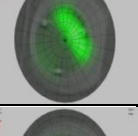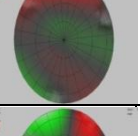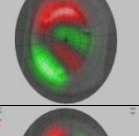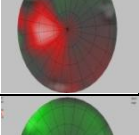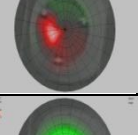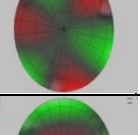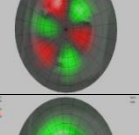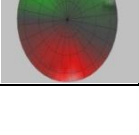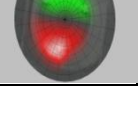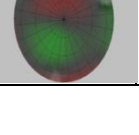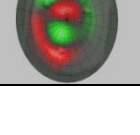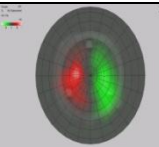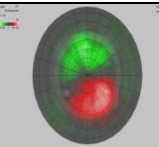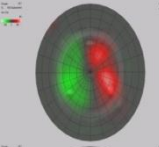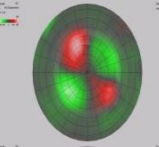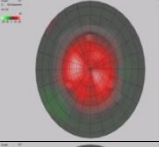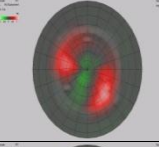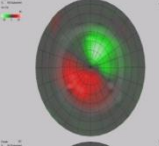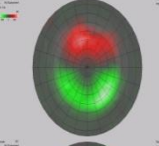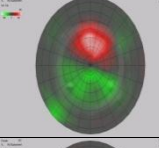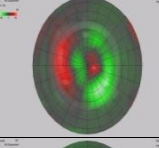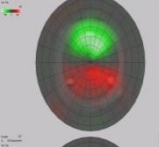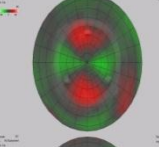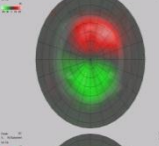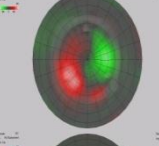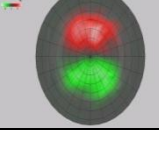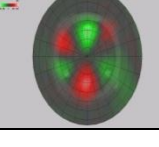
FEM f_o kHz [mode]	f_o (kHz) (Volts) Range	Sled	Sled and chip	FEM f_o kHz [mode]	f_o (kHz) (Volts) Range	Sled	Sled and chip
				f_o=408 [5] 1st free	370 (10V) ±1nm		
[1]	3.4 (2V) ±24nm			f_o=394 [4] 2nd free	396 (10V) ±600pm		
not in FEM	22 (2V) ±4nm			f_o=594 [6]	445 (10V) ±600pm		
not in FEM	33 (2V) ±12nm			not in FEM	582 (10V) ±700pm		
not in FEM	48 (2V) ±1.4nm			f_o=879 [7] 3rd free	772 (10V) ±300pm		
f_o=264 [3]	101 (2V) ±50nm			not in FEM	932 (10V) ±700pm		

Table 6.2 List of the first 16 *measured* experimental modes, in sequence of increasing resonance frequency (f_o in kHz), for the sled D1 (300μm diameter, 3.3μm thick) still connected to the chip. The voltage used to drive the actuation and the maximum measured amplitude range is shown. The data labeled "sled and chip" shows a measurement area over the sled and surrounding chip. The label "mode" is the mode number for the corresponding FEM *simulation* for a circular sled (Figure 4.17) with 2 legs and an attached off-centre particle, with the calculated f_o in kHz shown in red. The legs are perpendicular in the vertical direction.

FEM mode	FEM f_o (kHz)	f_o (kHz) (Volts) Range	Sled and chip	FEM mode	FEM f_o (kHz)	f_o (kHz) (Volts) Range	Sled and chip
1	32	33.6 (2V) ±30nm		not in FEM		274 (9V) ±1.2nm	
2	56	50 (9V) ±600pm		5 1st free	345	319 (9V) ±2nm	
not in FEM		69 (9V) ±2nm		4 2nd free	333	324 (9V) ±3nm	
not in FEM		83 (9V) ±250pm		not in FEM		434 (9V) ±6 nm	
Similar to [3]		108 (9V) ±260pm		not in FEM		528 (9V) ±240pm	
Similar to [3]		144 (9V) ±240pm		6	503	610 (9V) ±120pm	
Similar to [3]		170 (9V) ±250pm		not in FEM		648 (9V) ±260pm	
Similar to [3]		251 (2V) ±7nm		8	805	905 (9V) ±600pm	

Tables 6.1 and 6.2 can be compared with corresponding FEM simulations (Figure 4.17) by matching the mode shapes. The resonance frequencies (f_o) of matching modes are also compared. The FEM frequencies are calculated based on the SEM measurement of the

sled thickness (3.3μm or 3.9μm). Note that we cannot compare the amplitude of the modes as this information is not available from the FEM modelling.

The first observation is that many additional experimental modes arise than predicted by the FEM modelling, particularly at low frequency. The additional peaks no doubt occur because real devices are not symmetric and defect free as in the simulated case. Nevertheless, many of the modes predicted by FEM are also observed in the experimental data. Although the mode details can be slightly different, overall the experimental and simulation mode shapes are comparable; the 2nd free plate mode (listed as mode 4) even shows a distortion along the leg direction as predicted for a sled with attached particle (Figure 4.17, mode 4). The predicted and experimental frequencies (f_o) are in reasonable agreement for the low modes (1st and 2nd free modes) but diverge considerably (by ~100 kHz or ~20%) for higher modes. The experimental data also confirms that the thicker sled (D4, Table 6.1) has higher sled resonances for the 1st and 2nd free plate modes compared to the thinner sled (D1, Table 6.2). However, we again observe this is not the case for higher modes. The reason for the divergence at high mode number is not known.

The frequency of the 2nd free mode (listed as mode 4 in Tables 6.1 and 6.2) does not fall below that of the 1st free mode (listed as mode 5), as predicted by FEM (Figure 4.17). However, this is simply because the details of the real particle added to the sled differ from the simulation. What is entirely satisfactory is the frequency of the 2nd free mode has dropped considerably compared to a sled with no particle (compare mode 2 in Figures 4.14 and 4.15); and this is the major point to note.

6.2.2 Vibrometer results: Square sleds with magnetic actuation

Table 6.3 shows mode shape measurements on a square sled (D6). In this example, the experiment matches the FEM simulation very well. The 3rd free mode shape (labeled mode 5) has lower frequency than the 2nd free mode shape (labeled mode 6) as predicted in FEM by the addition of the spring legs (Figure 4.12). The experimental frequency of the 3rd free mode (374 kHz) is lower than the predicted FEM value (461 kHz), but this is expected because this mode (and also mode 3) is strongly influenced by a particle located in the centre of the sled, which considerably lowers the frequency (Figure 4.15). The other sled modes have a node located in the central region and thus their experimental values of f_o are very close to the predicted FEM values, if the thickness is taken as 4.8μm. Using an improved value for the thickness of 4.8μm, as opposed to the SEM value of 4μm, is entirely reasonable given the uncertainty in determining sled thickness across the entire structure using SEM.

6.2.3 Factors influencing the PSV measurement

Inevitably, variance in sled fabrication will occur (e.g. changes of the leg dimensions in the lithography step, differences in sled thickness in the etching step) and influence the measured resonance modes. Device reproducibility is the key to minimize this uncertainty. It is also important in the fabrication to fully open / remove any material in the back side release hole underneath the sled plate and legs.

Spectra were also measured in vacuum and compared to similar ambient experiments. A typical quality factor (Q) for a resonance is Q ≈ 200 e.g. see Figure 6.1. The signal to noise level in vacuum is slightly better than in ambient but the improvement is very small. Therefore, for sleds still attached to the chip, it is preferable to simply undertake

experiments in ambient. The situation changes when a sled is placed on a surface because squeeze damping becomes significant (section 6.3.4).

Table 6.3. List of the first 8 *measured* experimental modes, in sequence of increasing resonance frequency (f_o), for the sled D6 (300 µm square, 4µm thick) still connected to the chip. The voltage used to drive the actuation is 9V for all data and the maximum measured amplitude range is shown. The measurement area is over the sled and surrounding chip. The label "mode" is the mode number for the corresponding FEM *simulation* for a square sled with 2 legs but no attached particle, with the FEM calculated values of f_o shown in red for two different sled thicknesses. The heavy line shown in mode [3] shows the leg orientation.

Mode	FEM mode shape	FEM f_o kHz t=4.0µm	FEM f_o kHz t=4.8µm	Measured f_o (kHz) Range	Measured mode shape
[3]		**183**	**220**	**87.8** ±24nm	
Similar to [3]				**105** ±4nm	
Similar to [3]				**125** ±800pm	
[4] 1st free		**254**	**305**	**300** ±2nm	
[5] 3rd free		**384**	**461**	**374** ±1.6nm	
[6] 2nd free		**466**	**561**	**549** ±1.2nm	
[8]		**643**	**772**	**732** ±4nm	

Magnetic actuation is sensitive to the particle magnetization direction and the particle size. The diameter of the magnetic particles tested varied from 30µm to 80µm. We found the

particle size must be ≥60μm and the particle magnetization field must be ≥1.0 T, and preferably ≥1.4 T, in order to generate a clear free mode shape. If either condition is not fulfilled, free mode shapes cannot be observed due to the small magnetic force exerted.
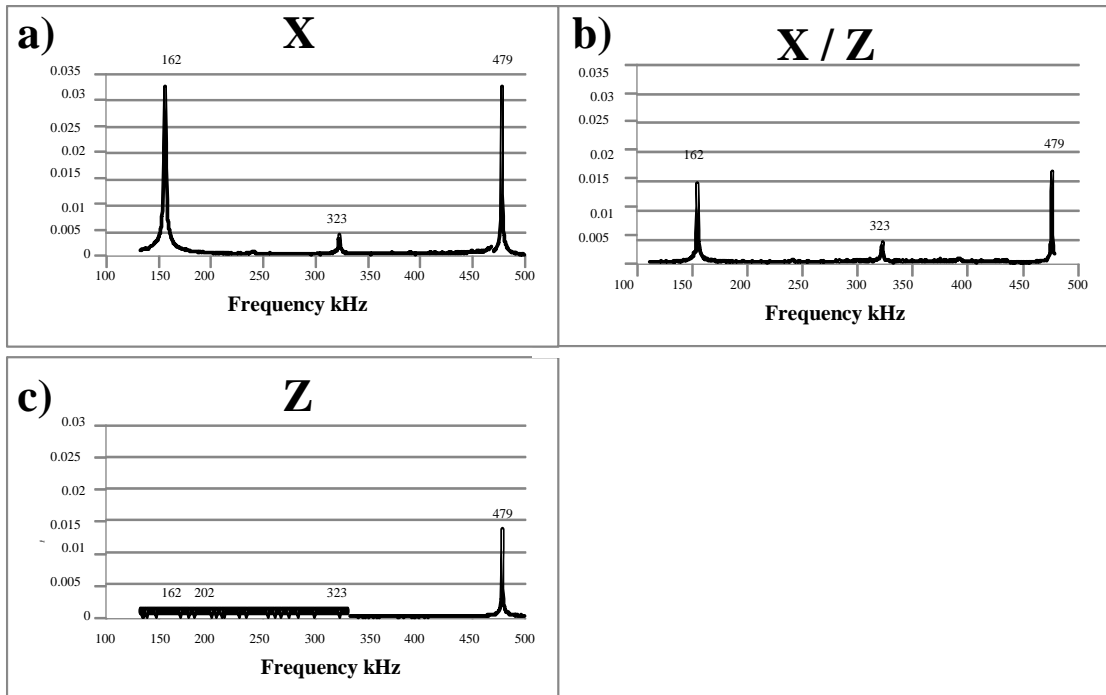
Figure 6.2 PSV spectra taken with a lockin amplifier on a square sled attached by 2 legs showing the effect of the particle magnetization direction on the resonances measured in the centre of the sled. a) The particle is magnetized along the plane of the sled (x direction). b) The particle is magnetized at 45° to the surface normal and the plane of the sled (x/z direction). c) The particle is magnetized in the surface normal direction (z).

Figure 6.2 gives a qualitative example of the influence of the particle magnetization direction. If the particle is magnetized in a direction normal to the sled surface (Figure 6.2c) the excitation of the resonances is much weaker compared to the case of the particle magnetized in the plane of the sled (Figure 6.2a); two lower resonance peaks (at 162 and 323 kHz) entirely disappear. An intermediate case is shown for the particle magnetized at 45° to the sled plane (Figure 6.2b). These observations follow because the strongest magnetic force is generated for particle magnetization in the plane of the sled, which creates a torque perpendicular to the sled plate.

6.2.4 PSV measurement using PZT actuation

Magnetic actuation was used extensively in PSV characterization because PZT actuation of the sled proved difficult to interpret. Figure 6.3 shows an example of spectra measured at different locations on a 300 μm diameter, ~ 4μm thickness sled (D4) with PZT actuation. There is a large noise peak from the substrate at around 230 kHz but the other peaks (labeled a-e) are related to the sled. The frequency of all the peaks is less than 300 kHz. From the FEM simulation, the free plate modes of a ~4μm thick, 300μm diameter sled are above ~300 kHz. Thus it appears all the peaks of Figure 6.3 are related to the modes of the spring leg, not to the free plate modes.
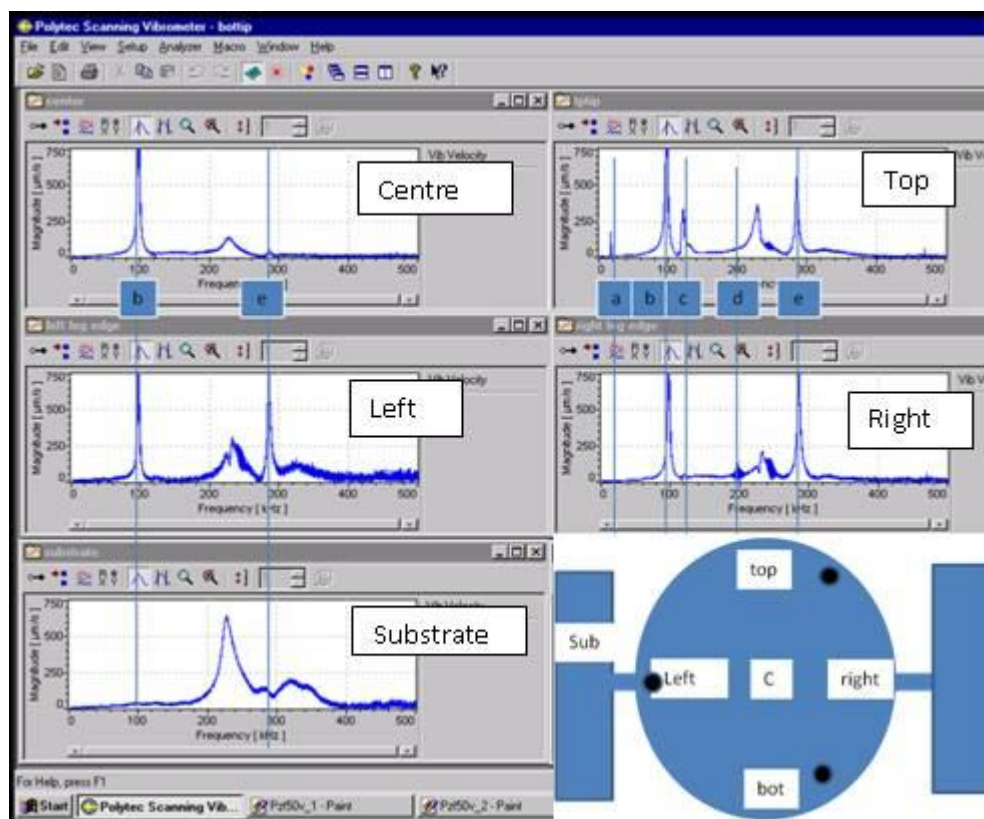
Figure 6.3 Frequency spectra measured using PZT actuation (50V) for a ~4 μm thick, 300μm diameter circular sled (D4). The measurement locations are shown in the inset.

This result gives an indication that one difficulty in PZT actuation is the spring legs cannot effectively transfer vibration energy to the sled during actuation. To excite a plate

mode, it is best to directly exert a force onto the sled plate and thus the magnetic actuation is a more suitable method.

6.3 Vibration of sleds on surfaces

After mode measurements (section 6.2), sleds from the D series were broken from the chip and dropped onto a clean mica or F-Si surface such that the tips of the sled are in contact with the surface. The mica or F-Si is then stuck to the actuation stage using Blu-Tack or double sided tape. We prefer using Blue-Tack as the adhesive because it is much easier to detach the mica or F-Si surface, which is important to avoid displacing the free standing sled resting on the surface.

The out-of-plane vibration modes are then measured using the PSV vibrometer and compared with the FEM simulation for a sled in contact with the surface (section 4.3.3.2). Magnetic actuation is used to measure circular sleds on mica (section 6.3.1), square sleds on mica (section 6.3.2), and circular sleds on F-Si (section 6.3.3). Both magnetic and PZT actuation is used for studying circular sleds on F-Si in vacuum (section 6.3.4).

6.3.1 Vibration of a circular sled on mica with magnetic actuation

The sleds D1 and D2 are placed on freshly cleaved mica and the mode shapes taken in ambient are shown in Table 6.4 for D1 and Table 6.5 for D2. It is clear that the mode amplitudes are much smaller than comparable data taken when the sleds were suspended on the chip e.g. compare with Table 6.2 for sled D1. The decrease in amplitude, presumably because some modes are now constrained by contact with the substrate or squeeze damping is present (see section 6.3.4), makes it difficult to observe the modes. This may be one reason fewer modes are visible. An alternative, equally valid

explanation is the legs are now removed and many of the low frequency modes associated

with leg movement for a suspended sled (Table 6.2) will disappear.

Table 6.4 Experimental mode shapes for sled D1 (300 μm diameter, 3.3 μm thick) placed on mica with magnetic actuation. The magnetic driving voltage is 10V for all modes.
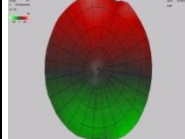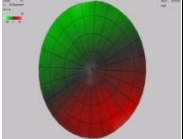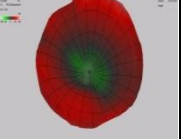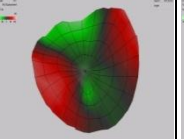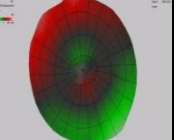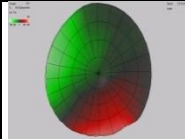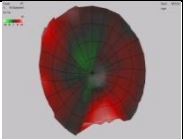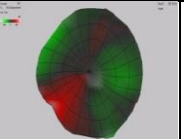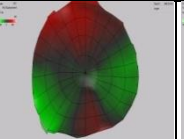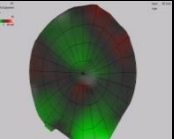
Mode	1	2	3	4	5
Range	±900 pm	±240 pm	±60 pm	±100 pm	±240 pm
f_o kHz	**95**	**150**	**330**	**415**	**456**

Table 6.5 Experimental mode shapes for sled D2 (300 μm diameter, 3.3 μm thick) placed on mica with magnetic actuation. The magnetic driving voltage is 10V for all modes.

Mode	1	2	3	4	5
Range	±300 pm	±80 pm	±180 pm	±160 pm	±1 nm
f_o kHz	**170**	**344**	**387**	**440**	**510**

In any case, the only *known* modes correspond to the 2nd free plate mode measured at 330

kHz for D1 and 344 kHz for D2, and the 1st free plate mode measured at 387 kHz or 440

kHz for D2 (the oscillation phase for which the snapshot is shown can be ambiguous).

The experiments for the suspended sled (Table 6.2) show a resonance frequency of ~330

kHz for the 2nd free mode and ~320 kHz for the 1st free mode, which closely matched the

corresponding FEM data. The FEM modeling of a circular sled on a surface (Table 4.6)

also shows that the resonance frequency should not vary greatly with changes in the tip-

sample interaction stiffness (k_{eff}) for the 2nd free mode.   Therefore the measured

resonance frequencies of the 2nd free mode for D1 and D2 on mica are in reasonable

agreement with those predicted from the FEM simulation and from the suspended sled.

There is less agreement for the 1st free mode (i.e. ~320 kHz compared to ~390 kHz or ~440 kHz) but we note that the 1st free mode is the only circular plate mode for which the resonance frequency changes considerably when placed on a surface (see Table 4.6). The difference between experiment and simulation suggests the tip-substrate interaction (k_{eff}) used in the FEM simulation should be even greater than 300 N/m.

The experiments also verify the onset of several low frequency modes (95 kHz and 150 kHz for D1, 170 kHz for D2) as predicted in the FEM study (Table 4.6, Figure 4.19), although it is not possible to directly compare the resonance frequencies because of the presence of the particle on the sled.

Table 6.6 The variation over time in resonance frequency for the modes having 1st and 2nd free plate mode shape observed during experiments on the sled D2 on mica.

Experiment	2nd free mode shape		1st free mode shape	
1st	390 kHz ±70pm		480 kHz ±400pm	
2nd	344 kHz ±80pm		440 kHz ±160pm	
3rd	360 kHz		468 kHz	
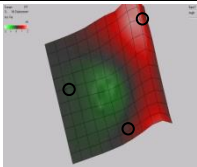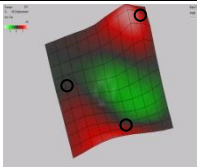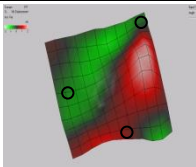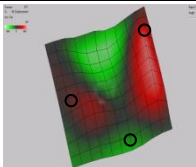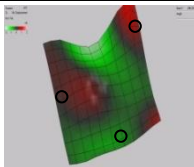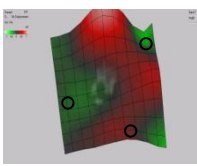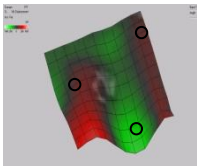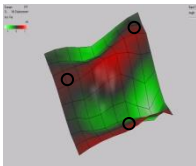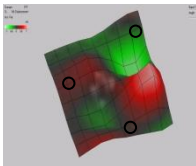
The agreement between the different sets of results is encouraging. However, some qualifications should be noted. The FEM simulation predicts the mode shape for the circular sled should be almost distortion-free (Figure 4.19) but this is clearly not the case experimentally (Tables 6.4 and 6.5). Also, the simple interaction model using k_{eff} predicts relatively small changes in resonance frequency as k_{eff} varies (Table 4.6). However, Table 6.6 shows a sequence of almost identical experiments on sled D2. The frequency of the

1st and 2nd free mode shapes clearly vary significantly (around ~10%). This could be due to changes in tip geometry or location on the surface, but in this example it is highly probable changes in k_{eff} arise from the variation over time of tip-sample capillary adhesion because water adsorbs readily on mica exposed to ambient.

6.3.2 Vibration of a square sled on mica with magnetic actuation

Experimental mode shapes for a free standing square sled (D6) on mica are summarized in Table 6.7. Many relatively large amplitude (nm) resonances are observed but none correspond to a free plate mode shape. Note that free plate modes were clearly measured at 300 kHz, 374 kHz and 549 kHz for this sled when suspended (Table 6.3).

Table 6.7 Mode measurement for the sled D6 (300µm square, 4µm thick) on mica. The approximate positions of the 3 tips are shown as circles. The solenoid driving voltage is 6V for all modes.

Mode	1	2	3	4	5
Range	±2nm	±1.8nm	±2nm	±540pm	±2nm
f_o kHz	**96**	**123**	**181.6**	**202**	**246**
Mode	6	7	8	9	
Range	±1.2nm	±500pm	±1.4nm	±1.2nm	
f_o kHz	**265**	**303**	**344**	**405**	

The results emphasize the importance of the tip positions and suggest the effective tip stiffness is high ($k_{eff} \gg 300$ N/m). Unlike the circular sled with tips near the circumference, the FEM simulation of a square plate in contact (Table 4.5) shows that for the tip locations chosen for the manufactured sleds, the mode shapes are distorted if k_{eff} is 300 N/m. In the simulation the free plates modes will still retain some symmetry even for
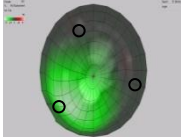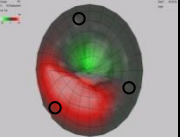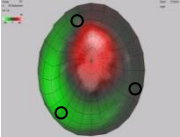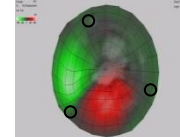
k_{eff}=300N/m, but the experimental data does not support this and indicates the tips have entirely disrupted the free plate modes. Square plates fabricated in future will need to more carefully consider the location of the tips with respect to mode shape.

6.3.3 Vibration of a circular sled on F-Si with magnetic actuation

The sleds D3 and D4 are placed on F-Si and the mode shapes taken in ambient. Data is shown in Table 6.8 for D3 and Table 6.9 for D4. Unfortunately, the results are inconclusive because free plate modes cannot be clearly assigned.

There are indications of a symmetric mode at 777 kHz for D4 (Table 6.9) but this frequency is far too high to be the 1st free mode, which occurs at 370 kHz for the same sled when suspended (Table 6.1). The resonance at 777 kHz must be a new mode. Further, the results do not show a 2nd free mode resonance near ~400 kHz, which is puzzling because this mode was clear for circular sleds on mica.
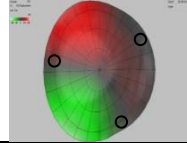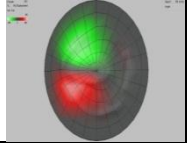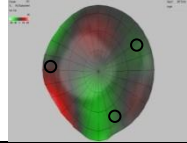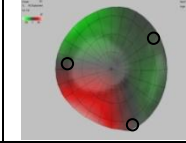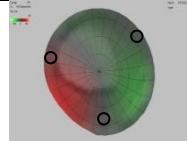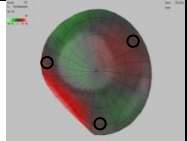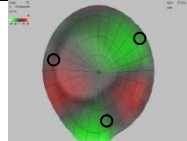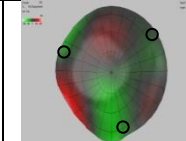
Table 6.8 Mode measurement for the sled D3 (300μm diameter, 3.3 μm thick) on F-Si. The approximate positions of the 3 tips are shown as circles. The solenoid driving voltage is 10V for all modes.

Mode	1	2	3	4
Range	±6 nm	±7 nm	±700 pm	±9 nm
f_o kHz	57	142	174	239

For the sled D3 (Table 6.8), the resonance at 174 kHz may possibly be the 2nd free mode. Although the frequency is very low, this sled has a much larger particle attached (~3 times more mass) and the additional mass will drop the frequency of the 2nd mode considerably (Figure 4.15). The larger magnetic volume also explains the larger oscillation amplitudes observed for sled D3.

Table 6.9 Mode measurement for the sled D4 (300μm diameter, 4μm thick) on F-Si. The approximate positions of the 3 tips are shown as circles. The solenoid driving voltage is 10V for all modes.

Mode	1	2	3	4
Range	±200 pm	±400 pm	±200 pm	±400 pm
f_o kHz	**66**	**191**	**255**	**293**
Mode	5	6	7	8
Range	±400 pm	±90 pm	±200 pm	±130 pm
f_o kHz	**315**	**570**	**777**	**887**

The underlying reason why the results on F-Si are less clear than comparable data taken on mica is unknown. One possibility is the experiments are more difficult on F-Si because the sled backscatter signal in the PSV is much weaker on F-Si substrates compared to mica, leading to poorer contrast in the mode images for sled D4. For sled D3 the displacement signals are large but one of the tips was found to be very blunt (Figure 6.4). One could speculate that the resulting strong tip-surface contact could greatly distort the mode motion. This explanation is tenuous because sled D4 was also imaged in SEM and all the tips were found to be sharp, yet the mode images remain poor. The sled displacement could also be much lower because of squeeze damping between the sled and the substrate, and this possibility is studied by placing the sled D4 under vacuum.
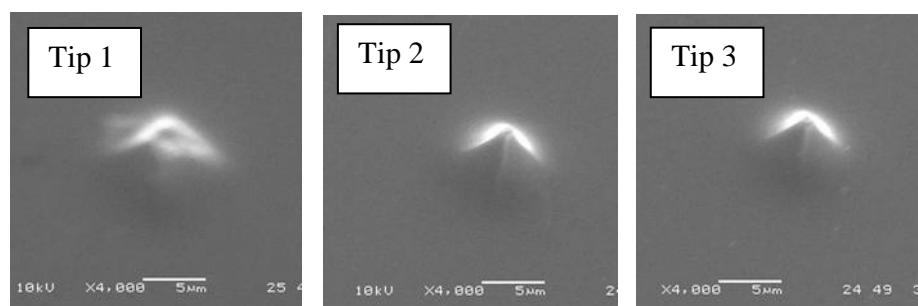
Figure 6.4   SEM images of the tips of sled D3 taken just before placing on a F-Si surface.   Tip 1 is noticeably blunt.

6.3.4 Vibration of circular sled D4 on F-Silicon in vacuum

The sled D4 on F-Si, as used in section 6.3.3, was placed under vacuum and the mode shapes taken using both magnetic and PZT actuation.
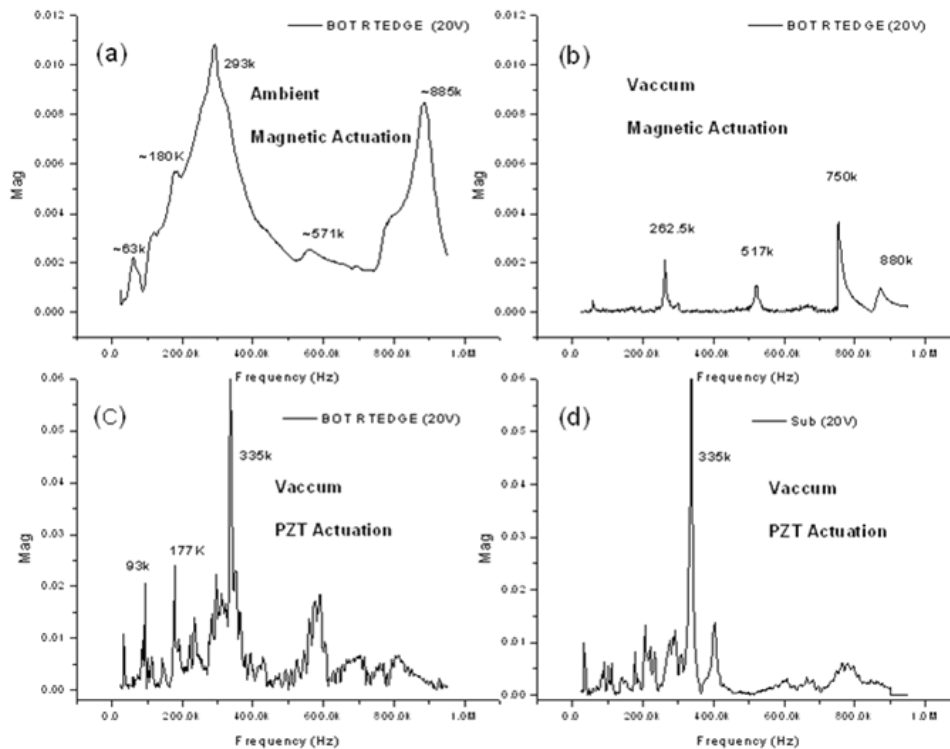
Figure 6.5 Spectrums taken at approximately the same location on sled D4 (300 μm diameter, 4 μm thick) placed on F-Si under different conditions. a) Taken in ambient using magnetic actuation. b) Taken in vacuum using magnetic actuation. c) Taken in vacuum using PZT actuation. d) Taken on the F-Si substrate in vacuum using PZT actuation.

Figure 6.5 compares some representative spectra taken over approximately the same location on the sled under the different actuation and environmental conditions. Compared with the spectra taken in ambient (Figure 6.5a), the widths of the resonances are significantly narrowed under vacuum (Figure 6.5b). For a sled still attached to a chip there is no significant change in the spectrums when vacuum is applied (section 6.2.3), and thus the results of Figure 6.5a and Figure 6.5b indicate a squeeze film effect is present when measurements are undertaken in ambient conditions. This is not surprising

because the tip height is less than ~4 μm, giving only a small gap between the sled plate

and the substrate. Note that Figure 6.5a is a rather extreme example with a quality factor

of only Q~20, whereas in ambient the Q value can be much larger.

Table 6.10 Vacuum measurement of modes for sled D4 (300μm diameter, 4μm thick) on F-Si using magnetic actuation. Note that the mode numbers have been assigned to similar modes of the corresponding ambient data (Table 6.9) or labeled as new modes that appear. The solenoid driving voltage is 10V for all modes except for 59 kHz which uses 3V. The approximate positions of the 3 tips are shown as circles.
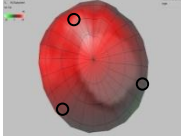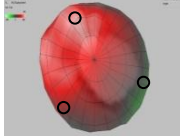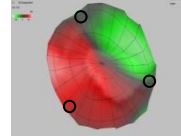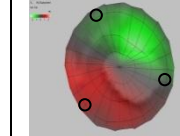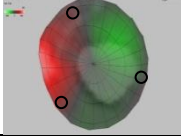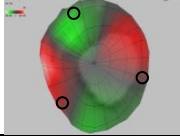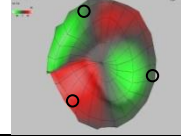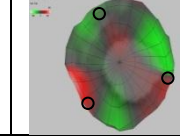
Mode	new	new	2	3
Range	±2.7 nm	±300 pm	±80 pm	±2.4 nm
f_o kHz	**59**	**86**	**171**	**262**
Mode	4	new- 1st free	7	8
Range	±2.4 nm	±500 pm	±2.4 nm	±140 pm
f_o kHz	**300**	**517**	**750**	**880**

Table 6.10 shows experimental mode shapes under vacuum using magnetic actuation.

Comparing the results to the corresponding experiments undertaken in ambient (Table 6.9)

we note that some of the mode shapes (modes 3 and 7) are much clearer to observe, with

a marginal visual improvement in other modes (modes 4 and 8). This is because the

mode amplitudes are an order of magnitude higher under vacuum for the same actuation

conditions. Interestingly this is not the case for modes 2 and 8, which have small

amplitude in vacuum and ambient. Clearly only some modes benefit from the lowered

damping and this appears to be associated with the position of the tips. For example,

modes 2 and 3 appear the same shape but there is a subtle difference. Two of the tips of

mode 2 are on a node line and this clearly restricts the out-of-plane sled motion. In

contrast, mode 3 has only 1 tip on a node line. Similar conclusions can be drawn by comparing the modes at 59 kHz with 86 kHz, and mode 7 with the mode at 517 kHz.

The lower damping conditions allow new modes to be observed and Table 6.10 shows the new mode at 517 kHz is similar to the 1st free plate shape. This mode was measured at 370 kHz in the suspended structure (Table 6.1) but the 1st free mode can also stiffen and have a large increase in resonance frequency if the tip-substrate interaction k_{eff} is high (Table 4.6). The FEM simulations (Table 4.6) predict a ~7% increase in frequency for k_{eff}=300 N/m whereas the experimental data shows a ~31% increase, implying the tip-substrate interaction is much more influential than the simulation would suggest. We again note that the 2nd free mode is not observed, and the reason for this is not clear.

Data for PZT actuation is now presented. Figure 6.5c shows a spectrum taken on the sled under PZT actuation. The resonance amplitudes are an order of magnitude larger than the magnetic actuation case (Figure 6.5b). However, the PZT spectra is significantly noisier with many small vibration peaks. Most of these peaks (if not all) are simply the substrate motion (Figure 6.5d) and it is therefore very difficult to assign any peak to a mode solely arising from a sled mode.

Table 6.11 shows experimental mode shapes under vacuum using PZT actuation. The substrate displacement is shown in addition to the sled displacement because the substrate movement serves as a reference for the magnitude of the PZT actuation.

The modes are different to those observed using magnetic actuation (Table 6.10). There is no indication of a 1st free plate mode, whereas the 2nd free mode shape (labeled as mode 4) now becomes observable under high PZT actuation voltage, with a resonance

frequency (404 kHz) comparable to that measured for the suspended structure (396 kHz, Table 6.1). FEM simulations (Table 4.6) show that the 2nd mode frequency will not change appreciably when a sled is placed on a surface. This result shows the modes measured using the suspended structure approach can indeed be related to the free structure on a surface, provided the actuation is sufficiently strong.
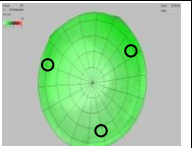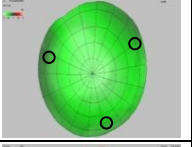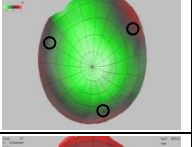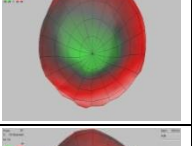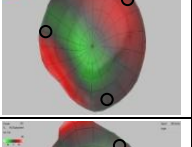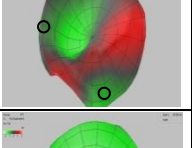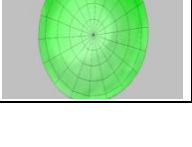
Three of the new modes observed (1, 2, and 7) appear to represent the entire plate simply being displaced vertically off the surface. The displacement of these modes is large and can be used for lateral actuation of plate motion, as will be discussed later. Modes 5 and 6 are also new but there is no understanding of the origin of these modes because we lack a detailed study of PZT actuation. Future research needs to describe the coupling of the substrate motion through the tips and to the plate, similar to studies on friction reduction induced by the ultrasonic vibration of surfaces.[113-115]

We now note an important observation. In all the results presented previously using magnetic actuation we did not observe any significant *lateral* movement of the sled across the surface during the PSV measurements. The situation is different for PZT actuation. During the first spectrum measurement, the sled was observed to move about ~30 μm as the frequency was swept before stopping at a scratch on the surface.

Only a large movement of the sled (e.g. greater than ~10 μm) can be clearly determined because of the poor optical resolution of the PSV. Such large movement is essentially sled actuation and is discussed in section 6.4, where it is found that repeatable lateral sled motion can occur near 177 kHz i.e. at mode 2 in Table 6.11. Mode 2 has the highest amplitude (5 nm with 10V PZT actuation) for sled D4 and it was found that lateral motion stops if the substrate amplitude falls below ~1 nm. Clearly, if the actuation is too small

the sled cannot move, irrespective of the mode shape, and reviewing our mode data taken using magnetic actuation we find the oscillation amplitudes are typically much smaller than ~1 nm. Thus it is not surprising lateral motion is not observed using magnetic actuation; the vertical displacement is too small.

Table 6.11 Vacuum measurement of modes for sled D4 (300 μm diameter, 4 μm thick) on F-Si using PZT actuation. The approximate positions of the 3 tips are shown as circles.

Mode	Drive voltage (V)	Range substrate	Range sled	f_o kHz	
1	10	1.2 nm	±1.1 nm	**94**	
2	10	1.1 nm	±5 nm	**177**	
3	10	1.4 nm	±2.5 nm	**221**	
4	46	750 pm	±600 pm	**404**	
5	28	1.1 nm	±1 nm	**760**	
6	30	130 pm	±90 pm	**893**	
7	10	___	±2.4	**935**	

There are examples using magnetic actuation in which large mode displacement occurs, such as with a very large particle (Table 6.8) or under vacuum (Table 6.10). However, lateral movement still does not occur because in these cases either two of the tips are

located at a node position or only one tip is on a node but the other two tips resonate in anti-phase. Mode 2 under PZT actuation (Table 6.11) shows all three tips moving in phase at large amplitude, and lateral motion can be observed. Thus the tip position and relative motion is an additional important condition for successful lateral actuation. The amplitude of the tip displacement should be large enough to overcome the tip-surface contact, especially in the presence of adhesion, and at least two of the tips should move in-phase.

6.3.5 Conclusions for vibration of sleds on surfaces

We now summarize some of the important conclusions from this section.

a) The results qualitatively match the FEM modeling of section 4.3.

b) The modes measured by the suspended structure approach (section 6.2) can be related to the free structure on a surface, provided the actuation is sufficient.

c) Magnetic actuation is cleaner than PZT actuation but has limited actuation displacement.

d) Tip location is important and can affect the mode shape for sleds on a surface.

e) The tip-substrate interaction can change the resonant frequency over time.

f) The modes appear different on mica and F-Si, but the reason remains unknown.

g) To induce lateral sled motion, the amplitude of the tips should be large enough to overcome the tip-surface contact, and at least two of the tips should move in-phase.

h) Experiments should be done under vacuum to remove squeeze damping.

i) PZT actuation needs analysis of the coupling of substrate motion to the sled.

6.4 In-plane actuation of sleds on surfaces

In this section we describe several experiments in which a sled is made to move laterally across a surface (mica, graphite or F-Si) using PZT actuation. PZT actuation is used because no motion was observed using magnetic actuation (i.e. the actuation force is too low). Unfortunately, with PZT actuation, we cannot compare with any theoretical analysis and data of the modes is sparse; our only experimental PSV data for a sled is summarized in Table 6.11. We will refer to Table 6.11 in our discussion but must note this data may not describe the actual sleds used.

Given these limitations, we simply note our observations in section 6.4.1 and 6.4.2, and then summarize in section 6.4.3. Linking the actuation of in-plane motion with specific sled modes must await future study. Further information showing movies of sled motion is provided as Supplementary Material.

Circular sleds of the C series (300 μm diameter, 3.3 μm thick) from the same fabricated batch are discussed. Square sleds could also be actuated. The experiments were mainly undertaken using the optical microscope setup (Figure 3.13b) because clear video images can be obtained, making it easier to view in-plane motion compared to the PSV setup. A sinusoidal voltage waveform is applied to the PZT, with the frequency and voltage adjusted manually. In a typical experiment, the frequency is manually ramped between two set frequencies at a constant peak-peak drive voltage. Lateral actuation of the sled can be observed as a sudden onset of rotation or translation as the frequency sweeps across a vibration resonance. If there is no movement, a higher voltage is applied to the PZT and the experiment repeated. Before each test, the sled is gently pushed by a gold wire at the sled edge to make sure no stiction occurs.

6.4.1 Motion of circular sleds on mica and graphite

Snapshots from a typical experiment are shown in Figure 6.6 for sled C1 on mica. The frequency is ramped between 384 and 460 kHz. We find that to actuate sleds on mica, a high voltage of $30V_{pp}$ is required, presumably because capillary formation occurs readily for this tip-substrate combination, thus increasing the adhesion force. Rotation about one tip or rotations of almost 360° are usually observed for sleds on mica. Small vibrations of the sled at a resonance can also be observed as a sudden blurring of the image at a particular frequency (file C1_II in the Supplementary Material).

| 62 sec | 78 sec | 84sec | 85 sec |
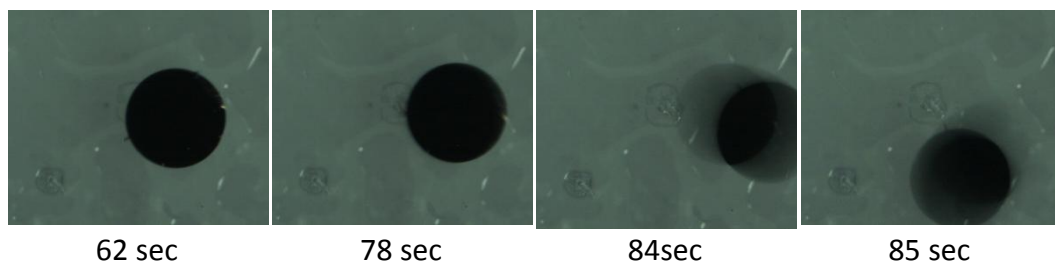
Figure 6.6 Snapshots taken during piezoelectric actuation ($30V_{pp}$ sine wave) of the sled C1 (300 μm diameter, 3.3 μm thick) on mica as the frequency sweeps from 384 kHz to 460 kHz.

Sled C4 could be actuated on graphite at a much lower voltage ($5.8V_{pp}$). In the frequency range 320 kHz to 330 kHz, the sled moved to another location on the surface with rapid motion, including both translation and rotation. After this sudden motion, the sled cannot be moved at all, even with $34V_{pp}$ applied over a broad frequency range. We hypothesize that at least two of the tips become pinned at the graphite step edges.

6.4.2 Motion of circular sleds on F-Si

The results on F-Si were the most fruitful because the actuation proved to be much easier than comparable experiments on mica. Three circular sleds (C3, C5 and D4) were used and often continuous motion of a sled could be achieved, sometimes moving rapidly over

millimeter distances on the surface. The motion could be turned on or off by changing the frequency over a narrow range.

Figure 6.7a shows a snapshot of rotational motion as the frequency is swept from 380 kHz to 360 kHz for sled C3. The motion can be actuated with voltages as low as $9V_{pp}$ and occurs only over a small frequency window (<<20 kHz) i.e. near a resonance. Two additional resonances were found between 320 kHz and 380 kHz on which actuation of sled C3 occurred. At ~320 kHz, a large translation was observed and the sled moves out of the camera frame to the edge of the substrate (Figure 6.7b).
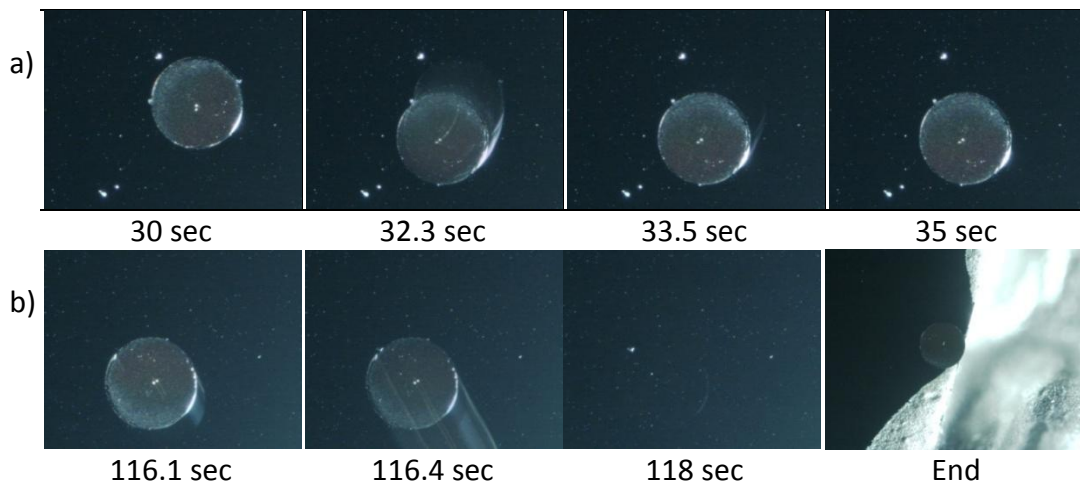
Figure 6.7 Snapshots taken during piezoelectric actuation (15Vpp sine wave) of sled C3 (300 μm diameter, 3.3 μm thick) on F-Si. The frequency is swept from, a) 380 kHz to 360 kHz, and b) 319.8 kHz to 324.3 kHz.

If the drive voltage is increased to $30V_{pp}$, then further frequencies can be found for actuation over an extended range of 280 kHz to 600 kHz. The observation that sled motion is most easily initiated with a frequency in the 300 kHz to 400 kHz range might suggest the 2nd free plate mode has been actuated (see mode 4 in Table 6.11). However, the existence of many resonances and an increasing number with increasing PZT actuation voltage, implies the motion arises in a manner similar to the ultrasonic lowering of friction[116-118] rather than a specific free plate mode.

There also appears to be another special frequency range for easy actuation near 180 kHz for all the circular sleds studied. Previously, a very strong mode at 177 kHz was measured in vacuum for sled D4 using PZT actuation (Table 6.11), corresponding to the whole plate moving vertically off the surface. For the sled C3, a smooth translation was observed within a narrow frequency range of 180-190 kHz. The sled moves slowly and continuously for several minutes with $15V_{pp}$ actuation. If the sled stops, a slight voltage increment sets the sled in motion again.

For the sled C5, translation with rotation occurs within a frequency range of 180-205 kHz using $2V_{pp}$ actuation. If the actuation is increased to $9V_{pp}$, the sled suddenly moves a large distance out of the camera frame. The results could be repeated several times.

For the sled D4, actuation occurred over the narrow frequency range 173-177 kHz. Initially, the sled translated ~100μm, then stopped momentarily, then moved again or rotated. This behavior continued for some time. In a following experiment, the sled started and then stopped with $15V_{pp}$ actuation (corresponding to a substrate displacement of ±1nm). On increasing the actuating voltage to $20V_{pp}$ the sled moved but then stopped again. We then used $25V_{pp}$ and the sled again moved and then stopped. Eventually the sled will firmly adhere to the substrate and we must gently push the device to re-initiate motion. We believe this behavior is related to defects on the surface. AFM images show there are particles and scratches in the FDTS coating. If a tip hits a defect, the tip can be pinned until a larger actuation amplitude is applied or some change in the tip location releases the tip.

6.4.3 Summary of sled actuation and Supplementary Material

All 300 μm diameter circular sleds could be actuated on mica, F-Silicon, and graphite. The actuation occurred over a narrow frequency window and was initiated most easily at 300 kHz to 400 kHz, or near 180 kHz. In general, a sled on mica requires a high actuation voltage (30V$_{pp}$), a sled on F-silicon requires a voltage of 9-15V$_{pp}$ and a sled on graphite requires 6V$_{pp}$.

Additional video movies of sled motion are shown in the Supplementary Material and some experimental details of each are provided. Rotation is observed, presumably as one of the tips becomes pinned on a surface defect or one of the tips is blunt. Translation across large (mm) distances on a surface could also be observed, showing that the basic concept of frequency control of the sled actuation is feasible provided the actuation amplitude is sufficiently large.

Often sleds cannot be moved, and must be gently pushed using a wire to initiate movement. Clearly the tips become trapped at surface defects or capillary forces have developed at the tips. Many sleds cannot be actuated even after gently pushing, especially after prolonged use, and one must assume tip wear or damage has occurred leading to larger tip-surface forces which cannot be overcome even using the largest actuation amplitude. Both of these effects highlight the importance of also having a suitable substrate i.e. a smooth, low energy surface with few defects, and low wear and friction for the given tip-substrate combination. In our work, F-Si best fitted these attributes and the actuation results indeed showed most promise using F-Si, although improvement in the quality of the F-Si coating is needed. The use of other suitable surfaces, such as diamond like carbon, and different tip material, such as silicon nitride, should be investigated to improve actuation.

Although PZT actuation has been used to show feasibility, the PZT approach is not well suited to MEMS applications. However, we are confident the method of controlled friction could be implemented using magnetic or electrostatic actuation, provided means can be found to produce sufficient actuation force. PZT actuation also suffers from having many small vibration resonances which may excite sled movement (Figure 6.5c), and the exact nature of each resonance depends on unknown tip-substrate coupling, as in friction lowering using ultrasonic vibration.[116-118] Magnetic or electrostatic actuation of only the sled structure offers clear, well defined modes, which is essential for the engineering of any practical device.

6.5 Conclusion

This chapter summarizes the vibrometer measurements of the sled modes and the actuation of the sleds. Both piezoelectric and magnetic actuations are explored, with magnetic actuation giving clearer resonance but piezoelectric drive providing stronger actuation. The mode results in ambient and vacuum environment are discussed, with squeeze damping effects observed under ambient conditions. The experimental modes are compared with the simulation results, and plate mode shapes are determined (see summary in section 6.3.5). The in-plane movement of free standing sleds was observed on different surfaces (mica, fluorine terminated silicon and graphite) under piezoelectric actuation and some qualitative conclusions drawn (see section 6.4.3).

Chapter 7 Special Cantilevers for Friction Study

7.1 Ultrathin Cantilevers for AFM Tribology Experiments

7.1.1 Ultrathin levers for friction measurement

In friction force microscopy (FFM), the AFM tip is in mechanical contact with the surface and slides along the surface. The static deflection in the sliding direction (Δx) measures the lateral force (F_L), and clearly in this static AFM based method $F_L = k_L \Delta x$. Typically the effective lateral spring constant of the cantilever (k_L) is high, usually >>10N/m (see Table 5.1). Such a high k_L limits the sensitivity of the FFM measurement to high friction force. This limitation is often of no concern because high applied loading and /or high friction coefficient at the solid (tip)–solid (sample) contact ensure high friction forces are present.

However, there is a large class of problems in which low friction forces and small coefficients of friction are highly desirable. Indeed, producing very low friction is a drive behind much tribology research, including liquid lubrication[119,120] and superlubricity[6]. A good FFM example is the lubrication of a mica surface in the liquid dodecanol[59]. With the tip in the dodecanol boundary layer, the friction is very low and cannot be measured by FFM. Once the tip pushes through the boundary layer and contacts the underlying mica the friction suddenly jumps to a high, measureable value.

To enable measurement of low friction force we propose and demonstrate the use of an ultra-thin cantilever used in contact mode AFM. Typical ultra-thin cantilevers have a bending spring constant of $k_L \leq 0.01\ N/m$.[46] Thus, if the cantilever is orientated

perpendicular to the sample surface (Figure 7.1), in the so-called pendulum geometry, the force sensitivity in the lateral (friction) direction can be extremely high, enabling ultra-low friction FFM to be undertaken.

In the following, aspects of the AFM pendulum geometry are discussed (7.1.1.1), including analysis in non-contact mode (7.1.1.2) and the new idea for use in contact mode (7.1.1.3), and a concept of reducing noise by mass loading the end of the cantilever (7.1.1.4). The later topic was proposed and tested by our collaborators at Basel University and is briefly introduced because the implementation of the idea greatly complicated the microfabrication requirements, as discussed in 7.1.2. Section 7.1.3 describes the characterization of the ultrathin cantilevers.

7.1.1.1 Ultrathin levers used in pendulum geometry

The pendulum structure was first introduced in AFM to allow the measurement of non-contact forces for scanning near field optical microscopy[45], using optical fiber type cantilevers. The geometry was also adopted for ultra-thin cantilevers for magnetic (NMR) and electron (ESR) spin resonance AFM[46], in which extremely high force resolution is required (less than atto-Newton sensitivity) in non-contact operation. Ultra-thin cantilevers are very soft and have excellent force sensitivity;[14] however soft cantilevers easily jump into contact when the attractive force gradient is larger than the spring constant, and thus the pendulum geometry has become common for high force resolution non-contact experiments. [121,122]

The new aspect we introduce (7.1.1.3) is to operate in contact mode for ultralow friction measurement, although the experimental setup is identical to standard pendulum mode AFM. Figure 7.1 shows schematically force microscopy in pendulum geometry. An ultra-thin cantilever is aligned perpendicular to the sample surface. The cantilever is

driven by a piezoelectric dither element to allow non-contact mode control and measurement to be undertaken if required. A bias voltage (V) is applied between the tip and sample to compensate the electrical contact potential, which is significant for non-contact operation. The sample is mounted on a piezoelectric tube scanner for displacement control. One of the major modifications of a standard AFM is to change the orientation of the sample by 90 degree to accommodate the pendulum geometry. Our collaborators in Basel can conduct experiment at cryogenic temperatures (7k) to further minimize noise and increase sensitivity.
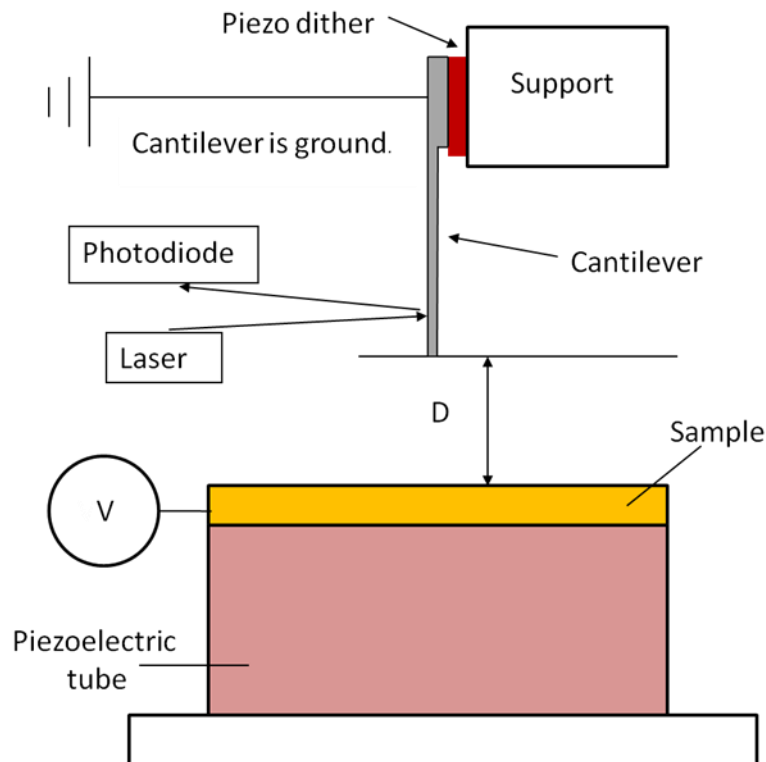
Figure 7.1 Schematic of the pendulum geometry. The cantilever response can be measured as a function of tip-sample separation (D).

7.1.1.2 Analysis of pendulum geometry AFM in non-contact mode[14,123]

The most sensitive mode of AFM operation for non-contact force measurement is frequency modulation (FM-AFM), and this is also the method adapted in Basel. Briefly, the cantilever is oscillated at a resonance (ω_0). Changes in the tip-sample forces shift the

resonance frequency by $\Delta\omega_0$ and $\Delta\omega$ can be measured with high accuracy. For small oscillation amplitudes, a linear approximation is valid and the frequency shift $\Delta\omega_0$ can be related to the tip–sample interaction force (F_n).

$$F_n = 2k_cL\frac{\Delta\omega_0}{\omega_0} \qquad (7.1)$$

where k_c is the spring constant and L is the length of the cantilever.

The changes in the amplitude of the cantilever can also be monitored and related to the change in the tip–sample dissipation forces, such as "non-contact" van der Waals friction[123]. The dissipative force is defined by $F_{diss}=\Gamma \cdot v$, where v is the velocity and Γ the damping coefficient factor, related to the quality factor (Q) as:

$$\Gamma = \frac{k_c}{\omega_0 Q} \qquad (7.2)$$

Ultra-thin cantilevers are excellent to sense force and dissipation because k_c is small and high quality factor can be achieved by use of crystalline Si. Note that any native oxide or surface contamination on pure single crystal silicon can greatly reduce the quality factor.[124]

7.1.1.3 Analysis of pendulum geometry AFM in contact mode

All previous studies of pendulum geometry AFM use non-contact mode operation. We propose a new technique based on contact mode measurement of low friction forces. The basic ideas turn out to be similar to the contact of a carbon nanotube (CNT) to a surface, in which the CNT either bends or buckles as the applied force increases.[125-127] Consider Figure 7.2 which shows schematically a pendulum type rectangular cantilever in contact with a flat surface. Experimentally it is not possible to have the cantilever exactly perpendicular to the surface[45,127] and the cantilever will be tilted at some small angle φ, as

shown. If the surface is displaced in the surface normal direction (z) the force acting on the cantilever tip will be,

$$F_z = F_n cos\varphi; F_x = F_n sin\varphi \qquad (7.3)$$

where F_n is the total force and the subscripts x and z label the force components.
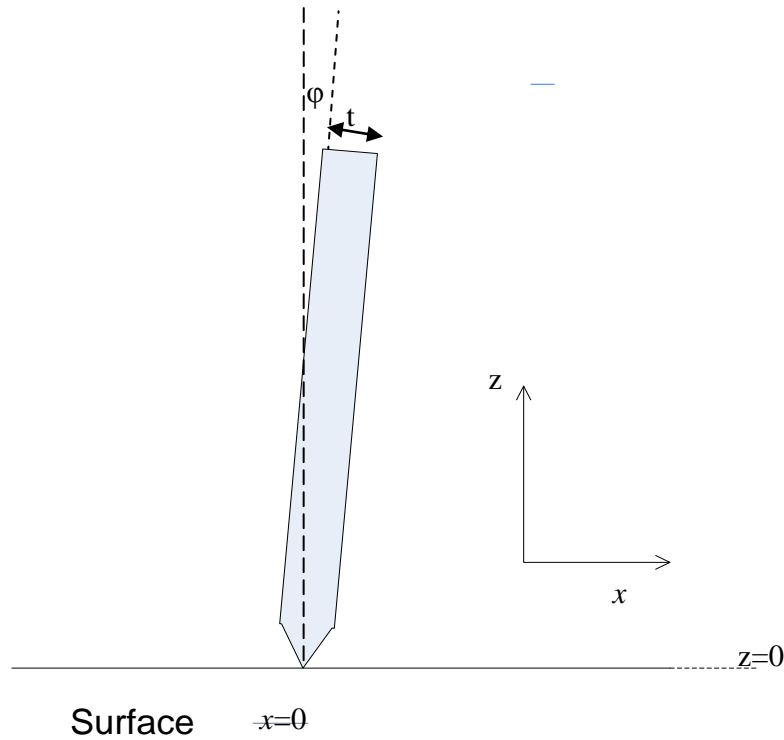
Figure 7.2 Schematic showing a cantilever in pendulum geometry and in mechanical contact with a flat surface. (a)

The corresponding displacement of the tip is,

$$z = F_z/k_A = F_n cos\varphi/k_A; x = F_x/k_c = F_n sin\varphi/k_c \qquad (7.4)$$

where k_c (or k_A) is the spring constant acting in the x (or z) direction.

In the compression (z) direction,

$$k_A = \frac{Ewt}{L} \qquad (7.5)$$

whereas k_c is simply the well known cantilever expression,

$$k_c = \frac{1}{4}\frac{Ewt^3}{L^3} \qquad (7.6)$$

From Eqn. (7.6) the ratio of the bending (x) to compression (z) is

$$\frac{k_A}{k_c} tan\varphi = \frac{4L^2}{t^2} tan\varphi \tag{7.7}$$

and Table 7.1 shows that for the ultra-thin cantilevers constructed in this thesis, this ratio is always very large. Therefore, practically all the tip movement is in the x direction and the cantilever undergoes bending, with curvature

$$1/R_{lever} \cong 2z/L^2 \tag{7.8}$$

as in standard AFM. An important point is that the above discussion assumes the tip will slip over the surface. This is a reasonable assumption because slip conditions are required for any measurement of a friction force and the technique is to be applied to systems of very low friction such that pinning is unlikely. At the other extreme boundary condition, the tip is pinned and in addition to bending, buckling can also occur[125]

Table 7.1 Calculated values of spring constants k_c and k_A for the two ultrathin cantilever designs. A Young's modulus of E=170GPa is used.

	Design 1	Design 2
Length (μm)	150	150
Width (μm)	5	5
Thickness (μm)	0.362	0.67
k_c (N/m)	0.0030	0.019
k_A (N/m)	2050	3790
$k_A tan\varphi/k_c$ $\varphi = 1°$	11927	3887
$k_A tan\varphi/k_c$ $\varphi = 5°$	59783	17479

Thus in a typical force curve measurement, the piezoscanner moves by a distance *z* and the lateral displacement is identical (*x=z*) because the tip slides on the surface. During sliding, the lateral force on the tip is a small constant (the friction force).

The total force can be found from eqn. (7.4) as $F_n = k_c z / sin\varphi$ since ($x=z$). To measure the friction force the AFM is controlled at low gain at a chosen value of force F_n. An oscillating triangle waveform, at a frequency higher than the control loop feedback, is applied to the tip by oscillating in either the x or z directions (Δx or Δz respectively). Since $\Delta x \cong \Delta z$ the lateral force is equivalent using either direction, i.e.

$$F_L = k_c \Delta x \text{ or } ; F_L = k_c \Delta z \qquad (7.9)$$

The friction force is then simply the value of F_L when the tip begins to slide (see Chapter 5, equation 5.5)

7.1.1.4 Concept of mass load cantilever

Analysis of noise and sensitivity in non-contact measurement is complex and reviews are provided in the literature[128-130]. For a rectangular cantilever oscillating on the first (fundamental) resonance frequency ω_0, the minimum force detectable (F_{min}) is limited by the thermal noise driving the cantilever, and is given by,

$$F_{min} = \sqrt{\frac{4 k_c k_B T}{\omega \cdot Q}} \sqrt{B} \qquad (7.10)$$

where T is the temperature, k_B the Boltzmann constant and B is the measurement bandwidth.[131]

The idea of the mass load cantilever is that by adding a mass at the end of the cantilever, the cantilever deflection is smaller at high eigenmodes. A conceptual design, which is fabricated, is shown in Figure 7.3.

The thermal vibration amplitude is also reduced at the higher harmonics. This is demonstrated in Figure 7.4 showing a simulation of the eigenmodes of a 150nm thick cantilever.

Top view of the Si-chip design

(the dimensions shown in millimetres)
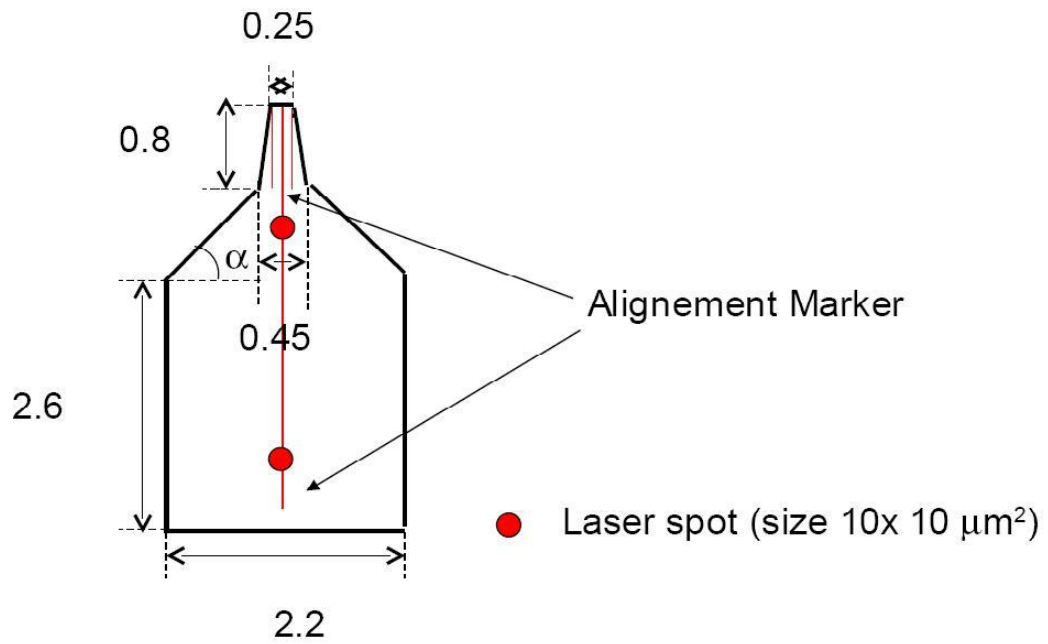
Top and side view of the cantilever
(the dimensions are shown in microns)
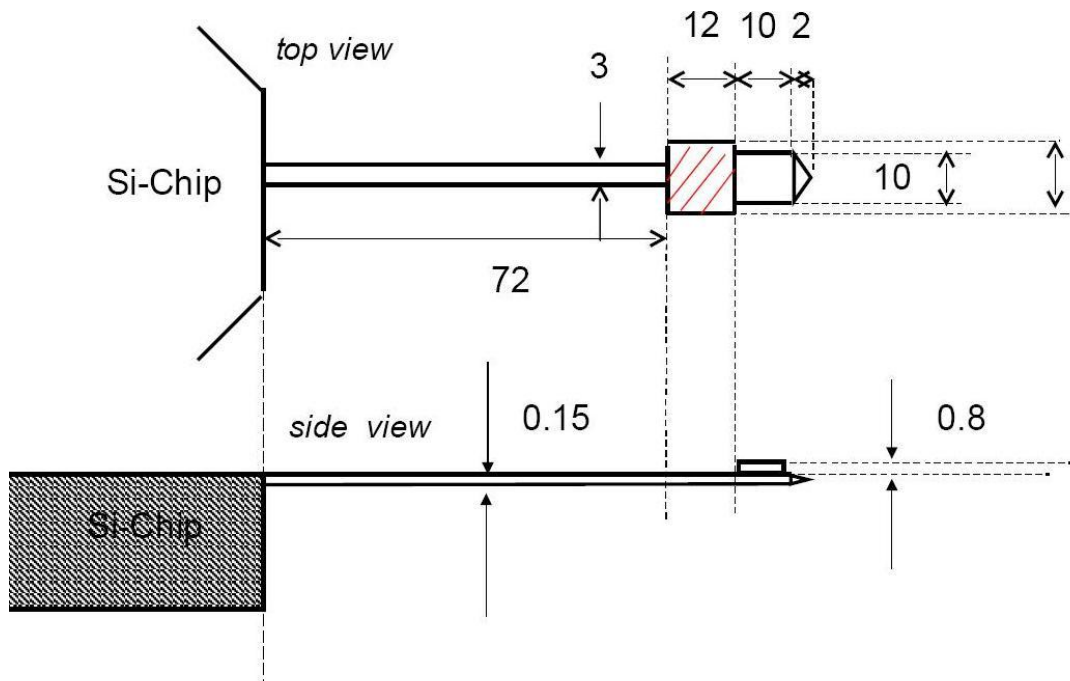
Figure 7.3 Schematic design of a mass load cantilever

ic
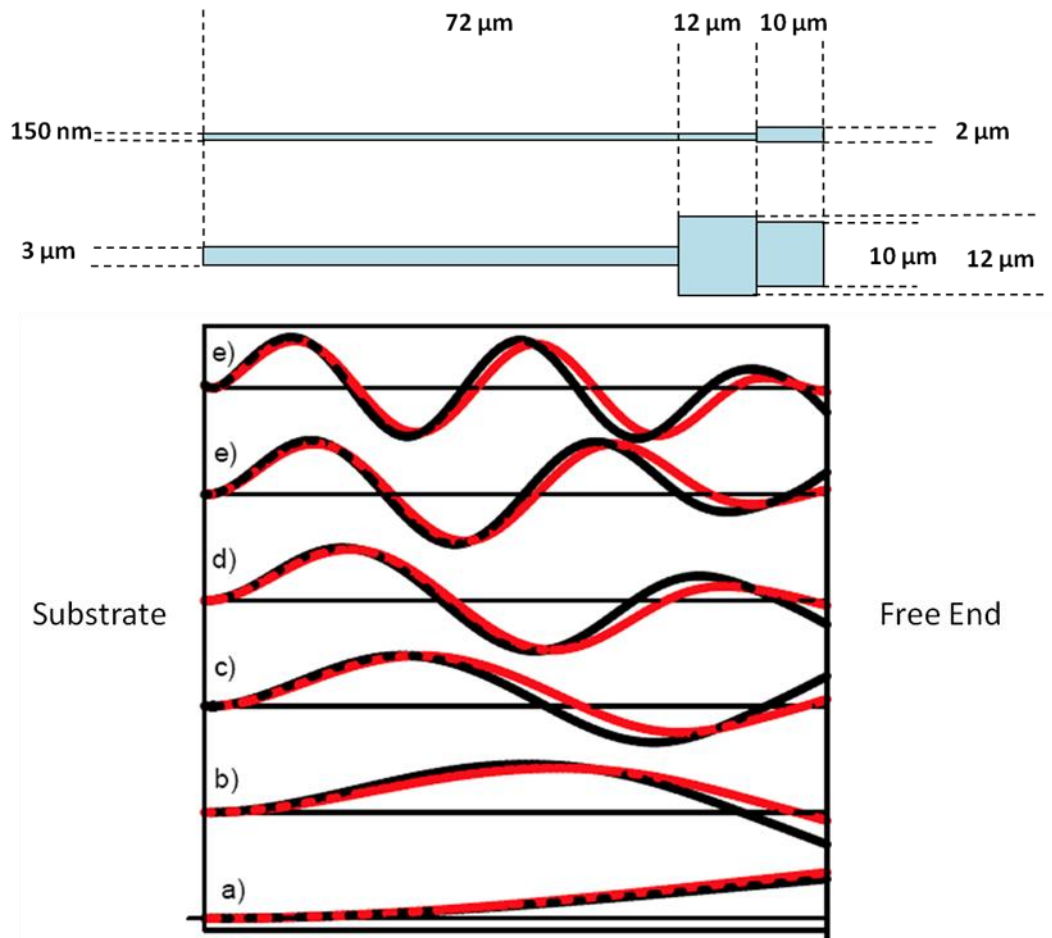
Figure 7.4 A simulation of the vibration amplitudes in the eigenmodes for a mass load cantilever (red) and a cantilever of the same dimension but with no load (black). At higher eigenmodes (b)-(e), the amplitude of the red curve is smaller than that of the black. The parameters of the cantilever are: $L_1= 72\mu m$, $L_2= 12\mu m$, $L_2= 10\mu m$, $W_1= 3\mu m$, $W_2= 10\mu m$, $W_3= 12\mu m$, $T_1= 150$ nm. The cantilever is silicon 150nm thick, and the mass load at the free end of the cantilever has thickness $t_2=2\mu m$.

7.1.2 Fabrication of the ultra-thin cantilever with mass load

From the discussion in Section 7.1.1, the ultra-thin cantilever should be made from single crystal silicon with minimal surface imperfections to increase the Q factor. The most important concern is the thickness control of the ultra-thin cantilever using thermal oxidation. It is a fabrication challenge to uniformly thin down the 2.5 µm silicon layer to 300nm or less because there is about 500nm variance in the thickness of the as-received

device layer. A sequence of three oxidation step is designed in the fabrication so that the thermal oxidation of silicon can be closely controlled. The second concern is the impact of etching damage to the surface. Dry etching of the cantilever surface is avoided since the plasma can produce surface defects. Dry etching is used only once to pattern the cantilever and during the procedure the cantilever surface is protected by photoresist.

The process sequence used to fabricate a very soft cantilever with a mass load is depicted schematically in Figure 7.5.

A SOI wafer (UltraTech, USA) with a 2.5 µm thick silicon device layer is used as the starting material. The interlayer oxide is about 1 µm thick and the total wafer thickness is about 500 µm. The backside substrate is polished.

RCA clean is first conducted on the SOI wafers. The wafers are dipped in 100:1 HF to remove native oxide before being loaded into the LPCVD furnace (Centratherm). A layer of smooth and stress free thermal oxide is grown on the wafer surfaces (Figure 7.5a). The recipe includes 3 growth steps: 100nm thick dry oxidization, 1µm thick wet oxidization, and another 100nm thick dry oxidation. The process temperature is 1000˚C for all steps. Only oxygen is used in dry oxidation, whereas oxygen and dichlorosilane (SiH_2Cl_2) are used for wet oxidation. The three step process is used to minimize the stress of the thick oxide.

The first lithography step (Karl Suss MA6) is to pattern the area of mass load on the SOI device layer (Figure 7.5b). Photoresist protects the oxide on top of the mass load, and the oxide layer covering other regions is removed using buffered hydrofluoric acid (BHF).

a) Start with SOI wafers with 2.5 µm thick device layer and oxide of 1µm

b) Pattern mass load area by wet etching

c) Oxidation for ~1.5 µm to form the mass load, then remove oxide

d) Precise align, pattern and dry etch cantilever structure

e) A further ~300nm thick oxidation to sharpen the tip

f) Align and pattern gold feature and guiding lines for AFM alignment

g) Backside alignment and etch through backside release hole

h) Release the mass loaded cantilever

Silicon   Silicon oxide   Cr/Au layer

Figure 7.5 Fabrication process flow for mass loaded cantilever

A second RCA clean and HF dip is conducted, and a thermal oxidation step as in Figure 7.5a follows. The exposed silicon device layer is further oxidized for 1.5 μm. The device layer is then uniformly thinned by oxidation to ~400nm thick except for the mass load area, where the silicon is covered by thick oxide (although the sidewalls of the mass load area is also oxidized inward, as shown in Figure 7.5c).

After removal of the oxide layer by BHF, lithography and silicon etching are used to produce the cantilever structure, as shown in Figure 7.5d. A 2μm thick photoresist is uniformly covered on the whole wafer surface. Contact mode lithography is used to ensure the cantilever features are precisely aligned to the mass. Silicon etching is conducted by RIE (Oxford 80) in a SF_6 based plasma. Silicon etching generally uses SF_6 and C_4F_8 based deep RIE, but this is not selected since C_4F_8 plasma can result in a surface polymer coating and decrease the quality factor.

A third RCA clean with HF dip is conducted and is followed by dry oxidation. This step is used to sharpen the end of the cantilever, which acts as the tip in pendulum geometry, and also precisely thins the cantilever thickness to 300nm or less (Figure 7.5e).

The oxide layer is then removed by BHF etching and the next step is to fabricate Cr/Au features on the cantilever (see Figure 7.5f). The metal is used for easy AFM optical alignment and measurement. A metal lift off process is used with a mask made in reversed tone. A 5μm thick photoresist is applied and an image reversal step (YES engineering oven) is used to reverse the photoresist tone and to make sharp photoresist edges. Electron-beam evaporation then deposits a 0.5nm Cr and 10nm Au thin film. The wafers are immersed in acetone overnight to remove the photoresist and metal covering the photoresist.

Further lithography and dry etching steps are used to pattern the backside release hole (Figure 7.5g). A 10 μm thick photoresist uniformly covers the whole wafer backside. The lithography step (Suss MA6) is followed by a silicon DRIE process to etch the backside opening, with photoresist as the mask (Oxford 100). The etching process is stopped when the etching depth almost reaches the SOI oxide because further DRIE plasma could produce heating to the oxide layer and can damage the cantilever features i.e. thermal stress. Therefore, XeF_2 vapor etching is used to completely remove the silicon left underneath the SOI oxide. XeF_2 etching is a pure chemical etching process with an isotropic etching of silicon and almost no impact to the SOI oxide.[66]

A standard MEMS wet release process follows by sequentially transferring the chip in several beakers with solutions (BHF, DI water and IPA) as discussed in Section 3.1.1.5. In the wet release, careful handling of the dip is critical since agitation could break the microstructure. In the final step, the chip is transferred out of IPA and is air dried (Figure 7.5h).

The above processes gave ultra-thin silicon cantilevers with a pure silicon mass at the free end, as shown in Figure 7.5. The thickness of the cantilever varies between 230nm to 600nm across the 4 inch wafer, and the cantilever yield is ~70% per wafer.
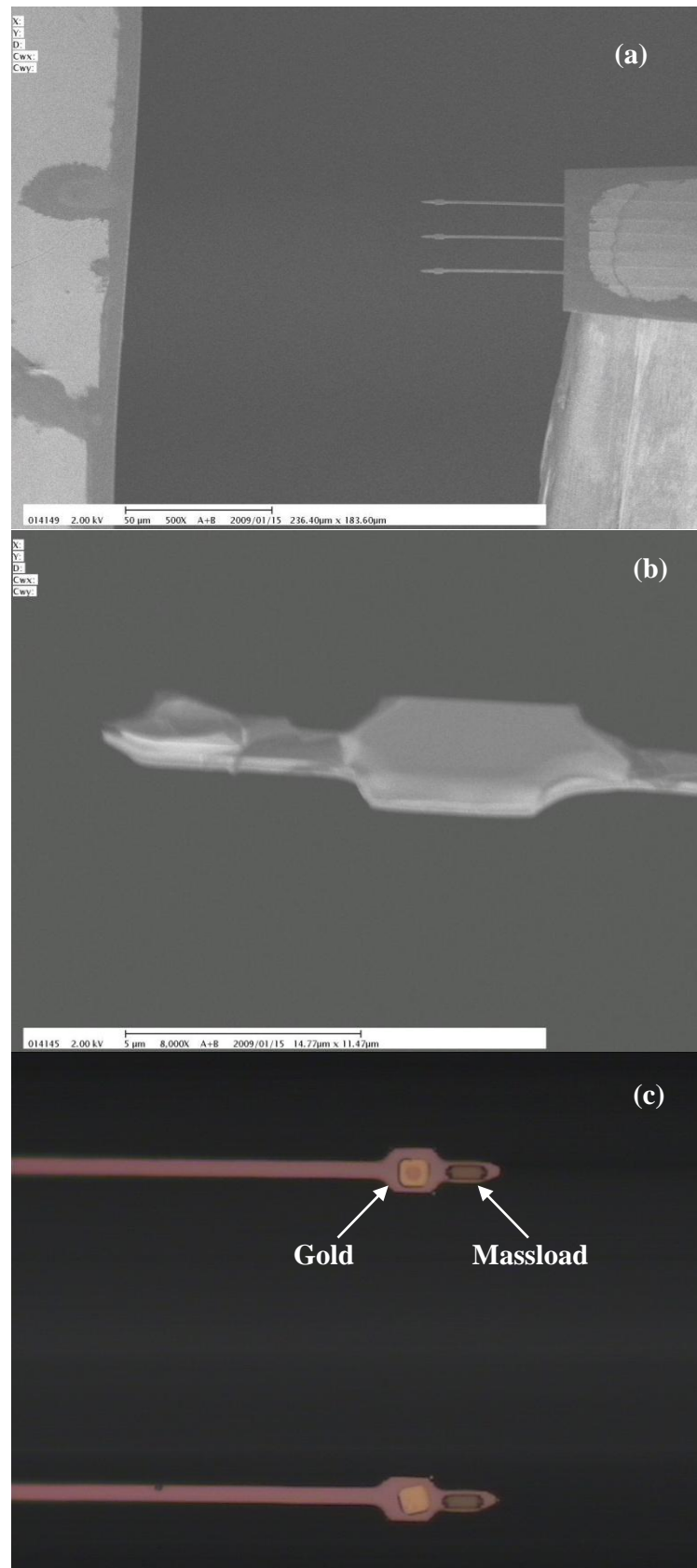
Figure 7.6 Photos of fabricated mass load cantilevers. (a) SEM of 3 cantilevers on a chip that can be directly mounted on an AFM (b) SEM of the mass load region and the tip at the free end of the cantilever. (c) Optical photo of the mass load cantilevers showing gold coated region near the mass load

7.1.3 Characterization of mass load cantilever

Table 7.2 shows typical properties of ultrathin cantilevers experimentally determined at Basel University. The cantilevers have a measured fundamental eigenfrequency ranging between 20–22 kHz for 362nm thick and around 41 kHz for 645 nm thick cantilevers, in good agreement with the theoretically predicted values. The ring down time of the decay response, however, is less than 1 sec, whereas the ring down time should be several seconds for a good cantilever. The small ring down time, or alternatively low Q value[132], indicates internal friction losses are occurring. EDX studies of the cantilever surfaces showed that no silicon oxide or polymer residue from the processing was present. Further, annealing the cantilevers in vacuum did not increase the ring down time.

Table 7.2 Properties of Cantilevers Measured at 300 K.

Length	µm	150	150
Width	µm	5	5
Thickness	nm	362	670
Spring Constant	N/m	0.003	0.019
Decay time	s	1	1
Quality Factor		69587	129144
Frequency ($\omega_0/2\pi$)	Hz	22150	41108

The most likely problem leading to lowered Q value is inhomogeneous surface topography along the cantilever surface. Figure 7.7 clearly shows the surface is not smooth. Earlier observations of silicon cantilevers indicate that the smoothness of the cantilever has a considerable influence on the quality factor.[133] In general an inhomogeneous surface structure lowers the quality factor, presumably by increasing the surface stress-strain losses as the cantilever deflects.[134]
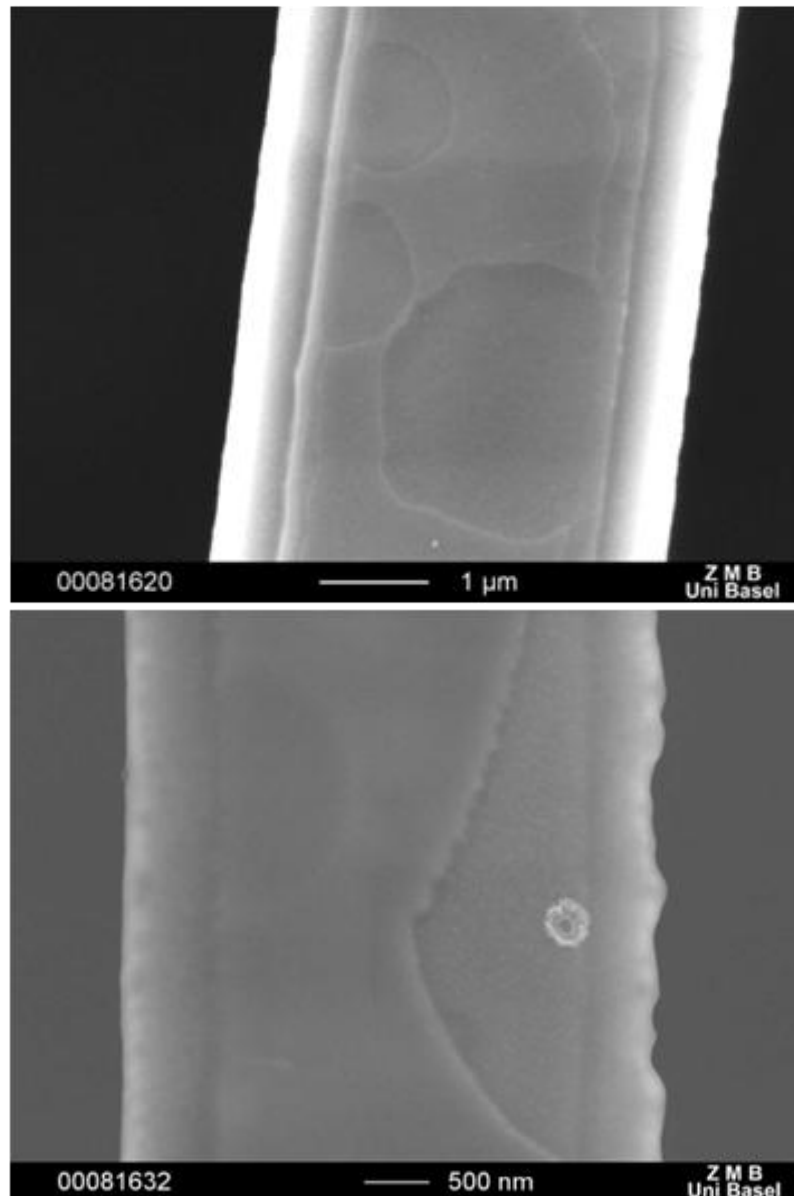
Figure 7.7 SEM of inhomogeneous surface topography along a mass loaded cantilever

The inhomogeneous structures themselves are most likely produced by the doping inside the silicon device layer. Dopants are distributed inside the silicon device layer and can form defects on the silicon surface during high temperature oxidation. In any event, the cantilever Q needs to be improved for non-contact experiments requiring force resolution in the atto-Newton or lower range.

7.2 Cantilever for dynamic droplet-droplet or bubble-bubble experiments in liquid

7.2.1 Introduction

7.2.1.1 AFM in Liquids and hydrodynamic force

Measurement of the hydrodynamic drainage between approaching surfaces is very important for lubrication of surfaces and also adhesion between particles. Indeed, most lubrication is based on keeping two surfaces separate from each other by use of an intervening liquid,[93] with the load supported by hydrodynamic forces generated by the relative movement of the surfaces. The removal of liquid (drainage) in the surface gap, particularly the velocity dependence of the hydrodynamic force, is therefore critical in understanding how to keep two surfaces apart for effective lubrication.

AFM can be used to obtain drainage data at nanometer separations and with very high force resolution. In collaboration with Melbourne University we have studied the drainage of water films between two approaching bubbles or droplets. Melbourne University undertakes the theory and AFM measurements, and these tasks are only briefly outlined below. My task was to manufacture and characterize the special cantilevers required. Specifically, bubbles need to be reliably attached to the free end of a cantilever, and subsequently used as a colloid probe type AFM[99] in aqueous solutions. This is achieved by suitable patterning and molecular functionalization of the free end of silicon cantilever.

AFM can be operated in liquid environments when the sample and the cantilever are completely immersed in liquid media. There are several advantages of using AFM in

liquid. For example, it allows a much better control over tip-sample contact forces than in air by eliminating capillary forces, and a degree of control over surface contamination. More importantly, liquid AFM can study a wide range of phenomena occurring at liquid interfaces. In our collaboration with Melbourne University, the hydrodynamic force between bubbles or droplets is investigated with liquid AFM. Like Strokes friction, the hydrodynamic force is proportional to the velocity. However, it also depends strongly on the bubble–bubble or bubble–surface separation, because as the gap gets smaller it becomes more difficult to remove the liquid from the gap. The hydrodynamic force is therefore repulsive upon approaching and attractive upon retraction.

7.2.1.2 The droplet-droplet experiment

Bubbles (or droplets) are also highly deformable i.e. soft, and analyzing the hydrodynamic force between bubbles is difficult. There are three disparate length scales: the bubble or droplet radii, on the order of 50μm; the axial length scale of the interaction force h(r,t), around 10 to 100nm; and the radial length scale of the interaction, around 5μm (see Figure 7.8).[93] Different types of force dominate at different length scales. By using liquid AFM the hydrodynamic forces can be measured directly and compared to theory.

A schematic diagram of the droplet-droplet setup in Melbourne University is shown in Figure 7.8. In a typical droplet experiment, a tetradecane droplet is anchored on the end of the AFM cantilever as a soft colloid probe. Some droplets (or bubbles) are then stuck onto a glass slide substrate. The soft colloid probe is then aligned to the crest of one of the substrate droplets. Approach and retract force curves are then recorded at different speeds.
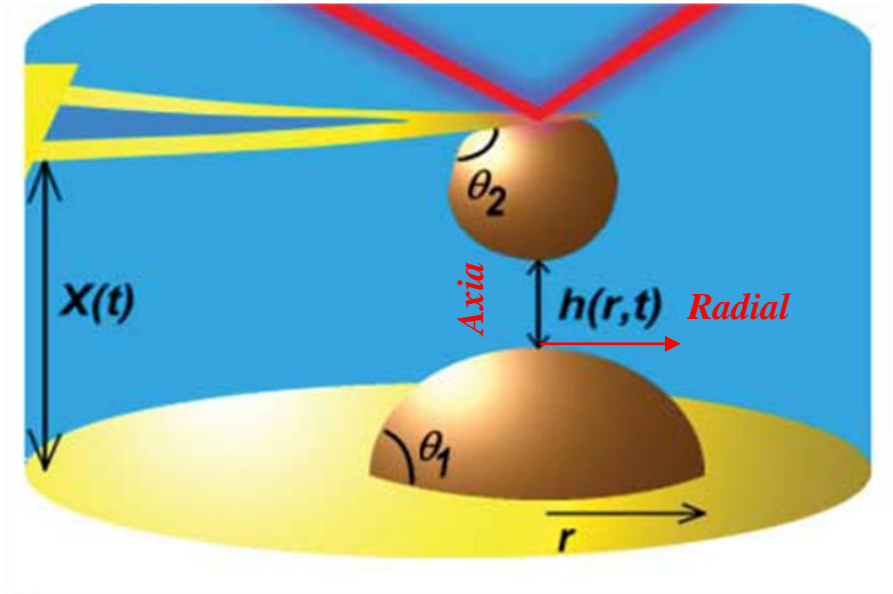
Figure 7.8 Schematic diagram of the experimental setup used in droplet-droplet experiments[137]

The experiment allows for precision measurement of hydrodynamic forces because all the parameters are known or measured. The droplet size and alignment can be monitored by inverted microscopy and controlled by AFM piezoelectric positioners. The separation of the droplets h(r,t) can be precisely determined by AFM and the velocity $\dot{X}(t)$ of the force curve controlled by the precision movement of the AFM peizo-stage. The force acting on the droplet (or bubble) probe can be measured with accuracy, provided the cantilever spring constant is known. The deflection of the cantilever as a function of time, *d(t)*, and the movement of the piezo as a function of time, *X(t)*, provides a force-displacement relationship for a given interaction.

A typical force curve for a droplet to droplet experiment is shown in Figure 7.9. The force distance (F-D) curves show the approach and retraction of a ~50μm radius tetradecane droplet anchored on a 0.04N/m cantilever. Note ΔX= 0 is arbitrary and the true separation h(r,t) between the droplets must be found analytically.[136]
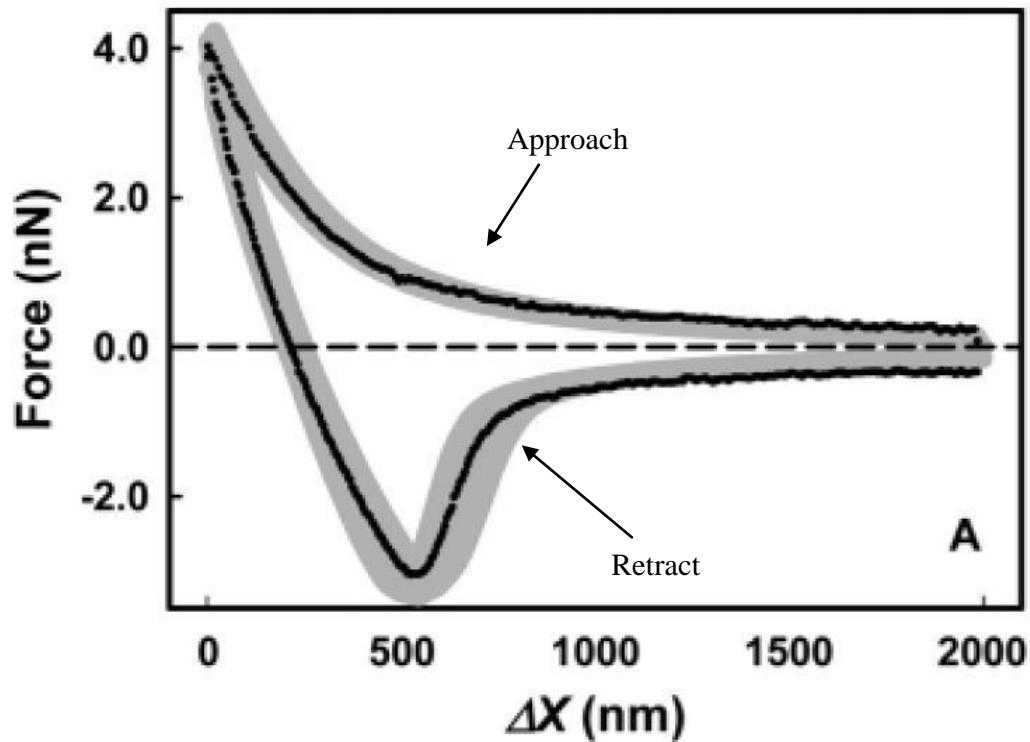
Figure 7.9 A typical AFM force-distance curve measured for a tetradecane droplet to droplet experiment. The grey area denotes the measurement uncertainty. ΔX is the change in piezoelectric displacement.[137]

However, there are two major problems which arise from the use of commercially available cantilevers. Firstly, the bubble or droplet must be precisely located at the free end of the cantilever. Secondly, the largest source of error on the force data results from the calibration of the cantilever spring constant. The grey regions in Figure 7.9 show the bounds of uncertainty. Given that force curves must be modeled to extract the hydrodynamic force as a function of h(r,t) and velocity,[137] it is critical to minimize experimental error by constructing cantilevers with well-defined spring constant.

7.2.2 Fabrication of cantilever for colloidal probe AFM

7.2.2.1 Special cantilever design

Two major improvements were made on the cantilever design. First, single crystal silicon is used instead of Si_3N_4 in the construction of very soft cantilevers (spring constant can be

as small as 0.04 N/m). The material properties of crystalline silicon are superior to Si_3N_4

and more importantly are well defined. Special attention is made to precisely control the

cantilever dimension and thus to maintain a consistent spring constant for the same type

of cantilevers across the entire wafer.

Secondly, a thin gold feature is designed at the end of the cantilever. The metal feature is

a square or coin shape and is used to pickup and anchor a bubble or droplet. For some

types of cantilever, the end of the Si cantilever itself is made to have the square or coin

shape to remove any unwanted wetting or unpinning of the droplet / bubble contact due to

the presence of silicon. Two typical designs with dimensions are shown in Figure 7.10.

Other related types of designs are also fabricated.

7.2.2.2 Fabrication steps for special Cantilever

The process sequence used to fabricate the special cantilever is depicted schematically in

Figure 7.11. The major challenge is the precision alignments required to produce the Au

patterns on the end of the cantilever. The process starts with a SOI wafer as shown in

Figure 7.11a. The silicon device layer is 2.5 μm, the interlayer oxide layer is about 1 μm

thick, and the substrate layer is about 500 μm thick. The backside substrate is polished.
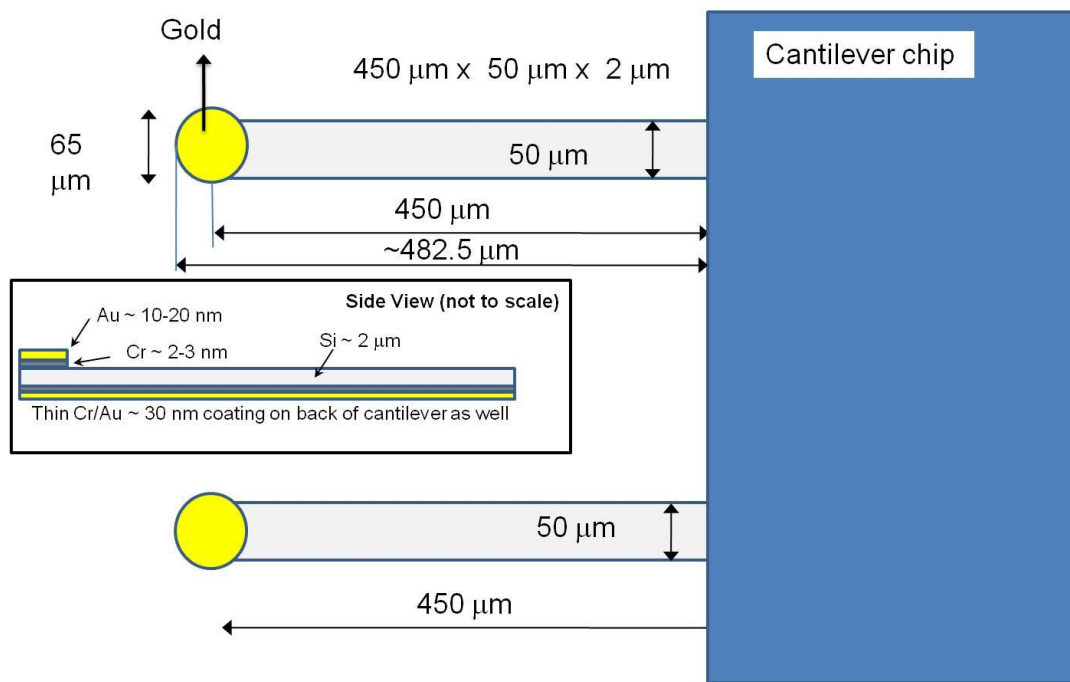
Design type 1
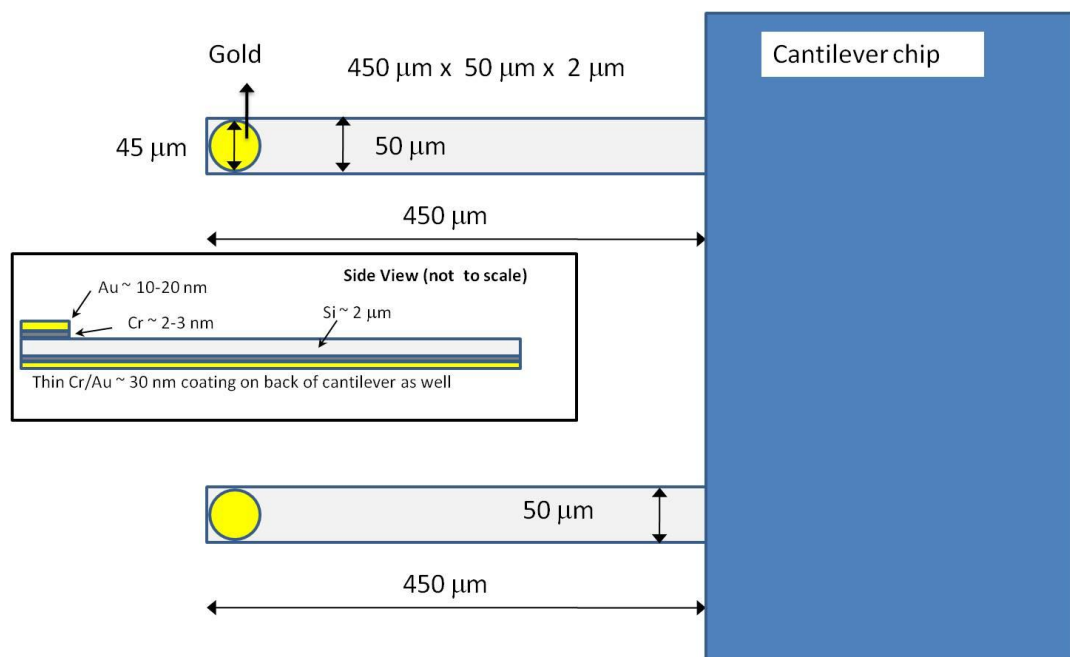
Design type 2

Figure 7.10 A schematic showing two typical cantilever designs

a) Start with SOI wafers with 2.5 µm thick device layer

b) Formation of cantilever structure

c) Precise lithography alignment for Cr/Au patterns at end of cantilever using lift off method

d) Precise lithography alignment and formation of backside hole via DRIE/RIE

e) Release cantilever on whole wafer by wet release method

f) Deposit Cr/Au at wafer backside

Silicon   Silicon oxide   Cr/Au layer

Figure 7.11 Fabrication flow to produce cantilever for a soft colloidal probe

The mask set is fabricated by direct laser writing (Heidelberg DWL66). To ensure precision cantilever dimensions, masks with quartz plates are used instead of more typical glass plates because the quartz plate has a low thermal expansion coefficient.

The first lithography step is to fabricate the cantilever structure (Karl Suss MA6) on the SOI device layer. To ensure the dimension precision, vacuum contact mode is used where the mask plate firmly contacts the photoresist using vacuum. The vacuum contact mode can be used since both mask and wafer are totally flat, and ensures the light intensity is uniform across an entire wafer to precisely transfer the mask features to the photoresist. After lithography, silicon DRIE etching is conducted (Oxford100). A straight sidewall is formed and the etching is stopped at the interlayer oxide (Figure 7.11b).

The second lithography process is to produce the metal features at the end of the cantilever. A 3 µm thick photoresist uniformly covers the whole wafer surface. Hard contact mode is used that provide the best feature resolution (~1µm) on the wafer surface with topology. During the mask aligner operation, a repeated alignment in proximity mode is conducted with the mask in close proximity to the wafer to recheck the alignment. Both exposure and development processes are tuned to form a near 90 degree photoresist profile. Metal deposition and lift off follows (Figure 7.11c). Layers of 20 nm thick Au / 1 nm thick chrome are deposited (Edwards 360 E-beam evaporator). The wafer is then immersed into acetone overnight to remove the photoresist, leaving only the metal coin or square features at the cantilever end.

The third lithography step follows to pattern the backside release hole. A 10 µm thick photoresist is coated on the wafer backside. The backside alignment and exposure is then conducted (Karl Suss MA6). Since standard backside alignment could produce about 20 µm additional alignment shift, the alignment marks are optically enlarged about 5 times during the process.

Silicon DRIE is then used to etch the backside opening with photoresist as the mask (Oxford 100 DRIE). It is generally difficult to keep the photoresist and maintain the photoresist profile while etching 500µm in depth. In our case, to ensure the deep etch has improved selectivity, a special cooling step is added between the standard Bosch deposition and etch steps. The selectivity between silicon and photoresist effectively reaches about 30:1. The etching progress is stopped when the etching almost reaches the interlayer oxide, where a red light spot on each release hole can be seen optically when light is shining from the backside. A low density silicon RIE process follows (Oxford 80) to ensure a straight silicon sidewall. The process is completed when all of the silicon in the exposed region is removed. The final profile is shown in Figure 7.11d.

A MEMS wet release process follows (see Figure 7.11e). During the release, solutions of BHF, DI water, Methanol, and IPA are sequentially used as discussed in Section 3.1.1.5. In the final step, the wafer is transferred out of IPA and is air-dried. The release is conducted on the whole wafer and care is required in transferring the wafer in or out of the liquid/air interface. The pulling or immersing direction should align with the released cantilever beam for the best yield (about 90%).
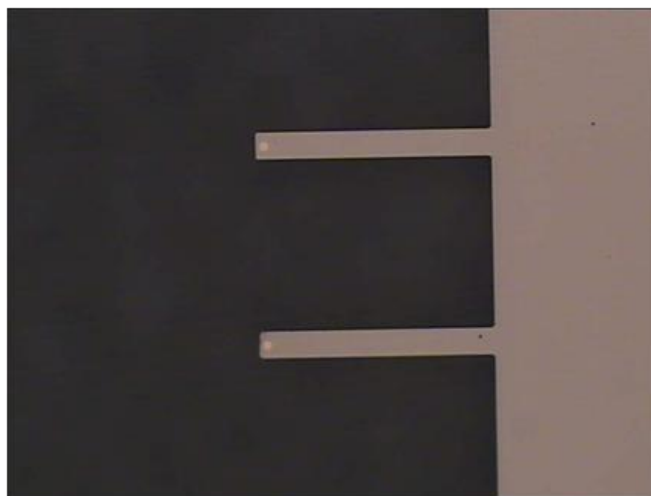
Figure 7.12 Photograph of gold coin cantilevers batch-fabricated on SOI wafer

In the last step (Figure 7.11f), 1nm thick chrome and 20nm thick Au films are evaporated on the cantilever backside (Edwards 360). This metal layer provides a reflection coating for improved operation of the AFM optical detection. Figure 7.12 shows a photograph of the completed cantilevers.

7.2.3 Characterization of the cantilevers

7.2.3.1 Calibration of the cantilever spring constant in air

Individual cantilevers were tested on an Aslyum MPF-3D AFM (Santa Barbara, USA) mounted on a Nikon TE-2000 inverted microscope. The spring constant is found by measuring the resonant frequency, and then calculated using either the method of Cleveland[138] or the thermal spectrum method of Hutter and Bechhoefer[139].

In thermal spectrum measurement, the first step is to measure the deflection sensitivity in contact mode when the cantilever approaches a surface. The same measurement is repeated at least 5 times to obtain the average deflection sensitivity. In the second step, the thermal spectrum is measured when the cantilever is not touching the surface. The fundamental frequency is selected and the AFM software calculates the spring constant based on the measured deflection sensitivity.

Table 7.3 shows measured values of the spring constants k_c, quality factor Q and fundamental frequency f_0 for design type 1 and design type 2 (Figure 7.3). Four rectangular cantilevers of design type 2, taken from different chips on a wafer, are measured.

With good control of the in-plane dimensions of the cantilever in microfabrication, the variation of the spring constant is mainly dependent on the cantilever thickness (equation

5.8c), and the thickness is dominated by the local thickness of the SOI device layer. The manufacturing spec of the SOI wafer are 2.5±0.5µm (Ultratech), the variance of the thickness could readily explain the small variations in f_0 and k_c.

Table 7.3 Values of the measured spring constant k_c, quality factor Q and fundamental resonant frequency f_0 in air for 1 device of design 1 and 4 devices of design II

Cantilever Type	Design 1	Design 2a	Design 2b	Design 2c	Design 2d
Q	120.0	43.7	45.4	43.1	42.0
f_0 (kHz)	27.151	5.778	6.503	5.776	5.767
k_c(N/m)	0.084	0.045	0.048	0.047	0.050

7.2.3.2 Characterization of the cantilevers in the fluidic cell

The other requirement of the new cantilevers is to be able to pick up and form stable bubbles or droplets on the metal pad at the end of cantilever, and this was successfully demonstrated using the Aslyum MPF-3D AFM.

Surface modifications of the substrate and the cantilever are required. The substrates are circular glass slides used specifically for the liquid cell of the AFM. The glass disk is mildly hydrophobilized by immersing briefly in a 3mM solution of octadecyltrichlorosilane in heptane to give a water contact angle in a range of $20 - 60°$. For the cantilever, the gold area at the end of the cantilever was hydrophobized by immersing the cantilever overnight in 10mM n-decanethiol solution in ethanol. The degree of hydrophobicity of the glass disc substrate must be lower than the alkane-thiol coated cantilever gold pads so that the droplets can be picked up by cantilever.

Liquid AFM experiments were generally undertaken in 0.1-10mM Na^+ electrolyte solution. Tetradecane oil droplets on the glass surface are generated by a needle syringe and the droplets are sprayed onto the glass surface. This process is undertaken in a Petri

dish containing electrolyte solution. Immediately after the droplet generation, the glass is transferred into the AFM fluidic cell.

The thermal tuning method is used to measure the cantilever properties in air, and in liquid before and after picking a droplet.. Calibration must be performed for each cantilever prior to a series of measurements without disassembling the AFM fluid cell. For measurement in liquid, the previous deflection sensitivity number found in air is used for the spring constant calculation. As an example, thermal spectrum measurement results for cantilever design 2a (Table 7.3) are shown in Table 7.4.

With a droplet attached onto the cantilever, the mass is increased and hence the resonant frequency decreases. The measurement also shows that the cantilever Q is very low in the liquid compared to that in air because of increased viscous damping from the liquid. After a droplet is attached the resonance frequency decreases further due to the additional mass. This drop in frequency can be used to verify that a droplet is successfully attached to the cantilever. Optical verification of attachment can also be used for large droplet, as shown in Figure 7.13.

Table 7.4 Thermal spectrum results of the cantilever design type 2a (Table 7.3) in a fluid

Design 2a	In air	in liquid* (before droplet)	in liquid* (after droplet)
Q	41.0	2.4	2.6
f_0 (kHz)	5.764	2.144	1.445
k_c (N/m)	0.0513	0.0267*	0.0180*

* In liquid, k_c, f_0 values are used for verifying the droplet attachment. They are different from the definition of the spring constant because additional fluid mass changes the inertia.

It proved much easier to use the special cantilevers to pickup an oil droplet compared to standard cantilevers. By using the special cantilevers, a 100% success rate was obtained

in picking up oil droplets. Another observation is that no apparent liquid slip is found using the silicon cantilever and droplets are nicely anchored onto the metal pad area. Previous experiments using Si_3N_4 cantilevers showed the surface roughness of nitride can lead to an apparent slip length because the liquid contact line can still move. Surface roughness can also reduce the adhesion force making it difficult to attach a bubble or droplet at all to the cantilevers.[140]
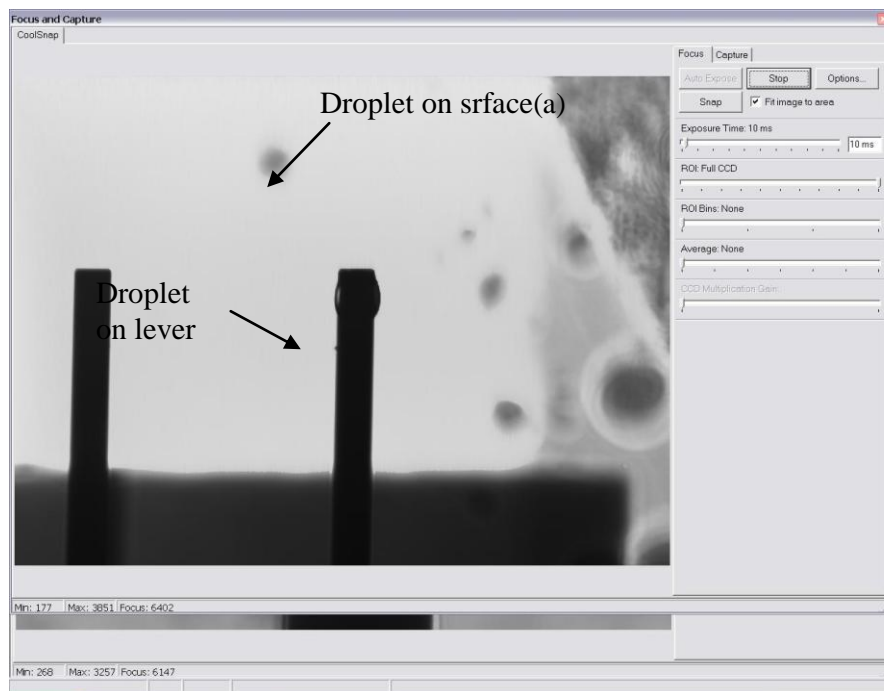
Figure 7.13 An oil droplet attached to a cantilever. This droplet can then be placed over another droplet, some of which can be observed (out of focus) on the underlying glass substrate

7.2.3.3 Results from the Melbourne group

The extensive experiments on bubble–bubble and droplet–droplet interactions undertaken at Melbourne University using the special cantilevers do not form part of this Thesis. For completeness, some major findings are;

In reference 16: Bubbles of air are placed on a cantilever and force curves measured for interactions with a mica surface in either 1mM $NaNO_3$ electrolyte or in a 10mM

sodium dodecylsulfate (SDS) surfactant solution. The boundary condition at the bubble-liquid interface can be determined rigorously by comparing the measured hydrodynamic forces with model Reynolds equations, with verification strengthened by comparisons over a range of approach velocities. In the presence of surfactant SDS, the *no slip* boundary condition holds i.e. the radial component of the fluid velocity is zero at the mica interface and the bubble-liquid interface. This is expected and has been measured for wetting liquids.[141] However, the results using the pure $NaNO_3$ electrolyte fall between *no slip* and *full slip* (fully mobile interface) boundary conditions. Whilst this observation could be fitted within a model incorporating some slip length (~20nm), as in many previous reports,[142] an alternative explanation is proposed that fully fits the AFM data. In the absence of surfactants, bubbles are *very* sensitive to trace amounts of insoluble surface active impurities, which need only slightly lower the surface tension at the air-liquid interface to change the hydrodynamic forces. In the $NaNO_3$ electrolyte experiments, the required change in surface tension to fit the hydrodynamic force data is less than 0.1mN/m, which is smaller than the error in the measured bubble-liquid interfacial tension (72 ±1mN/m).

In reference 15: A~100μm diameter bubble is again placed on specially fabricated cantilevers (Figure 7.14), but here the cantilever bubble is positioned symmetrically above another bubble attached to a surface (mildly hydrophobic glass). This arrangement allowed the forces between two interacting bubbles in liquid to be directly measured. Of particular interest is bubble coalescence. Force curves were undertaken under a variety of different conditions (approach velocity, initial separation, continuous or stop-start approach) and the time-dependent forces measured. Experiments were undertaken in 0.5M $NaNO_3$ so no electrical double

layer repulsion is present between the bubbles, the only forces being van der Waals attraction, hydrodynamic forces from the flow of water, and the surface tension of the bubbles (which influences the deformation of the bubble when external forces are applied). It was found bubbles can coalesce if the force on approach was sufficiently strong to overcome the repulsive hydrodynamic force arising from water trying to drain from the bubble-bubble gap. Surprisingly it was found that coalescence can also occur, and at lower forces, as the bubbles separate or remain stationary after approach. These counterintuitive "coalescence on separation" results arise because it is found the basic requirement for coalescence is that some local region of the intervening water film (around the outer rim of the deformed bubble under the experimental conditions) becomes thinner than ~5nm, in which case the van der Waals attraction to destabilizes the water film, leading to rapid film rupture. This can occur on separation of the bubbles because *attractive* hydrodynamic forces occur as water flows back between the bubbles, deforming the bubbles towards each other. In contrast to previous reports,[143] there appears to be no special role played by thermal fluctuations in triggering coalescence; nor is there support for the use of special ions at high concentration to prevent coalescence[144].
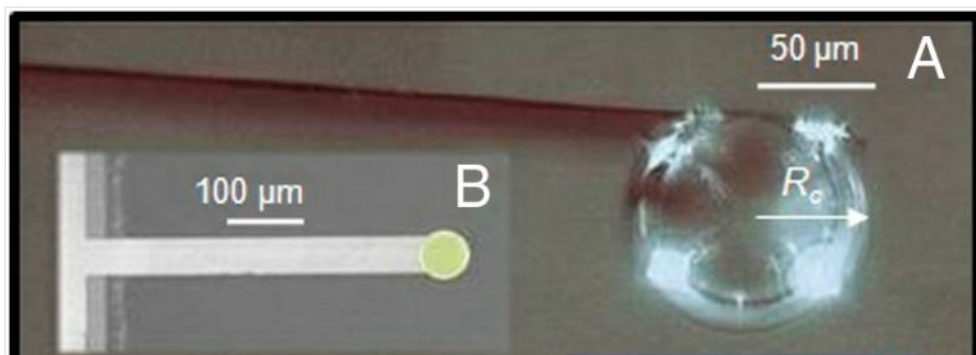
Figure 7.14(a) Side view of a bubble anchored on the tip of a cantilever. (b) Plan view of a cantilever showing the extended gold pad at the end used to anchor the bubble.

7.3 Conclusion

This chapter describe the microfabrication and characterization of special AFM cantilevers for ultra-low friction force measurements. The chapter includes the fabrication of ultrathin cantilevers (~300 nm thick) with a mass loading at the free end. We propose that the use of such ultra-thin cantilevers in a pendulum AFM geometry can be used to measure very low friction forces e.g. on lubricants, with the AFM operating in contact mode. The chapter also describes the fabrication and characterization of special cantilevers so that a droplet or a bubble can be reliably attached to the free end of the lever. These levers were used at the University of Melbourne as a colloid probe type AFM in aqueous solutions, enabling the drainage of water films between two approaching bubbles or droplets to be measured.

\

Chapter 8 Conclusion

8.1 General Conclusion

Very thin sleds were constructed, down to 300nm thick with atomically sharp Si_3N_4 tips. Thicker sleds (~3μm) were also constructed with sharp silicon tips. The vibration modes were measured experimentally using a laser vibrometer and qualitatively match the FEM modelling of section 4.3. The modes measured by the suspended structure approach (section 6.2) can be related to the free structure on a surface (section 6.3), provided the actuation is sufficient.

Tip location is important and can affect the mode shape for sleds on a surface. To induce lateral sled motion, the amplitude of the tips should be large enough to overcome the tip-surface contact, and at least two of the tips should move in-phase.

All thick sleds could be actuated on mica, F-Si, and graphite surfaces. The actuation occurred over a narrow frequency window and was initiated most easily at 300 kHz to 400 kHz, or additionally near 180 kHz on F-Si. In general, actuation of a sled on mica requires a higher actuation voltage than a sled on F-Si, and the actuation is repeatable using the same sled. Actuation of a sled on graphite requires smaller voltage however the actuation cannot be repeated on the same device.

A new AFM based approach for measuring the friction of free standing MEMS structures was demonstrated. The method can measure nano-Newton to micro-Newton forces (both friction and load) and provides a means to measure friction of macroscopic structures at very low load.

Ultra-thin AFM cantilevers were also microfabricated for ultra-low friction force measurements. The use of such cantilevers in a pendulum AFM geometry is proposed to measure very low friction forces with the AFM operating in contact mode. Special cantilevers are also manufactured and characterized so that a droplet or a bubble can be reliably attached to the free ends of the levers. The cantilevers are used as a colloid probe type AFM in aqueous solutions.

8.2 Future work

One outstanding task is to unequivocally relate the sled movement to actuated superlubricity by the simultaneous measurement of the sled friction, actuation, and mode properties. This remains very challenging and several related problems will require investigation. For example, the PZT approach is not ideal unless an accurate analysis of the coupling of substrate motion to the sled can be successfully undertaken. A more straightforward approach for stronger actuation of the sled would be to develop improved magnetic or electrostatic actuation methods. Also, future experiments should preferably be done under vacuum to remove squeeze damping and to minimize surface contamination.

Of the surfaces studied, F-Silicon proved to be the most reliable substrate for actuation studies, but curiously not for vibrometer measurement. The use of other surfaces, such as diamond like carbon (DLC), should be investigated. DLC has excellent tribology properties and satisfies the substrate requirements for actuated superlubricity (Table 1.1).

Finally, some aspects of the sled manufacture could be improved. The tip locations require more careful analysis in future designs for optimum sled movement. For improved optical properties of the sled surfaces, a simpler fabrication flow for making thin sleds is desirable e.g. using RIE to thin down a thicker sled would remove the need

of a metal coating and minimize the stress.

REFERENCES

1. Madou, M. J. Fundamentals of microfabrication; 1st ed, CRC Press: Boca Raton, Fla., 1997.

2. Bhushan, B. J. Vac. Sci. Technol. B 2003, 21, 2262.

3. Bhushan, B. Microelectronic Engineering 2007, 84, 387.

4. Akiyama, T.; Collard, D.; Fujita, H. J. Microelectromech. Syst. 1997, 6, 10.

5. Erdemir, A.; Martin, J. M. Superlubricity; 1st ed.; Elsevier,: Amsterdam, 2007.

6. Socoliuc, A.; Gnecco, E.; Maier, S.; Pfeiffer, O.; Baratoff, A.; Bennewitz, R.; Meyer, E. Science 2006, 313, 207.

7. Kenny, T. W.; Kaiser, W. J.; Rockstad, H. K.; Reynolds, J. K.; Podosek, J. A.; Vote, E. C. J. Microelectromech. Syst. 1994, 3, 97.

8. Biswas, A.; Weller, T.; Katehi, L. P. B. Rev. Sci. Instrum. 1996, 67, 1965.

9. Burdess, J. S.; Harris, A. J.; Wood, D.; Pitcher, R. J.; Glennie, D. J. Microelectromech. Syst. 1997, 6, 322.

10. Eichner, D.; VonMunch, W. Sens. Actuator A-Phys. 1997, 60, 103.

11. Liu, C. H.; Grade, J. D.; Barzilai, A. M.; Reynolds, J. K.; Partridge, A.; Rockstad, H. K.; Kenny, T. W.; ASME Winter Conf.&mdash, Symp. Micro-Electron Mechanical Syst. 1997, p13-20.

12. Cannella, F.; Marchetti, B. In Sixth International Conference on Vibration Measurements by Laser Techniques: Advances and Applications, 22-25 June 2004; 1 ed.; SPIE-Int. Soc. Opt. Eng: USA, 2004; Vol. 5503, p 468.

13. Tang, X. S.; Loke, Y. C.; Lu, P.; Sinha, S.K.; O'Shea, S. J. J. Rev. Sci. Instrum. 2012.84, 13702

14. Rast, S.; Gysin, U.; Ruff, P.; Gerber, C.; Meyer, E.; Lee, D. W. Nanotechnology 2006, 17, S189.

15. Vakarelski, I. U.; Manica, R.; Tang, X. S.; O'Shea, S. J.; Stevens, G. W.; Grieser, F.; Dagastine, R. R.; Chan, D. Y. C. Proc. Natl. Acad. Sci. U. S. A. 2010, 107, 11177.

16. Manor, O.; Vakarelski, I. U.; Tang, X. S.; O'Shea, S. J.; Stevens, G. W.; Grieser, F.; Dagastine, R. R.; Chan, D. Y. C. Phys. Rev. Lett. 2008, 101, 24501.

17. Kovacs, G. T. A. Micromachined transducers sourcebook; WCB: Boston, Ma., 1998.

18. Israelachvili, J. N. Intermolecular and Surface Forces; Academic Press, Oxford, 2011.

19. Mate, C. M. Tribology on the small scale : a bottom up approach to friction, lubrication, and wear; Oxford University Press: Oxford ; New York, 2008.

20. Mehregany, M.; Yu-Chong, T. J. Micromech. Microeng. 1991, 1, 73.

21. Tanner, D. M.; Miller, W. M.; Peterson, K. A.; Dugger, M. T.; Eaton, W. P.; Irwin, L. W.; Senft, D. C.; Smith, N. F.; Tangyunyong, P.; Miller, S. L. Microelectron. Reliab. 1999, 39, 401.

22. Akiyama, T.; Shono, K. J. Microelectromech. Syst. 1993, 2, 106.

23. Koinkar, V. N.; Bhushan, B. J. Vac. Sci. Technol. A 1996, 14, 2378.

24. Williams, J. A.; Le, H. R. J. Phys. D: Appl. Phys. 2006, 39, R201.

25. Frechette, L. G.; Nagle, S. F.; Ghodssi, R.; Umans, S. D.; Schmidt, M. A.; Lang, J. H.; IEEE In 14th IEEE International Conference on Micro Electro Mechanical Systems, Technical Digest 2001, p 290.

26. Kovacs, G.T.A.; Maluf, N.I.; Petersen, K.E. Proceedings of the IEEE 1998, 86, 1536.

27. Trumper, D. L.; Won-Jong, K.; Williams, M. E. IEEE T.Ind.Appl. 1996, 32, 371.

28. Choi, Y. M.; Lee, M. G.; Gweon, D. G.; Jeong, J. Rev. Sci. Instrum. 2009, 80.45106.

29. Wagner, B.; Kreutzer, M.; Benecke, W. J. Microelectromech. Syst. 1993, 2, 23.

30. Wagner, B.; Benecke, W. In Proceedings. IEEE Micro Electro Mechanical Systems. An Investigation of Micro Structures, Sensors, Actuators, Machines and Robots (Cat. No.91CH2957-9), 30 Jan.-2 Feb. 1991; IEEE: New York, NY, USA, 1991, p 27.

31. Asay, D. B.; Dugger, M. T.; Kim, S. H. Tribol. Lett. 2008, 29, 67.

32. Rodgers, M. S.; Sniegowski, J. J. 5-level polysilicon surface micromachine technology: Application to complex mechanical systems, 1998.

33. Yu H. B.; Zhou, G. Y.; Sinha, S. K.; Leong, J. Y.; Chau F. S. J. Microelectromech. Syst. 2011, 20, 991.

34. Hirano, M.; Shinjo, K. Phys. Rev. B. 1990, 41, 11837.

35. Shinjo, K.; Hirano, M. In Third ISSP International Symposium on Dynamical Processes at Solid Surfaces, 20-23 April 1992; 1-3 ed. Netherlands, 1993; Vol. 283, p 473.

36. Hirano, M.; Shinjo, K.; Kaneko, R.; Murata, Y. Phys. Rev. Lett. 1991, 67, 2642.

37. Hirano, M. "Superlubricity of clean surfaces", Superlubricity; 1st ed.; Elsevier,: Amsterdam, 2007, p17.

38. Dienwiebel, M.; Verhoeven, G. S.; Pradeep, N.; Frenken, J. W. M.; Heimberg, J. A.; Zandbergen, H. W. Phys. Rev. Lett. 2004, 92.126101.

39. Gnecco, E.; Maier, S.; Meyer, E. Journal of Physics-Condensed Matter 2008, 20.

40. Carpick, R. W. Science 2006, 313, 184.

41. Kim, S. H.; Strawhecker, K. Abstracts of Papers of the American Chemical Society 2004, 227, U828.

42. Van Spengen, W. M.; Frenken, J. W. M. Tribol. Lett., 2007, 28, 149.

43.   Mate, C. M.; McClelland, G. M.; Erlandsson, R.; Chiang, S. Phys. Rev. Lett. 1987, 59, 1942.

44.   Meyer, G.; Amer, N. M. Appl. Phys. Lett. 1988, 53, 1045.

45.   Stowe, T. D.; Yasumura, K.; Kenny, T. W.; Botkin, D.; Wago, K.; Rugar, D. Appl. Phys. Lett. 1997, 71, 288.

46.   Sidles, J. A.; Garbini, J. L.; Bruland, K. J.; Rugar, D.; Zuger, O.; Hoen, S.; Yannoni, C. S. Reviews of Modern Physics 1995, 67, 249.

47.   Yaqiang, W.; van der Weide, D. W. J. Vac. Sci. Technol., B: Microelectron. Nanometer Struct.--Process., Meas., Phenom. 2005, 23, 1582.

48.   Loke, Y. C.; Hofbauer, W.; Lu, P.; K.Ansari; Xiaosong, T.; O'Shea, S. J. Rev. Sci. Instrum. 2011 82 115002.

49.   Tang, P. T. Electrochim. Acta 2001, 47, 61.

50.   Sharma, J.; DasGupta, A. J. Micro/Nanolith. MEMS MOEMS. 2008, 7, 043007.

51.   Wang, B.; Zhang, W.; Zhang, W.; Mujumdar, A. S.; Huang, L. Drying Technology 2005, 23, 7.

52.   Yan Xin, Z.; Hansen, O.; Knieling, T.; Wang, C.; Rombach, P.; Lang, W.; Benecke, W.; Kehlenbeck, M.; Koblitz, J. J. Microelectromech. Syst. 2007, 16, 1451.

53.   Zhou, J.; Wolden, C. A. J. Electrochem. Soc. 2000, 147, 4142.

54.   Han, WH,; Lindsay, SM; Jing, TW. Appl. Phys. Lett. 1996, 69, 4111.

55.   O'Shea, S. J.; Welland, M. E.; Pethica, J. B. Chem. Phys. Lett. 1994, 223, 336.

56.   Choi, S.-H.; An, K.; Kim, E.-G.; Yu, J. H.; Kim, J. H.; Hyeon, T. Adv. Funct. Mater. 2009, 19, 1645.

57.   Rugar, D.; Hansma, P. Physics Today 1990, 43, 23.

58.   Lantz, M. A.; Oshea, S. J.; Welland, M. E.; Johnson, K. L. Phys. Rev. B 1997, 55, 10776.

59.   O'Shea, S. J.; Welland, M. E.; Rayment, T. Appl. Phys. Lett. 1992, 61, 2240.

60.   Meyer, G.; Amer, N. M. Appl. Phys. Lett. 1990, 57, 2089.

61.   Socoliuc, A.; Bennewitz, R.; Gnecco, E.; Meyer, E. Phys. Rev. Lett. 2004, 92.134301.

62.   Polytec Scanning Vibrometer Hardware manual; Polytec International.

63.   Tas, N.; Sonnenberg, T.; Jansen, H.; Legtenberg, R.; Elwenspoek, M. J. Micromech. Microeng. 1996, 6, 385.

64.   de Boer, M. P.; Knapp, J. A.; Mayer, T. M.; Michalske, T. A. In Microsystems Metrology and Inspection; Gorecki, C., Ed. 1999; Vol. 3825, p 2.

65.   Pamidighantam, S.; Laureyn, W.; Rusu, C.; Baert, K.; Puers, R.; Tilmans, H. A. C. Sens. Actuator A-Phys. 2003, A103, 202.

66.   Easter, C.; O'Neal, C. B. J. Microelectromech. Syst.2009, 18, 1054.

67.   Celler, G. K.; Cristoloveanu, S. J. Appl. Phys. 2003, 93, 4955.

68.   Arana, L. R.; de Mas, N.; Schmidt, R.; Franz, A. J.; Schmidt, M. A.; Jensen, K. F. J. Micromech. Microeng. 2007, 17, 384.

69.   Madou, M. J. Fundamentals of microfabrication and nanotechnology : solid-state physics, fluidics, and analytical techniques in micro-and nanotechnology; 3rd ed.; CRC Press: Boca Raton, Fla, 2012.

70.   Albrecht, T. R.; Akamine, S.; Carver, T. E.; Quate, C. F. In Topical Conference on Nanometer Scale Properties of Surfaces and Interfaces, 23-26 Oct. 1989; 4 ed. USA, 1990; Vol. 8, p 3386.

71.   Brugger, J.; Buser, R. A.; Derooij, N. F. Sens. Actuator A-Phys. 1992, 34, 193.

72.   Zou, H. Microsyst. Technol. 2004, 10, 603.

73.   Leissa, A. Vibration of Plates; Acoustical Scociety of America, Columus, Ohio, USA, 1993.

74.   Hurley, D. C.; Turner, J. A. J. Appl. Phys. 2007, 102.

75.   Lantz, M. A.; Oshea, S. J.; Hoole, A. C. F.; Welland, M. E. Appl. Phys. Lett. 1997, 70, 970.

76.   Holland, R.; Dugdale, T. M.; Wetherbee, R.; Brennan, A. B.; Finlay, J. A.; Callow, J. A.; Callow, M. E. Biofouling 2004, 20, 323.

77.   Itano, M.; Kern, F. W.; Miyashita, M.; Ohmi, T. IEEE T. Semiconduct. M. 1993, 6, 258.

78.   Williams, J. A.; Le, H. R. J. Phys. D-Appl. Phys. 2006, 39, R201.

79.   Tas, N. R.; Gui, C.; Elwenspoek, M. J. Adhes. Sci. Technol. 2003, 17, 547.

80.   Gerde, E.; Marder, M. Nature 2001, 413, 285.

81.   Gao, J. P.; Luedtke, W. D.; Gourdon, D.; Ruths, M.; Israelachvili, J. N.; Landman, U. J. Phys. Chem. B 2004, 108, 3410.

82.   Achanta, S.; Celis, J. P. Wear 2010, 269, 435.

83.   Guo, Z. S.; Feng, Z.; Fan, S. C.; Zheng, D. Z.; Zhuang, H. H. Microsystem Technologies-Micro-and Nanosystems-Information Storage and Processing Systems 2009, 15, 343.

84.   CSM Instruments SA CH-2034 Peseux, Switzerland.

85.   Wang, M.; Xu, D.; Ravi-Chandar, K.; Liechti, K. M. Experimental Mechanics 2007, 47, 123.

86.   Heslot, F.; Baumberger, T.; Perrin, B.; Caroli, B.; Caroli, C. Phys. Rev. E. 1994, 49, 4973.

87.   Achanta, S.; Drees, D.; Celis, J. P. Surf. Coat. Technol. 2008, 202, 6127.

88. Dietzel, D.; Monninghoff, T.; Jansen, L.; Fuchs, H.; Ritter, C.; Schwarz, U. D.; Schirmeisen, A. J. Appl. Phys. 2007, 102.

89. Dietzel, D.; Ritter, C.; Monninghoff, T.; Fuchs, H.; Schirmeisen, A.; Schwarz, U. D. Phys. Rev. Lett. 2008, 101.125505.

90. Houston, M. R.; Howe, R. T.; Maboudian, R. J. Appl. Phys. 1997, 81, 3474.

91. Delrio, F. W.; De Boer, M. P.; Knapp, J. A.; Reedy, E. D.; Clews, P. J.; Dunn, M. L. Nat. Mater. 2005, 4, 629.

92. Prokopovich, P.; Starov, V. Adv. Colloid Interface Sci. 2011, 168, 210.

93. Butt, H. J.; Cappella, B.; Kappl, M. Surf. Sci. Rep. 2005, 59, 1.

94. Berman, A.; Drummond, C.; Israelachvili, J. Tribol. Lett., 1998, 4, 95.

95. Bowder F.P.; Talor, D. The Friction and Lubrication of Solids I; Clarendon Press, Oxford) 1950.

96. Szlufarska, I.; Chandross, M.; Carpick, R. W. J. Phys. D Appl. Phys. 2008, 41, 123001.

97. Carpick, R. W.; Ogletree, D. F.; Salmeron, M. Appl. Phys. Lett. 1997, 70, 1548.

98. Johnson, K. L. Contact Mechanics; Cambridge University Press, Cambridge, 1985.

99. Ducker, W. A.; Senden, T. J.; Pashley, R. M. Nature 1991, 353, 239.

100. Oshea, S. J.; Welland, M. E.; Wong, T. M. H. Ultramicroscopy 1993, 52, 55.

101. Chung, K. H.; Reitsma, M. G. Rev. Sci. Instrum. 2010, 81, 26104.

102. Sader, J. E.; Green, C. P. Rev. Sci. Instrum. 2004, 75, 878.

103. Srinivasan, U.; Houston, M. R.; Howe, R. T.; Maboudian, R. J. Microelectromech. Syst. 1998, 7, 252.

104. Gnecco, E.; Bennewitz, R.; Gyalog, T.; Meyer, E. Journal of Physics-Condensed Matter 2001, 13, R619.

105. Derjaguin, B. V.; Muller, V. M.; Toporov, Y. P. J. Colloid Interface Sci. 1975, 53, 314.

106. Bora, C. K.; Flater, E. E.; Street, M. D.; Redmond, J. M.; Starr, M. J.; Carpick, R. W.; Plesha, M. E. Tribol. Lett., 2005, 19, 37.

107. Lu, P.; O'Shea, S. J. J. Phys. D Appl. Phys. 2012, 45, 475303.

108. Jones, R. E. J. Appl. Mech-T.Asme. 2007, 74, 31.

109. Adams, G. G.; Muftu, S.; Azhar, N. M. J. Tribol-T. Asme 2003, 125, 700.

110. Bhushan, B. Tribol. Lett., 1998, 4, 1.

111. Laboriante, I.; Bush, B.; Lee, D.; Liu, F.; Liu, T. J. K.; Carraro, C.; Maboudian, R. J. Adhes. Sci. Technol. 2010, 24, 2545.

112. Whitby, J. A.; Ostlund, F.; Horvath, P.; Gabureac, M.; Riesterer, J. L.; Utke, I.; Hohl, M.; Sedlacek, L.; Jiruse, J.; Friedli, V.; Bechelany, M.; Michler, J. Advances in Materials Science and Engineering 2012.

113. Gutowski, P.; Leus, M. Tribol. Int. 2012, 55, 108.

114. Hesjedal, T.; Behme, G. IEEE T. Ultrason. Ferr 2002, 49, 356.

115. Storck, H.; Littmann, W.; Wallaschek, J.; Mracek, M. Ultrasonics 2002, 40, 379.

116. Kumar, V. C.; Hutchings, I. M. Tribol. Int. 2004, 37, 833.

117. Capozza, R.; Vanossi, A.; Vezzani, A.; Zapperi, S. Phys. Rev. Lett. 2009, 103, 85502.

118. Teidelt, E.; Starcevic, J.; Popov, V. L. Tribol. Lett., 2012, 48, 51.

119. Erlandsson, R.; Hadziioannou, G.; Mate, C. M.; McClelland, G. M.; Chiang, S. J. Chem. Phys. 1988, 89, 5190.

120.   Gee, M. L.; McGuiggan, P. M.; Israelachvili, J. N.; Homola, A. M. J. Chem. Phys. 1990, 93, 1895.

121.   Mamin, H. J.; Poggio, M.; Degen, C. L.; Rugar, D. Nat. Nanotechnol. 2007, 2, 301.

122.   Rugar, D.; Budakian, R.; Mamin, H. J.; Chui, B. W. Nature 2004, 430, 329.

123.   Rast, S.; Wattinger, C.; Gysin, U.; Meyer, E. Nanotechnology 2000, 11, 169.

124.   Yang, J.; Neudeck, G. W.; Denton, J. P. Appl. Phys. Lett. 2000, 77, 4034.

125.   Strus, M. C.; Raman, A. Phys. Rev. B 2009, 80, 224105.

126.   Dietzel, D.; Marsaudon, S.; Aime, J. P.; Nguyen, C. V.; Couturier, G. Phys. Rev. B 2005, 72, 35445.

127.   Snow, E. S.; Campbell, P. M.; Novak, J. P. Appl. Phys. Lett. 2002, 80, 2002.

128.   Roters, A.; Johannsmann, D. Journal of Physics-Condensed Matter 1996, 8, 7561.

129.   Carpick, R. W.; Salmeron, M. Chem. Rev. 1997, 97, 1163.

130.   Lewin, A. C.; Kersey, A. D.; Jackson, D. A. J.Phys. E. Sci. Instrum. 1985, 18, 604.

131.   Albrecht, T. R.; Grutter, P.; Horne, D.; Rugar, D. J. Appl. Phys. 1991, 69, 668.

132.   Yasumura, K. Y.; Stowe, T. D.; Chow, E. M.; Pfafman, T.; Kenny, T. W.; Stipe, B. C.; Rugar, D. J. Microelectromech. Syst. 2000, 9, 117.

133.   Gurtin, M. E.; Markenscoff, X.; Thurston, R. N. Appl. Phys. Lett. 1976, 29, 529.

134.   Lu, P.; Lee, H. P.; Lu, C.; O'Shea, S. J. Phys. Rev. B 2005, 72, 085405.

135.   Butt, H.-J.; Cappella, B.; Kappl, M. Surf. Sci. Rep. 2005, 59, 1.

136.   Lockie, H. J.; Manica, R.; Stevens, G. W.; Grieser, F.; Chan, D. Y. C.; Dagastine, R. R. Langmuir 2011, 27, 2676.

137.   Dagastine, R. R.; Manica, R.; Carnie, S. L.; Chan, D. Y. C.; Stevens, G. W.; Grieser, F. Science 2006, 313, 210.

138.   Cleveland, J. P.; Manne, S.; Bocek, D.; Hansma, P. K. Rev. Sci. Instrum. 1993, 64, 403.

139.   Hutter, J. L.; Bechhoefer, J. Rev. Sci. Instrum. 1993, 64, 1868.

140.   Schaeffer D.M.; Carpenter, M.; Gady, B., Reifenberger, R.; Demejo, L.P.; Rimai, D.S. J. Adhes. Sci. Technol. 1995, 1049.

141.   Chan, D. Y. C.; Horn, R. G. J. Chem. Phys. 1985, 83, 5311.

142.   Neto, C.; Evans, D. R.; Bonaccurso, E.; Butt, H. J.; Craig, V. S. J. Reports on Progress in Physics 2005, 68, 2859.

143.   Ivanov, I. B.; Kralchevsky, P. A. Colloid. Surface. A. 1997, 128, 155.

144.   Craig, V. S. J.; Ninham, B. W.; Pashley, R. M. Nature 1993, 364, 317.